Boosted $b\bar{b}$ decays with the ATLAS experiment at the LHC

Luke Lambourne
University College London

Submitted to University College London in fulfilment
of the requirements for the award of the
degree of **Doctor of Philosophy**

May 28, 2014

Declaration

I, Luke Lambourne confirm that the work presented in this thesis is my own. Where information has been derived from other sources, I confirm that this has been indicated in the thesis.

Luke Lambourne

Abstract

A measurement and a search, both involving high transverse momentum bosons decaying to b-quarks, are performed using a dataset of proton-proton collisions at $\sqrt{s} = 8$ TeV, collected in 2012 with the ATLAS detector at the LHC, corresponding to an integrated luminosity of 19.5 fb^{-1}.

The production cross section of $Z \to b\bar{b}$ is measured, where the Z boson has high transverse momentum. The measured value of the fiducial cross section is found to be in good agreement with next-to-leading-order Standard Model predictions.

A search is made for TeV-scale resonances decaying via a pair of Higgs bosons to the $b\bar{b}b\bar{b}$ final state. The graviton excitation, G^*, in the bulk Randall-Sundrum model is used as a baseline signal model. No evidence of a resonance is found. Upper limits are set on $\sigma(pp\to G^*) \times \mathrm{BR}(G^*\to HH\to b\bar{b}b\bar{b})$.

Acknowledgements

I would like to thank my supervisor Nikos Konstantinidis for giving me direction throughout my PhD and for his contagious enthusiasm for working on the LHC. Ben Cooper and David Wardrope have been a pleasure to work with, always intelligent, insightful and helpful to me. The University College London High Energy Physics group has been a fantastic collection of people to work within, in particular I'm grateful to Stephen Bieniek and Adam Davison for their helpful responses to my frequent questions. I would like to thank my examiners, Jonathan Hays and David Waters for their corrections to this thesis, which substantially improved it. Clare Bernard for her support and useful comments on this thesis. Finally I would like to thank my parents for their love and support.

Preface

Modern experimental particle physics is a highly collaborative endeavour. The research carried out at the ATLAS experiment depends critically on previous measurements at past experiments as well as on theoretical calculations and many specialised software packages.

The ATLAS collaboration has approximately 3000 members who have all done work on which the experiment as a whole depends. Here I will try to clarify which work presented here is my own. This thesis covers two analyses of the data collected in 2012 by the ATLAS detector. A measurement of the Standard Model process $Z \rightarrow b\bar{b}$ [1] and a search for a heavy particle decaying via $X \rightarrow HH \rightarrow b\bar{b}b\bar{b}$ [2,3]. Both analyses were worked on directly by several people other than myself, and indirectly by many more.

The team working directly on the $Z \rightarrow b\bar{b}$ measurement was Ben Cooper, Nikos Konstantinidis, David Wardrope and myself. For the search it was Ben Cooper, Nikos Konstantinidis, David Wardrope, John Allison, Rebecca Falla, Nurfikri Norjoharuddeen and myself. Both analyses benefited from the scrutiny and suggestions of the collaboration through the internal review process, in particular that of the members assigned to the editorial boards and the convenors of the relevant groups and sub-groups.

In the $Z \rightarrow b\bar{b}$ measurement my work focussed on: the triggering strategy and its associated systematic uncertainty; investigating the variables used to separate the signal from background; investigating and implementing multivariate methods used to combine those variables; the Monte Carlo modelling of the signal, backgrounds and the theoretical predictions. In the $X \rightarrow HH \rightarrow b\bar{b}b\bar{b}$ search, my work focussed on: Monte Carlo production of the backgrounds; optimising the event selection; the statistical treatment of the search and limit setting.

Contents

List of Figures

List of Tables

Chapter 1.

The Standard Model of Particle Physics and Beyond

1.1. The Standard Model of Particle Physics

The Standard Model (SM) of particle physics [4] is a theoretical framework of the interactions of the known fundamental particles and forces with the notable exception of the gravitational force. It is a quantum field theory which describes the interactions of the twelve known fermions, with the force-carrying gauge bosons. It incorporates the Brout-Englert-Higgs mechanism [5, 6], which gives mass to the fundamental particles and has an associated scalar boson. The Standard Model is built on the principle of gauge invariance. The symmetries of the theory predict conserved quantities according to Noether's theorem [7]. Table 1.1 lists the fundamental particles of the SM and their properties.

The Standard Model is an extremely successful theory whose predictions have been tested at various experiments over the course of more than forty years. Relatively recent examples include the discovery of the top quark at the Tevatron [8, 9] and the Higgs Boson at the LHC [10, 11]. The SM also predicts the values of many other measurable quantities such as the ratio of the W and Z masses, the cross sections of interactions in collisions, the probabilities of the different decay modes of unstable particles and much more. So far no measurement has found a significant deviation from the SM prediction.

		Particle	Spin [$\hbar$]	EM Charge [e]	Mass [GeV]
Fermions	Quarks	u	$\frac{1}{2}$	$+\frac{2}{3}$	$\sim 2 \times 10^{-3}$
		c			~ 1.3
		t			~ 173
		d		$-\frac{1}{3}$	$\sim 5 \times 10^{-3}$
		s			~ 0.1
		b			~ 4
	Leptons	e		$+1$	5.11×10^{-4}
		μ			0.106
		τ			1.78
		ν_e		0	$< 2 \times 10^{-9}$
		ν_μ			$< 2 \times 10^{-4}$
		ν_τ			$< 2 \times 10^{-2}$
Bosons		γ	1	0	0
		W		$+1$	80.4
		Z		0	91.2
		g		0	0
		H	0	0	125.

Table 1.1.: The fundamental particles of the Standard Model and their properties.

The Strong Interaction

The strong force is described by an SU(3) quantum field theory called Quantum Chromodynamics (QCD), which is one of the constituent theories that make up the Standard Model. It describes the interaction of colour-charged quarks via the gluon. The gluon itself is colour charged and so self-interacts. A key point about the strong force is that its strength decreases with energy and equivalently increases with distance. One important result of this behaviour is that calculating the first terms of the perturbative expansion of a strong interaction, only gives reasonable predictions above an energy scale of ~1 GeV. Another is that quarks are confined into colourless hadrons. A third is that quarks and gluons produced in experimental collisions result in large numbers of additional strongly produced particles and so are observed as a spray of hadrons. Together these phenomenological issues make accurate calculations of QCD interactions extremely challenging.

1.1.1. Problems with the Standard Model

The most obvious issue with the Standard Model is its failure to account for the gravitational interaction. There is also a lack of an explanation as to why gravity is so much weaker than the other fundamental forces. This difference between the electroweak scale and the gravitational scale manifests itself when considering the mass of the Higgs Boson. When calculating that mass, there are quadratic contributions from the other SM particles, dominated by the top quark, which are divergent up to the Planck scale. This means that there must be a huge amount of fine-tuning of the bare mass of the Higgs, in order to cancel out these quadratic divergences resulting in a 125 GeV mass. This issue is known as the 'hierarchy problem'.

Another problem with the Standard Model is the lack of a particle that could possibly make up the large amounts of 'dark matter' observed in astrophysical experiments. Dark matter is estimated to contribute to $\sim$85% of the matter in the observable universe [12]. The neutrinos are the only SM particles to fulfil the requirements of being stable and only weakly interacting, but their masses are too low to be consistent with the observed distribution of dark matter in the universe.

Other outstanding issues with the Standard Model include the failure to account for the matter-antimatter asymmetry observed in the universe. The SM also contains a very large number of free parameters, such as the masses of the particles and the coupling constants, whose values are not predicted but set through experimental observations.

1.1.2. Beyond the Standard Model Theories

There are a number of theories that solve some of the issues with the SM. These theories are referred to as 'beyond the Standard Model' (BSM) theories. The most famous of these is supersymmetry [13], which, by introducing a new symmetry, predicts a supersymmetric partner particle for each SM particle. This solves the problem of the fine-tuning of the Higgs mass, since the divergent contributions from the top quark are canceled out by its superpartner, the stop squark. It also provides a dark matter candidate in the lightest supersymmetric particle, the neutralino.

The search in this thesis uses a BSM theory known as the Randall-Sundrum model [14] as a benchmark to search for an HH resonance.

Randall-Sundrum Model

An alternative solution for the hierarchy problem is to postulate an extra spatial dimension, in which only the graviton can propagate, with the Higgs boson being fixed at a point, on a 'brane' in that dimension. In the Randall-Sundrum (RS) model [14], known as RS1, there is an extra spatial dimension bounded by two branes, referred to as the TeV brane, where the Higgs boson is fixed, and the Planck brane. The extra dimension is warped, such that gravity becomes exponentially weaker when traveling from the Planck brane to the TeV brane. The rate of that exponential change is parameterised by k, known as the curvature scale and usually expressed as a fraction of the reduced Planck mass: $k/\bar{M}_{\mathrm{Pl}}$. An important prediction of the RS model is a set of massive Kaluza-Klein (KK) excitations of the spin-2 graviton, where the mass of the first excitation, $\mathrm{m}_{\mathrm{G}^*}$, is predicted to be at the TeV scale [15]. Chapter 4 describes a search which uses that first excitation of the graviton as a benchmark signal model. For the model used, the production of the graviton excitation is dominated by gluon-gluon fusion. The decays are dominated by $t\bar{t}$, WW, ZZ and HH.

1.2. Monte Carlo Generators

In order to use the Standard Model and BSM theories to model signal and background processes and to make predictions to be tested with the data collected at the LHC, software packages called 'Monte Carlo event generators' (MC) are used. These tools simulate particle interactions, such as proton-proton collisions, for a specified physical process, e.g. $pp \to Z \to b\bar{b}$. The MC generator produces a sample of these events, with kinematics distributed according to its calculations together with an estimate of the probability of the specified process occurring, in the form of an overall cross section for that process.

1.2.1. Parton Distribution Functions

Protons are made up of three valance quarks but also contain ‘sea quarks’ and gluons produced by the strong force. The term parton refers to either a quark or a gluon. The particle content of the proton is parameterised as probability density functions for each particle type, as a function of the momentum fraction of the parton, x, and the energy scale of the hard interaction, Q. These are called the ‘parton distribution functions’ (PDFs) of the proton. Due to inherent difficulties with QCD calculations, these parameterisations need to be constrained by experimental measurements. The key measurements in modern PDFs are those from the ‘deep inelastic scattering’ (DIS) proton-electron collisions at HERA [16] and the inclusive jet measurements at the Tevatron [17, 18]. The uncertainty on a particular theoretical prediction coming from the accuracy of PDFs is very dependant on what part of the phase-space of the proton structure the prediction is dependant on.

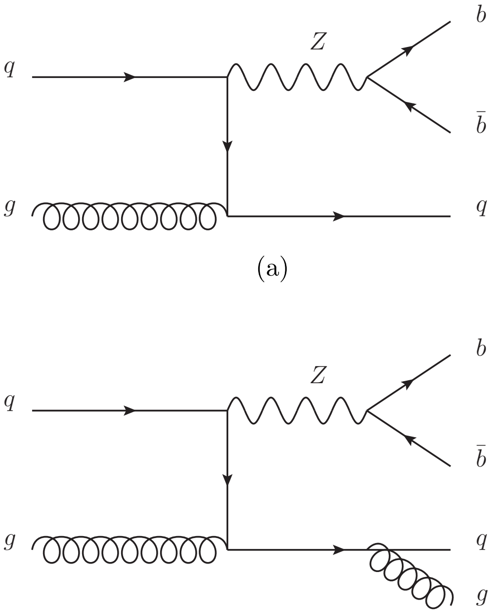

(a)

(b)

Figure 1.1.: Example Feynman diagrams: (a) A leading-order diagram of the $Z + 1\,\text{jet}$ process; (b) the same diagram with an extra gluon radiated.

1.2.2. Event Generation

Production of simulated events is broken down into several different processes.

The first is a perturbative calculation of the matrix element (ME) at a fixed order, using all the subprocess Feynman diagrams for the specified process. This is the so-called ‘hard process’. The phase space integral is then calculated using numerical integration. The selected PDF set is used to obtain the probability densities for the incoming partons of the different types as a function of the parton momentum. This is put together to produce unweighted events.

Next, QCD radiation at lower energies than the hard process is simulated using an approximate technique called a ‘parton shower’ (PS). The parton shower makes use of the fact that in the limit of radiation at small angles from the radiating object, the probabilities for emission can be factorised out and interference can be neglected. The parton shower simulates emission from the energy scale of the hard process until the non-perturbative scale of $\sim$1 GeV.

After obtaining the event including the extra QCD radiation from the parton shower, the process of hadronisation, whereby coloured partons are confined into colourless hadrons, is simulated. This is simulated using phenomenological models, such as the string [19] and cluster [20] models.

The final part of the MC generation is to take into account interactions of the remaining constituents of the proton. This is referred to as the ‘underlying event’ and has the effect of producing extra soft QCD radiation in the event.

1.2.3. Examples of Monte Carlo Event Generators

Currently there are several different MC generators used to model collisions at the LHC [21]. Two of the most widely used are the leading order generators HERWIG++ [22] and PYTHIA 8 [23]. These have different approaches to the parton shower, with HERWIG++ using angular ordering and PYTHIA 8 using transverse momentum (p_{T}) ordering. Other differences include the choice of hadronisation model, with HERWIG++ using a cluster model and PYTHIA 8 using a string model. The leading-order approximation tends to not give an accurate value for the overall cross section of a process and so typically the overall cross sections of samples produced by these generators are normalised to an NLO prediction or a measured cross section. An example leading-order Feynman diagram for the $Z + 1$ jet process is shown in Figure 1.1(a). The parameters of the parton shower, hadronisation and underlying event, are tuned in order to maximise the quality of the modelling of data measurements.

Another type of generator tries to improve on the predictive power of the leading-order + parton shower approach by taking into account Feynman diagrams with extra hard partons when calculating the matrix element and merging those calculations with the predictions of the parton shower. These are known as either ME+PS or 'multi-leg' generators and an example of one used in this thesis is SHERPA [24]. Figure 1.1(b) shows an example of one of the Feynman diagrams containing extra parton radiation that would be used to calculate the matrix element of the Z+jets process with this class of generators. These generators are found, in particular, to produce more accurate predictions than standard LO generators in distributions that depend on extra hard radiation in the event, like for example, the number of jets in the event, above a given jet p_{T} threshold.

The current state-of-the-art generators are those that interface an NLO matrix element calculation with a parton shower MC. Examples of these are POWHEG [25] and aMC@NLO [26]. POWHEG and aMC@NLO differ in how they account for possible double counting between the matrix element and the parton shower. aMC@NLO produces negative weight events, to cancel out this overlap. POWHEG achieves this without producing negative weight events.

Chapter 2.

The ATLAS Detector

2.1. Introduction

The Large Hadron Collider (LHC) is a 27 km circumference synchrotron designed to accelerate two beams of protons up to an energy of 7 TeV each [27]. The beams are crossed at specific points along the ring and the products of the resulting collisions are recorded by four detectors, which are located at those crossing points. ATLAS is one of these detectors.

ATLAS [29] is a general purpose detector, designed to explore the high energy frontier at the LHC. A diagram of the detector is shown in Figure 2.1. It is cylindrical in shape, 44 m long and 25 m in diameter. It is composed of layers of subdetectors, each designed to measure different information about the particles resulting from the collisions. It is designed to cope with the extreme radiation environment of the LHC. As a consequence of the desired high luminosity, there are multiple collisions in each crossing of proton bunches at the LHC. These multiple collisions are referred to as 'pile-up' and ATLAS has to be able to accurately reconstruct and measure particles in the presence of large numbers of pile-up collisions. In 2012, the average number of collisions per bunch crossing reached 37.

The coordinates system in ATLAS is defined as follows: the z direction points along the beamline, ϕ is the azimuthal angle of spherical coordinates, which is around the beamline and θ is the polar angle of spherical coordinates, which is in the plane of the beamline. Typically in hadron colliders, a transformation of θ is used called

Figure 2.1.: A diagram of the ATLAS detector [28].

'pseudorapidity', which is defined as:

$$\eta = -\ln\left[\tan\left(\frac{\theta}{2}\right)\right], \tag{2.1}$$

which approaches the kinematic variable rapidity in the massless limit. Objects at low values of $|\eta|$ are referred to as 'central' and objects at higher values of $|\eta|$ are referred to as 'forward'. The 'transverse' direction is perpendicular to the beam and the 'longitudinal' direction is along the beam.

ATLAS has been collecting data since 2009 and in 2012 collected a dataset of *p*-*p* collisions, at a centre of mass energy of 8 TeV, corresponding to an integrated luminosity of $\sim$20 fb^{-1}.

2.2. The Sub-Detectors

2.2.1. Inner Detector

The innermost sub-detector system is called the Inner Detector (ID). It is designed to measure the tracks of charged particles which pass through it. The region $|\eta| < 2.5$ is fully covered by the inner detector. It is made up of three components, which, going outwards from the beamline are: the pixel detector, the semiconductor tracker (SCT) and the transition radiation tracker (TRT). The Inner Detector is encased in a solenoid magnet, providing a magnetic field of 2 T, which allows the momentum of a charged particle to be inferred from the curvature of its track.

The pixel detector is made up of three cylindrical layers and two sets of five disks, positioned at either end of the cylinders. The silicon pixel sensors measure $50\,\mu\text{m} \times 400\,\mu\text{m}$. The SCT is a silicon microstrip detector and is comprised of 4 cylindrical layers and 9 disks at both ends. Each layer has two sets of strips back-to-back at a small angle to each other. The strips have a width of $80\,\mu$m. The TRT is made up of straw detectors, each 4 mm in diameter and filled with a mixture of gasses, including xenon. Straws are oriented both along the beam axis and in disks perpendicular to the beam axis at both ends. The distance of closest approach of a track to the primary collision vertex is known as the 'impact parameter' and is used for identifying tracks from the decay of B-hadrons. The ID achieves impact parameter resolutions down to $\sim 10\,\mu$m in the transverse direction and $\sim 80\,\mu$m in the longitudinal direction.

2.2.2. Calorimeters

The calorimeter is split into two parts; the electromagnetic (EM) calorimeter, surrounded by the hadronic calorimeter. Both are made out of several sampling calorimeters, meaning that they have alternating layers of dense 'absorber' to initiate a shower and instrumented 'active material' to measure the energy.

The EM calorimeter uses lead absorber and liquid argon (LAr), where the ionisation caused by the incident particles is measured. It has a central, cylindrical part referred to as the barrel, and two forward parts, referred to as the end-caps. Its granularity varies over η and between the layers. The first two samplings have the finest granularities of 0.0031 × 0.1 and 0.025 × 0.025 in $\Delta\eta \times \Delta\phi$.

The hadronic calorimeter is made up of barrel, end-cap and forward calorimeter parts. The hadronic barrel consists of iron absorber and plastic scintillator tiles and is instrumented in three sampling layers. At higher pseudo-rapidities the hadronic end-cap ($1.5 < |\eta| < 3.2$) uses copper and LAr and the forward calorimeter ($3.1 < |\eta| < 4.9$) uses copper/tungsten and LAr.

2.2.3. Muon System

The outermost part of the ATLAS detector is designed to measure the tracks of muons. It is composed of triggering and tracking chambers which lie in a strong magnetic field produced by superconducting air-core toroid magnets. It covers $|\eta| < 2.7$. Drift tube detectors measure central tracks and forward tracks are measured with segmented multiwire proportional chambers. The triggering detectors are resistive plate chambers, where plates are separated with a high voltage between them, and multiwire proportional chambers.

2.3. Trigger

The LHC has, so far, collided protons with a bunch spacing of 50 ns, corresponding to an event rate of 20 MHz. An event rate this high is impossible to record and also the majority of collisions that occur at the LHC are physically uninteresting. The solution is to use information from the detector to quickly decide whether to record an event. The system that does this is called the trigger. The ATLAS trigger is made up of three successive levels; ‘level 1’, ‘level 2’ and ‘event filter’. Level 1 is a hardware-based trigger, which uses information from the calorimeter and muon system. Level 2 and the event filter are run on a dedicated CPU farm, using the detector data passed to readout buffers for events selected by Level 1. Level 2 looks at the portion of the detector containing the calorimeter or muon system deposits selected by level 1 and can combine the inner detector information with that from the calorimeter and muon systems, using fast reconstruction and decision algorithms. The event filter then has time to run a more sophisticated reconstruction. Level 1 reduces the event rate to ∼75 kHz and level 2 and the event filter reduced the rate to ∼400 Hz in 2012.

A trigger chain is a sequence of trigger algorithms going through level 1 to level 2 to event filter. A selection of different trigger chains are chosen for a particular period of running, depending on the instantaneous luminosity, which is intended to maximise the physics potential of the collected data by covering a broad range of final states. If the rate of a particular trigger chain is too high, it can be 'prescaled' meaning that only a small fraction of events passing that trigger chain are recorded. For an event selection, requirements made by the trigger are referred to as 'online' and requirements made on the fully reconstructed objects in the recorded data are referred to as 'offline'.

There are 6 trigger chains used in the analyses in this thesis. All 6 are used in the $Z \to b\bar{b}$ measurement and 5 of the 6 are used in the $X \to HH \to b\bar{b}b\bar{b}$ search. These triggers are:

- **EF_2b35_loose_j145_j35_a4tchad**: requires a jet with transverse energy (E_T) above 145 GeV and two jets which are b-tagged, that have E_T above 35 GeV. One of the two b-tagged jets may or may not be the jet with E_T above 145 GeV.
- **EF_b45_medium_j145_j45_a4tchad_ht500**: requires a jet with E_T above 145 GeV and a jet which is b-tagged, that has E_T above 45 GeV. The b-tagged jet may or may not be the jet with E_T above 145 GeV. The scalar sum of the transverse energy of all the jets in the event must be above 500 GeV.
- **EF_b45_medium_4j45_a4tchad_L2FS**: requires at least 4 jets with E_T above 45 GeV including a jet which is b-tagged.
- **EF_b145_medium_j145_a4tchad_ht400**: requires a b-tagged jet that has E_T above 145 GeV. The scalar sum of the transverse energy of all the jets in the event must be above 400 GeV. This trigger chain is used in the $Z \to b\bar{b}$ measurement but not in the $X \to HH \to b\bar{b}b\bar{b}$ search.
- **EF_j360_a4tchad**: requires a jet with E_T above 360 GeV.
- **EF_4j80_a4tchad_L2FS**: requires four jets with E_T above 80 GeV.

2.4. Detector Simulation

Simulating collisions is an important tool for analysing the data collected with ATLAS. The physical process of the proton-proton collision is simulated using the MC generators described in Section 1.2. A simulation of the ATLAS detector [30] is used to model the collision products passing through the detector and the response of the detector. There are two main types of simulation; the full simulation which uses GEANT4 [31] and fast simulations. The full ATLAS detector simulation takes a significant amount of computing time to run each event. One of the fast simulations, used in this thesis, is called AtlFast-II [32]. AtlFast-II uses the full simulation of the inner detector and the muon system but uses a parameterisation of the calorimeter response and the particle showers [33] which results in it being an order of magnitude faster than the full simulation.

The accuracy of the modelling of simulated events is an important source of uncertainty for the vast majority of analyses of ATLAS data. Some of the techniques used to assess the accuracy of the simulation of certain properties of reconstructed objects are discussed in sections 2.6.2, 2.6.2, and 2.7.1.

2.5. Particle Identification and Reconstruction

Different types of stable particles can be identified and their momenta reconstructed using the information from the detector. Muons are identified from tracks in the muon system, which are then matched and combined with corresponding tracks in the Inner Detector. Electrons are identified from isolated tracks in the Inner Detector, matched with an energy deposit in the EM calorimeter. Photons are identified from energy deposits in the EM calorimeter without an associated track. Neutrinos are not directly detected but their presence can be inferred using energy/momentum conservation in the plane transverse to the beam. The momentum in that plane is reconstructed to obtain the missing transverse energy, 'E_T^{miss}'. Hadrons are reconstructed by clustering energy deposits in the calorimeter into objects called 'jets'. Jets containing B-hadrons can be identified using the fact that, at energies above $\sim$20 GeV, B-hadrons typically travel a few mm inside the detector before decaying. This thesis is concerned mainly with measurements involving these 'b-jets' and so they are discussed in more detail in the following sections.

2.6. Jets

The production of quarks and gluons at a high energy collider is seen as a spray of multiple hadrons. These will typically be close together as they pass through the detector and so, in order to attempt to reconstruct the hard process, constituents are clustered together into jets. For theoretical calculations, the constituents are stable particles in a MC generated event. For reconstructed jets in ATLAS, the constituents are clustered neighbouring calorimeter cells [34] which are treated as having 0 mass. There are several different algorithms available to do this clustering. The jets used in this thesis have all been clustered with the anti-k_t algorithm [35]. This algorithm clusters constituents based on their transverse momentum and angular separation, using the two variables:

$$d_{ij} = min\left(\frac{1}{p_{T,i}^2}, \frac{1}{p_{T,j}^2}\right)\left(\frac{\Delta R_{ij}}{R}\right)^2, \tag{2.2}$$

$$d_{i,max} = \frac{1}{p_{T,i}^2}, \tag{2.3}$$

where $\Delta R_{ij} = \sqrt{(\Delta\eta_{ij})^2 + (\Delta\phi_{ij})^2}$ and R is known as the radius parameter of the jet. In each step of the algorithm, $d_{i,max}$ is calculated for each constituent, i, and d_{ij} is calculated, for each unique pair of constituents, ij. The smallest of these two sets of numbers defines what happens in this step: if it is one of the d_{ij} then the corresponding constituents are clustered together into a single constituent by adding their four-momenta, if instead, it is one of the $d_{i,max}$, then i is defined as a jet and removed from the clustering procedure. This process is repeated until every constituent has been associated to a jet. The value of R chosen for the jets used in this thesis is 0.4. This is chosen as a compromise between a radius small enough to be able to resolve two individual b-quarks from the decay of a high-p_{T} boson and a radius large enough to capture most of the radiation from a parton.

2.6.1. Jet Vertex Fraction

Jets from pile-up are a significant background to many physics analyses. In order to reject jets from pile-up, a variable called the jet-vertex-fraction (JVF) is used [36]. JVF is defined as the fraction of the scalar sum of the transverse momentum of tracks, associated to the jet, where the tracks are associated to the hard-scatter vertex, divided by the scalar sum of the transverse momentum of all tracks associated to that jet, where the hard-scatter vertex is defined as the vertex with the highest scalar sum of the p_{T} of associated tracks. A cut on this variable is applied to jets inside the inner detector acceptance, and with a jet $p_{\mathrm{T}} < 50\,\mathrm{GeV}$, since it is very rare for jets from pile-up to reach p_{T} values greater than that. Jets in this thesis are required to have JVF > 0.5. The efficiency of this requirement is dependent on jet p_{T} and the number of pile-up collisions in the event and is typically significantly above 90% for jets with $p_{\mathrm{T}} > 30$ GeV. The rejection of jets from pile-up is close to 100% [37].

2.6.2. Calibration and Uncertainties of Jets

Jet Energy Scale

There is an uncertainty arising from the modeling of the measured energy of jets, known as the jet energy scale (JES) uncertainty. The JES is derived by exploiting momentum conservation between a well-calibrated object or group of objects and a jet, in a variety of different types of events [38]. First, events containing 2 jets, where one of the jets falls inside the most central part of the calorimeter, $|\eta| < 0.8$, and the other is in a more forward region, are used to correct for the η dependence of the calorimeter response. Next, $Z(\rightarrow e^+e^-)$+jet [39] and γ+jet [40] events are used to calibrate the jets up to a point in jet p_{T} where there are no longer enough of these type of events. Lastly, multi-jet events, where a single high p_{T} jet above the Z/γ+jet calibration threshold is balanced against a group of lower p_{T} jets, which have been calibrated with the Z/γ+jet balance, are used to calibrate the higher p_{T} jets. This method is iterated to calibrate up to the highest p_{T} jets.

In order to use the Z/γ+jet balance technique, the energy scale of electrons and photons must be calibrated first. This calibrated scale is known as the electromagnetic

(EM) energy scale. The EM energy scale is calibrated using $Z \to e^+e^-$ events, since the Z mass has been very accurately measured.

There are a large number of sources of uncertainty on the JES, mainly coming from the MC modelling of the events and also from the statistical uncertainty in the various calibration methods. The jets are corrected for the effect of clustering additional energy from pile-up collisions in the event. This correction also has an associated uncertainty, which is part of the total uncertainty on the JES.

The JES uncertainty is implemented as a set of variations of the simulated energy of jets. Each variation is the $\pm 1\sigma$ uncertainty from a particular source of uncertainty in the calibration process. There are 14 of these components and an extra one for b-jets to account for the different properties of these jets, such as an increased number containing electrons. The component uncertainties are dependant on the jet p_{T} and η and 3 of those that relate to the pile-up correction are dependant on the number of reconstructed primary vertices and the average number of collisions per event.

Jet Energy Resolution

The resolution of the measured transverse momentum of a jet can be parameterised as:

$$\frac{\sigma_{p_{\mathrm{T}}}}{p_{\mathrm{T}}} = \frac{A}{p_{\mathrm{T}}} \oplus \frac{B}{\sqrt{p_{\mathrm{T}}}} \oplus C, \tag{2.4}$$

where the first term is due to calorimeter noise, the second is due to stochastic processes such as the amount of energy deposited in the calorimeter and the particle composition of the jet, and the third is a constant term from effects such as dead material.

In order to assess the modelling of the simulated jet energy resolution (JER), momentum conservation in the plane transverse to the beamline is used in events containing two jets [41]. For a jet with p_{T} of 50 GeV the resolution is $\sim$17% with an absolute uncertainty of $\sim$1%.

2.7. B-Tagging

B-hadrons, meaning a hadron containing a b-quark, typically have lifetimes of $\sim$1.5 ps and so, at energies above $\sim$20 GeV, will generally travel a few mm in the detector before decaying. Accurate reconstruction of the decay products of the B-hadron can therefore be used to infer this displacement from the primary collision point. This can then be used in order to assess the likelihood of a jet to contain a B-hadron and so obtain a sample enriched in jets containing B-hadrons.

Primary vertices are reconstructed from the Inner Detector tracks using an adaptive vertex fitting algorithm [42]. The resolution achieved on the primary vertex position is $\sim 30\,\mu$m in the transverse plane and $\sim 50\,\mu$m in z [43].

The algorithms used to identify jets that are likely to contain a B-hadron are known as b-taggers. The input to these algorithms are tracks reconstructed from hits in the inner detector, which pass a series of quality cuts designed to reject fake tracks, badly measured tracks, tracks from the decay of long-lived particles such as K_s and tracks from interactions in the inner detector material such as photon conversions. These tracks are then associated with a jet using a jet p_{T} dependant cut on the angular separation between the track and the jet.

One type of b-tagger is based on the distance of closest approach of each track to the primary vertex, known as the 'impact parameter' (IP). IP3D is an impact parameter based b-tagger used in ATLAS [44]. It uses the 'impact parameter significance', IP/σ(IP), where σ(IP) is the error on the measurement of the IP, to b-tag jets, in order to reduce the effect of badly measured tracks. Another type of b-tagger tries to reconstruct the vertex of the B-hadron decay by successively combining pairs of tracks, removing those consistent with a long-lived particle decay or material interaction. The signed distance of the reconstructed secondary vertex from the primary vertex is used as the variable to distinguish b-jets from other jets. An example of this type of tagger used in ATLAS is SV1. A third type of b-tagger uses the topology of a B-hadron decay being followed by a C-hadron decay, under the assumption that the two decays take place along the flight path of the B-hadron. JetFitter [45] is a tagger which uses this technique. Recently, more sophisticated algorithms have been developed, which combine several individual tagging algorithms. JetFitterCombNN uses a neural network, whose inputs are the outputs of two b-taggers; IP3D and JetFitter.

The b-tagger used in this thesis is called MV1 and uses a neural network, with three inputs, which are the outputs of three individual b-taggers; IP3D, SV1 and JetFitterCombNN. The typical approach using b-taggers is to pick a point at which to cut on the output of the algorithm, which is a compromise between the efficiency to correctly tag true b-jets and the rejection of fake b-jets. The point used in this thesis is that where the overall predicted efficiency for true b-jets is 70%. This efficiency is measured in a control sample of data, as described in the next section, and varies as a function of the p_{T} and η of the jet. The predicted fake rates for this point are 20% for charm jets and 0.7% for light jets.

For the purposes of evaluating the b-tagging performance, the following definitions are made for simulated events. A true b-jet is defined as a jet, clustered from stable particles, excluding neutrinos and muons, using the anti-k_t algorithm with R = 0.4, which contains at least one B-hadron with $p_{\mathrm{T}} > 5$ GeV and $\Delta R < 0.3$ from the jet axis, where stable particles are defined as having a lifetime $>$ 10 ps. A charm jet is defined as a jet, not defined as a b-jet, which contains a charm-hadron, with $p_{\mathrm{T}} > 5$ GeV, within $\Delta R < 0.3$ of the jet axis. A light jet is defined as all jets which are not b-jets or charm jets.

2.7.1. B-Tagging Calibration and Uncertainties

For the chosen cut point of the b-tagging algorithm, the simulated efficiency for tagging true b-jets and for mistakenly tagging light and charm jets, is calibrated to that measured in data. For the b-tagging efficiency, this is done using $t\bar{t}$ events [46].

Selecting $t\bar{t}$ events, where one or both of the tops decay leptonically, gives a relatively pure data sample containing true b-jets. The efficiency is calibrated in bins of jet p_{T} and η and this is implemented by assigning a weight for each b-tagged jet based on its p_{T} and η. The event weight being the product of the weights for each b-tagged jet in the event. These weights are very close to 1, accounting for differences between data and simulated MC of $<$ 4%. The uncertainty on this calibrated efficiency is between 2-8%. The largest contributions to this uncertainty are: generator modelling uncertainties, such as the differences obtained using different generators and varying the parton-shower parameters; the uncertainty on the JES; the statistics of available $t\bar{t}$ data events. For b-jets with $p_{\mathrm{T}} > 300$ GeV, the $t\bar{t}$ data sample runs out of events and a large MC derived uncertainty of between 12-33% is added to the data-derived uncertainty.

The uncertainties are implemented as a set of 10 eigenvectors, where 10 is the number of p_{T} bins used in the calibration and the elements of the eigenvectors are the weights to apply to b-tagged b-jets in the p_{T} bins. This is intended to account for the correlations between the different p_{T} bins. The eigenvectors are obtained by forming the covariance matrix of the combined shift of all the sources of uncertainty in the individual p_{T} bins and then diagonalising its inverse. The eigenvector variations are treated as uncorrelated.

2.8. Measurement of the Integrated Luminosity

Both analyses in this thesis use a dataset of proton-proton collisions at a centre of mass energy of $\sqrt{s} = 8\,\mathrm{TeV}$, collected during 2012, with an integrated luminosity measured to be $19.5\,\mathrm{fb}^{-1}$. The relative uncertainty on this quantity is 2.8%. It is a slightly reduced dataset size compared with other ATLAS analyses, since there was a software bug in the b-jet triggers used in this thesis, that was in place for a short period of running at the start of 2012. The luminosity is measured using three specialised sub-detectors in the forward region of ATLAS [47]. It is calibrated using data taken during runs of the LHC when beam separation scans, known as Van de Meer scans [48], are performed.

Chapter 3.

Measurement of $Z \rightarrow b\bar{b}$

3.1. Introduction

All-hadronic final states are amongst the most challenging search channels at the LHC due to large QCD backgrounds and the poor experimental resolution of jets compared to leptons. Given the challenging nature of these search channels, it is important to validate them by measuring a known resonant process. This is the idea behind the analysis described in this chapter, which is measuring the Standard Model process; $Z \rightarrow b\bar{b}$. In addition, the $Z \rightarrow b\bar{b}$ peak could potentially be used as a testbed of techniques to improve the $b\bar{b}$ mass resolution, in order to increase the sensitivity of the $H \rightarrow b\bar{b}$ search and searches for other $b\bar{b}$ resonances.

This analysis measures the $Z \rightarrow b\bar{b}$ process in the so-called 'boosted' regime where the Z has high transverse momentum, specifically Z bosons with $p_{\mathrm{T}} > 200$ GeV. Z boson candidates are reconstructed using pairs of b-tagged anti-k_t, R=0.4 jets, which are close to each other in angular separation.

Looking for Z bosons with a high p_{T} results in a large reduction in the relative size of the background processes. The dominant background is from QCD multi-jet events, where there is a high p_{T} gluon 'splitting' to $b\bar{b}$. It is found that this background is not well modelled by leading-order MC event generators and so a data-driven background estimation is used instead.

3.1.1. Cross-Section Definition

The measured fiducial $Z \to b\bar{b}$ cross section, $\sigma_{Z\to b\bar{b}}$, is defined as having 2 b-jets resulting from the Z decay which satisfy:

- b-jet $p_{\mathrm{T}} > 40\,\mathrm{GeV}$;
- b-jet $|\eta| < 2.5$;
- ΔR(b-jet1,b-jet2) < 1.2;
- Dijet formed by adding the 4-vectors of the 2 b-jets with:
  - $p_T^{\mathrm{dijet}} > 200$ GeV;
  - $60 < m_{\mathrm{dijet}} < 160\,\mathrm{GeV}$;

where the definition of a b-jet in Section 2.7 is used.

The cross section is determined from the measured yield of $Z \to b\bar{b}$ events in the data, in the signal region, $N^{\mathrm{signal}}_{Z\to b\bar{b}}$, using the equation:

$$\sigma_{Z\to b\bar{b}} = \frac{N^{\mathrm{signal}}_{Z\to b\bar{b}}}{\mathcal{L}\cdot\mathcal{C}_{Z\to b\bar{b}}}, \tag{3.1}$$

where $\mathcal{C}_{Z\to b\bar{b}}$ is the value of the acceptance, defined as the predicted fraction of the reconstructed signal events passing the selection, to the events passing the cross section definition requirements. This acceptance factor and its associated uncertainty is discussed in detail in Section 3.5. $\mathcal{L}$ is the integrated luminosity of the data (19.5 ± 0.5 fb^{-1}).

3.2. MC Modelling of Signal and Background

The $Z \to b\bar{b}$ signal is modelled using two different MC generators: Sherpa and Pythia 8. Pythia 8 simulates the process at leading order using diagrams which have a Z boson and one extra parton in the final state, whilst Sherpa calculates the matrix element using diagrams with a Z boson and between 1 and 2 extra partons. Both MC samples are put through the full ATLAS detector simulation.

Since charm hadrons also have reasonably long lifetimes and so can be misidentified as b's by the b-tagging algorithms; there is a background from the process $Z \to c\bar{c}$. This contribution is modelled using Sherpa in the same way as for the $Z \to b\bar{b}$. It is simulated using a fast simulation of the ATLAS detector called AtlFastII. This uses the full simulation of the inner detector but uses a parameterisation of the calorimeters.

Another background contribution comes from hadronically decaying W bosons. These are simulated, at leading-order, using the $W + 1$ jet process with Pythia 8 and the full ATLAS detector simulation. These samples are normalised by multiplying by the ratio of next-to-leading-order to leading-order cross sections, known as a k-factor. This k-factor is derived using the MC generator MCFM [49] and has a value of 1.55.

The background from $t\bar{t}$ events is modelled at next-to-leading-order using the MC generator MC@NLO [26], interfaced with the LO generator Herwig+Jimmy [50, 51] for parton showering, underlying event and hadronisation. It is also put through the full ATLAS detector simulation. It is normalised to the calculated NNLO cross section of 253 pb [52–57].

By far the largest background comes from QCD events. This background is modelled using a data-driven method described in the next sections. There are some QCD MC samples used to assess the uncertainty of the modelling of the simulation of the triggers used. These are simulated with Pythia 8 using $2 \to 2$ diagrams in the matrix elements. They are put through the full ATLAS detector simulation.

3.3. Event Selection

3.3.1. Data Selection

Data is only considered if it was taken at a point in time where the detector passes a set of data quality requirements, in order to ensure all the relevant components of the detector were operating correctly. In both data and MC, events are vetoed that contain jets with $p_{\mathrm{T}} > 20$ GeV that fail the 'Looser' jet cleaning cuts as prescribed in [58]. This is intended to identify jets caused by noise in the detector, non-collision backgrounds and cosmic rays.

Both data and MC events are required to pass any of a specific set of 6 triggers, described in Section 2.3. None of the 6 triggers had a prescale applied to them, meaning that every event which passed any one of the triggers was recorded. The trigger efficiency for signal events which pass the selection detatiled in Section 3.3.2, estimated using SHERPA $Z \to b\bar{b}$ MC, is 88%. This predicted efficiency is shown as a function of various kinematic variables in Figure 3.1. The different turn-on regions in these plots come from the different kinematic requirements of the 6 triggers. Some inefficiency also comes from the use of b-tagging in the trigger, which is not as efficient as the b-tagging used in the offline selection on recorded events, after the full reconstruction. Figure 3.2 shows the predicted selected signal efficiency of the triggers as a function of dijet p_{T} but with the selection changed so that the offline b-tagging requirement is less efficient; specifically the 50% efficiency point is used instead of the 70% point. Using the less efficient b-tagging point in the selection, removes the relative inefficiency from the online b-tagging. Comparing this to Figure 3.1(a), which used the 70% efficiency point for b-tagging, it is seen that the inefficiency in the region ∼250-360 GeV, where the efficiency plateaus, is caused by the b-tagging in the trigger.

3.3.2. Preselection

The following event selection is referred to as the 'preselection'.

Jets are constructed from clusters of energy deposits in the calorimeters with the anti-k_t algorithm [35] using a radius parameter of $R = 0.4$. These jets are calibrated to the hadronic jet energy scale [38], as described in Section 2.6.2. Candidate b-jets from the Z decay are selected using the following criteria:

- $|\eta| < 2.5$;
- $p_{\mathrm{T}} > 40\,\mathrm{GeV}$;
- b-tagged using the MV1 tagging algorithm at the 70% efficiency point;
- if $|\eta| < 2.4$ and $p_T < 50\,\mathrm{GeV}$, then jet vertex fraction, JVF > 0.5;

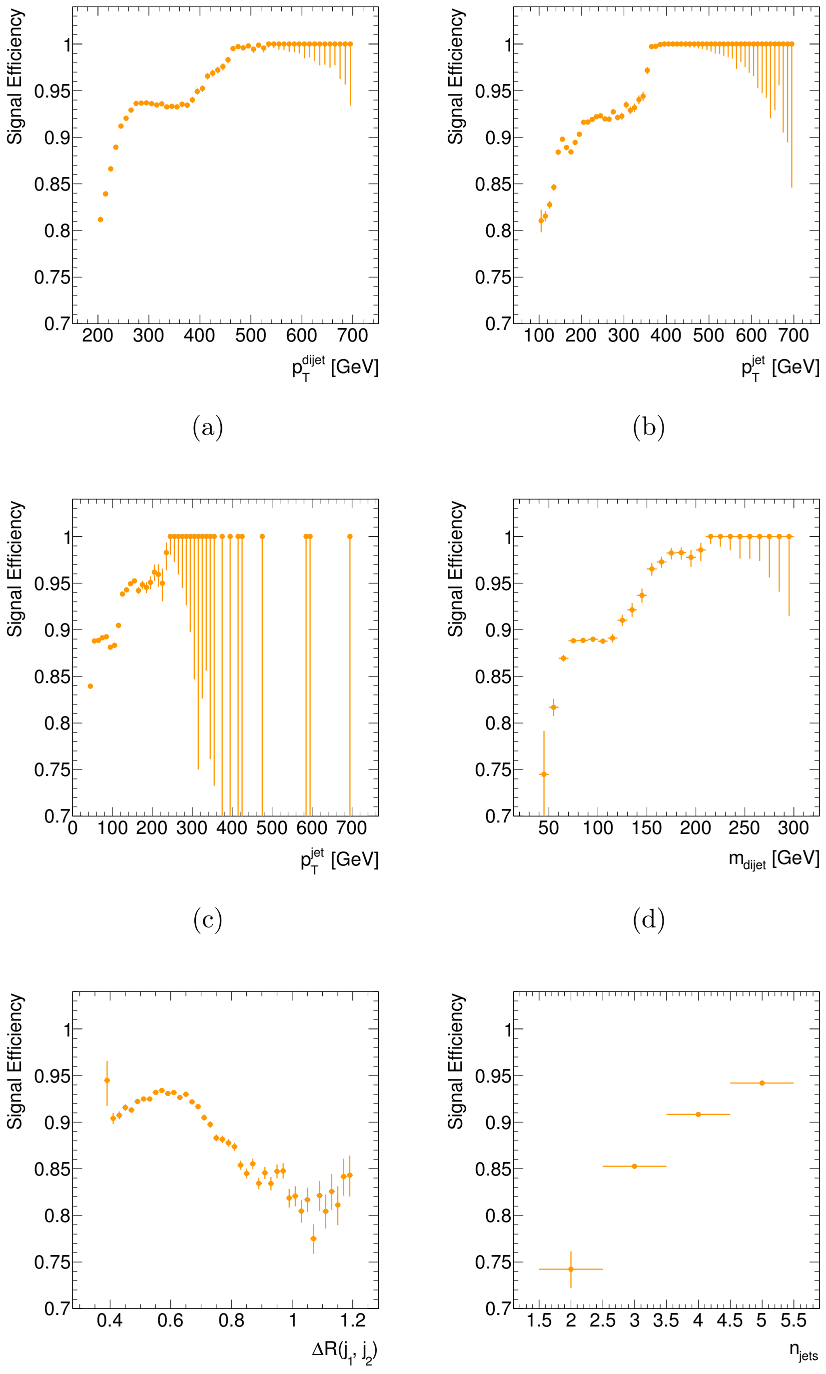

(a) (b)

(c) (d)

(e) (f)

Figure 3.1.: The efficiency of the trigger for selected Sherpa $Z \to b\bar{b}$ MC events. The efficiency is shown as a function of (a) the p_T of the b-tagged dijet, (b) the p_T of the leading jet of the dijet, (c) the p_T of the sub-leading jet of the dijet, (d) the mass of the dijet, (e) the angular separation between the two jets in the dijet, (f) the number of jets in the event.

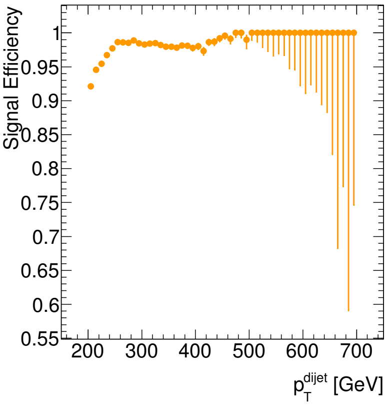

Figure 3.2.: The efficiency of the trigger for selected Sherpa $Z \to b\bar{b}$ MC events but using a modified selection which uses the 50% b-tagging efficiency point, as a function of the p_T of the b-tagged dijet.

where the meaning of JVF is described in Section 2.6.1 and the MV1 b-tagging algorithm is described in Section 2.7. From these selected jets, it is required that at least one dijet pair, formed by adding the 4-vectors of two jets, can be made which satisfies:

- Dijet $p_T > 200$ GeV.
- Angular separation of the two jets ΔR(jet1,jet2) < 1.2.

There are also other requirements on the number of jets in the event:

- $2 < n_\mathrm{jets} < 6$;
- $n_\mathrm{bjets} = 2$;

where n_jets are the number of jets with $p_T > 30\,\mathrm{GeV}$ and $|\eta| < 2.5$ and n_bjets is the number of those jets which are also b-tagged using the 70% efficiency point. These cuts are made to suppress the background from $t\bar{t}$ events. Figure 3.3 shows the n_jets and n_bjets distributions for data, $Z \to b\bar{b}$ MC and $t\bar{t}$ MC events which pass the b-tagged dijet selection but without the n_jets and n_bjets cuts applied. It is seen that these cuts reduce the contribution of $t\bar{t}$ without having a large impact on the signal efficiency.

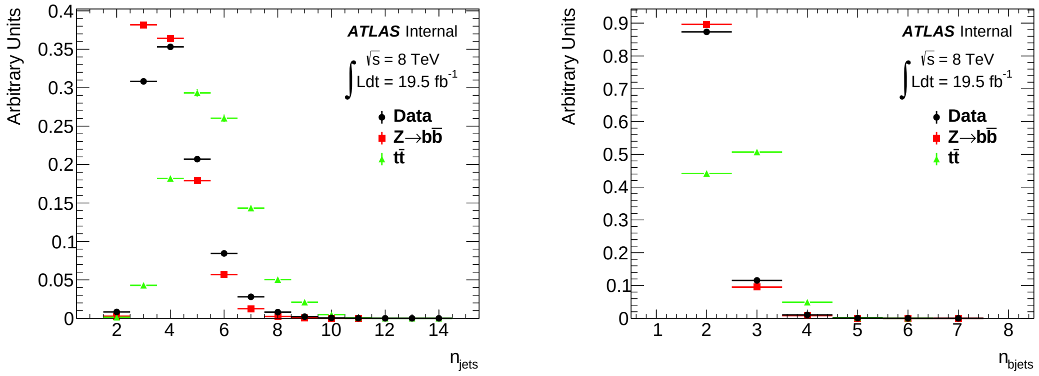

(a) (b)

Figure 3.3.: The distributions of (a) n_{jets} and (b) n_{bjets} for events passing the b-tagged dijet selection without the cuts on these variables. The histograms are normalised to equal area.

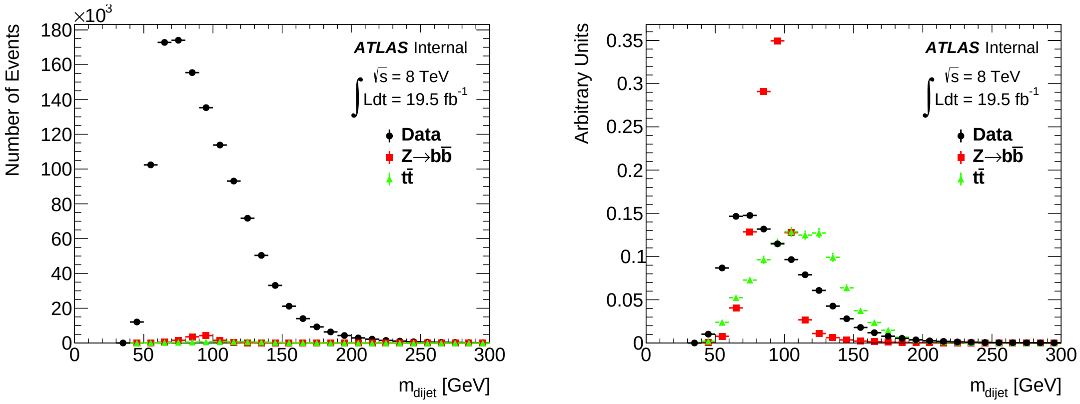

(a) (b)

Figure 3.4.: The dijet mass distribution of events passing the preselection. (a) The MC is normalised to the predicted number of events (b) The MC and data are normalised to equal area.

Applying the preselection criteria to the 2012 data results in 1179947 events. Figure 3.4 shows the distribution of the invariant mass of the b-tagged dijet in the data, $Z \to b\bar{b}$ and $t\bar{t}$ MC. After applying the preselection, the signal to background ratio (s/b) is just 1.0% overall and 2.4% when restricting to a signal mass window of 80 - 110 GeV.

3.3.3. Signal and Control Regions

In order to increase the s/b and obtain a data-driven background model, an additional set of kinematic cuts are used to separate the data into a signal-enhanced 'signal region' and a signal-depleted 'control region'.

The kinematic variables used are two which are found to have good discrimination between signal and background and are also minimally correlated with m_{dijet}, which is necessary in order to use the m_{dijet} distribution in the control region to model the background in the signal region. The variables are:

- $|\eta|$ of the b-tagged dijet.
- $|\Delta\eta|$ between the b-tagged dijet and the balancing jet.

The balancing jet is defined as the jet in the event (with $p_T > 30\,\mathrm{GeV}$ and $|\eta| < 2.5$) which, when added vectorially to the b-tagged dijet, results in a combined p_{T} closest to 0.

Figures 3.5(a) and 3.5(b) show the distributions of these two variables in events passing the preselection, comparing $Z \to b\bar{b}$, $t\bar{t}$ MC and data. There is significant difference in the distributions in signal and the QCD background dominated data. The two variables have some correlation between them and so, in order to maximise the discrimination between signal and background, an Artificial Neural Network (ANN) combining the two variables is used.

The ANN is trained using events which pass the preselection in SHERPA $Z \to b\bar{b}$ MC as signal. For background, events in data are used, which pass the preselection and are outside of the dijet mass window 80 - 110 GeV. Using data to train the ANN reduces the dependency on the MC modelling of these two variables and since the variables are approximately uncorrelated with mass, it is possible to use the data outside of the signal mass region, which reduces the signal contamination in this background sample to a negligibly small level. The distribution of the ANN output variable, $\mathcal{S}_{\mathcal{NN}}$, in data, signal and $t\bar{t}$ events, which pass the preselection, is shown in Figure 3.5(c).

The signal region is defined as events passing the preselection with $\mathcal{S}_{\mathcal{NN}} > 0.58$ and the control region is defined as events passing the preselection with $\mathcal{S}_{\mathcal{NN}} < 0.45$. The numbers of events in these regions in data and MC are listed in Table 3.1. These

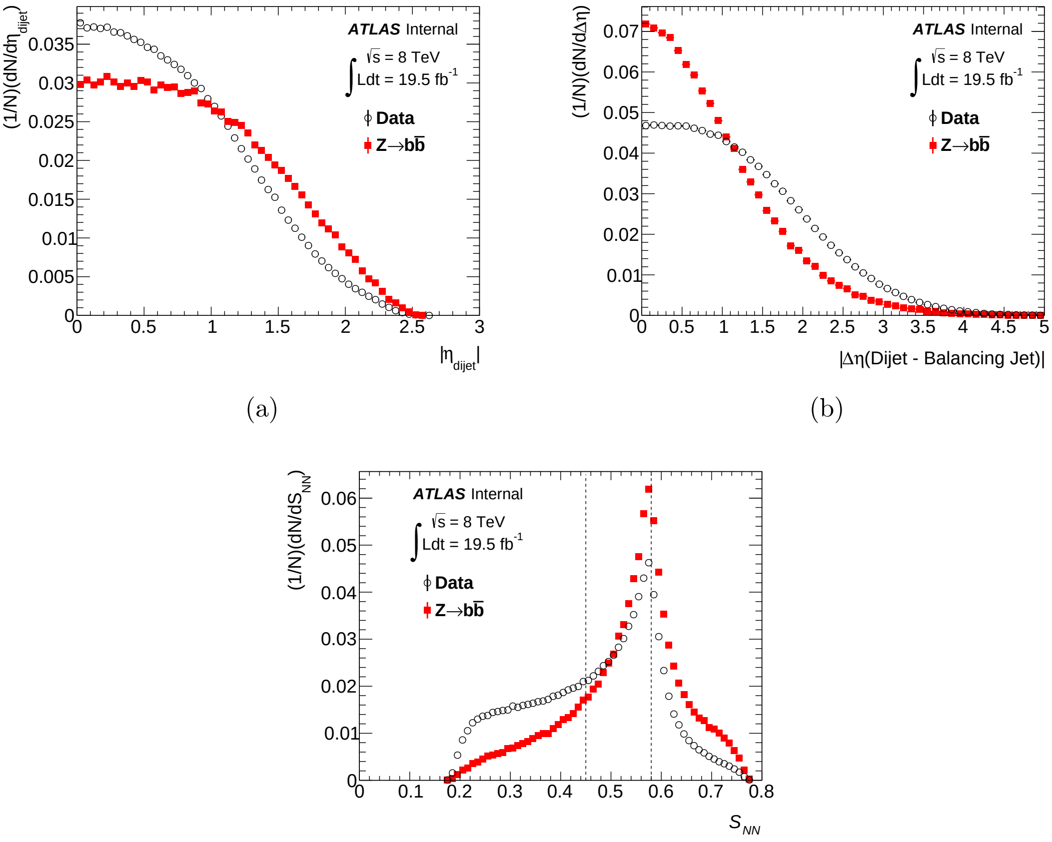

(a)

(b)

(c)

Figure 3.5.: (a) Distribution of the $|\eta|$ of the b-tagged dijet in events passing the preselection. (b) Distribution of the $|\Delta\eta|$ between the dijet and the balancing jet, in events passing the preselection. (c) Distribution of the output of the ANN, $\mathcal{S}_{\mathcal{NN}}$, which uses the variables in (a) and (b) as inputs. The dashed lines denote the cuts on $\mathcal{S}_{\mathcal{NN}}$ which define the signal and control regions.

	After Preselection	Signal Region $\mathcal{S}_{\mathcal{NN}} > 0.58$	Control Region $\mathcal{S}_{\mathcal{NN}} < 0.45$
Number of Data Events	1179947	236172	474810
Number of Signal $Z \rightarrow b\bar{b}$ Events	12204	4219	2583
Number of $t\bar{t}$ Events	5533	1022	2382
Number of $Z \rightarrow c\bar{c}$ Events	1207	342	298
Number of $W \rightarrow \overline{q}q'$ Events	695	239	144
s/b	1.0%	1.8%	0.5%
s/b ($80 < m_{\text{dijet}} < 110\,\text{GeV}$)	2.4%	4.2%	1.0%
s/$\sqrt{\text{b}}$ ($80 < m_{\text{dijet}} < 110\,\text{GeV}$)	14.9	11.7	4.9

Table 3.1.: The number of data and (SHERPA) predicted signal events in the signal and control regions. The s/b values are likely an underestimate since they use the value of the signal cross section predicted by SHERPA which is smaller than the NLO prediction. The background is estimated by subtracting the signal from the data.

points are chosen as a compromise between the number of events in the signal/control regions and the signal purity/contamination in those regions.

Figure 3.6(a) shows the dijet mass distribution in data events in the signal region and in the control region, where the control region has been normalised to the signal region outside the Z mass window. An excess of data events in the Z mass window is seen in the signal region compared to the control region. The ratio of these two histograms is plotted in Figure 3.6(b), with the Z mass window excluded. No significant bias in the control region description of the signal region m_{dijet} distribution is seen.

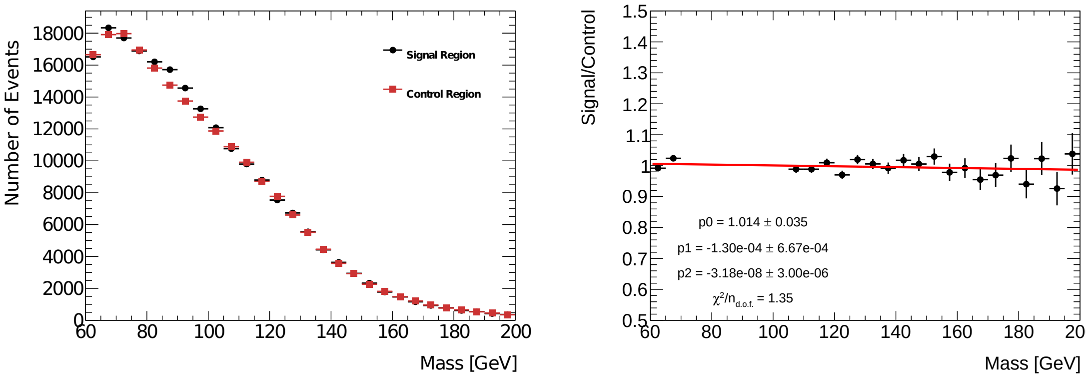

(a) (b)

Figure 3.6.: (a) The dijet mass distribution in data events in the signal region and in the control region, where the control region has been normalised to the signal region outside the Z mass window. (b) The ratio of (a) with the Z mass window excluded, fitted with a linear function.

3.4. Determining the Number of $Z \to b\bar{b}$ Events in Data

To measure the number of $Z \to b\bar{b}$ events in the signal region, in data, $N^{\text{signal}}_{Z\to b\bar{b}}$, the distributions of the dijet invariant mass, m_{dijet}, in both the control and signal regions, are fitted simulataneously with a combined signal+background model. This section describes the details of that procedure.

3.4.1. Signal and Background Models

The dijet invariant mass distribution for $Z \to b\bar{b}$ events is modelled as the sum of three Gaussian functions, shown in Figure 3.7. This function is chosen because it is found to model the MC prediction well. The values of the parameters of this function are determined from a fit to the $Z \to b\bar{b}$ MC, except the mean value of the distribution. The mean is parameterised by the value m_{peak}, which is the mean of the central Gaussian. The means of the other two Gaussian functions are coupled to the mean of the central Gaussian by fixing them to be the difference from m_{peak} obtained in the fit to $Z \to b\bar{b}$ MC. Setting m_{peak} as a free parameter reduces the impact of the uncertainty on the jet energy scale. The overall normalisation of this function is allowed to float in the fit, in order to extract $N^{\text{signal}}_{Z\to b\bar{b}}$. The function, with its parameter values determined by fitting to SHERPA MC, is used for the baseline result and the function fitted to PYTHIA 8 MC is used to assess the systematic uncertainty on the MC modelling of the m_{dijet} distribution, as described in Section 3.4.4.

Figure 3.8 shows the $Z \to b\bar{b}$ signal model fitted to the MC in the signal and the control region. There are small differences between the fitted functions in the two regions and so the values of the parameters of the signal models used are distinct in the two regions, with both fixed to the values obtained with the fit to the MC in the corresponding region.

The backgrounds from $Z \to c\bar{c}$ and $W \to \bar{q}q'$ are also modelled using the same functional form of the sum of three Gaussians. These models are shown in Figure 3.9. In both cases the mean value of the function is fixed relative to the mean of the $Z \to b\bar{b}$ model. Since the $Z \to c\bar{c}$ is a different decay channel of the Z, which has branching ratios which have been well measured at LEP and the SLC, the normalisation of the $Z \to c\bar{c}$ model is fixed as a fraction of the $Z \to b\bar{b}$ normalisation. This is done separately in the signal and control regions using the fraction predicted by SHERPA using the simulated b-tagging efficiency and charm mis-tagging efficiency. The normalisation of the $W \to \bar{q}q'$ model is set to the cross section predicted by PYTHIA 8, multiplied by the k-factor of 1.55 derived using MCFM.

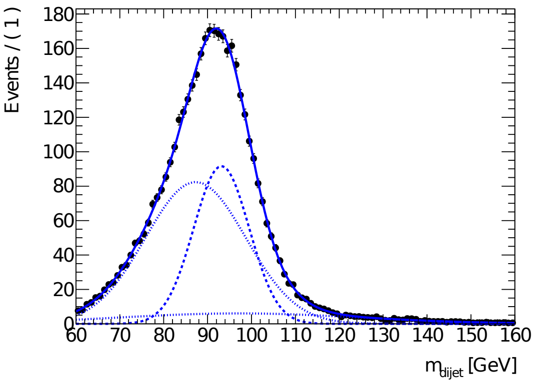

(a)

Figure 3.7.: The m_{dijet} distribution in $Z \to b\bar{b}$ MC for selected events in the signal region. The signal model is shown as the solid line. It is a sum of three Gaussian functions, with the shape parameters fitted to the MC. The individual Gaussians are shown as the dashed lines. The MC generator used is SHERPA.

The background from $t\bar{t}$ is modelled using a single Gaussian function; the fit to MC@NLO MC is shown in Figure 3.10. The normalisation is fixed to the next-to-next-to-leading-order + next-to-next-to-leading-log (NNLO+NNLL) predicted cross section [52–57].

The model for the QCD background is a 7th degree Bernstein polynomial [59]:

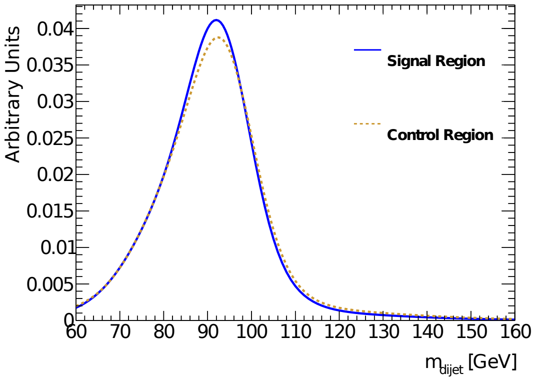

(a)

Figure 3.8.: A comparison of the $Z \to b\bar{b}$ model of the m_{dijet} distribution in the signal and control regions. The MC generator used is Sherpa.

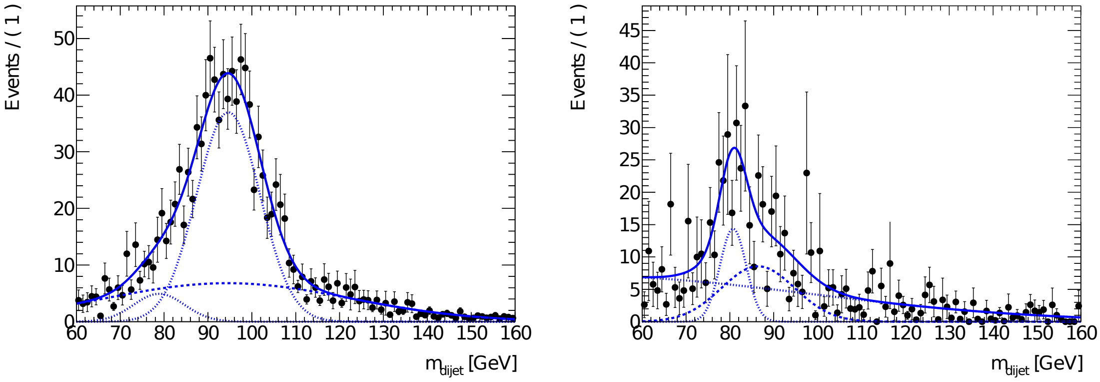

(a) $Z \to c\bar{c}$ (b) $W \to \bar{q}q'$

Figure 3.9.: The m_{dijet} distribution in $W \to \bar{q}q'$ and $Z \to c\bar{c}$ MC for selected events in the signal region. The background model is shown as the solid line. It is a sum of three Gaussian functions, with the shape parameters fitted to the MC. The individual Gaussians are shown as the dashed lines.

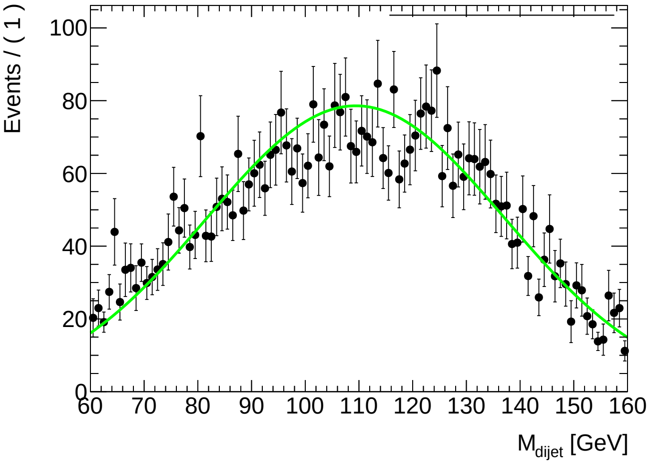

Figure 3.10.: The m_{dijet} distribution in $t\bar{t}$ MC for selected events in the signal region. The background model is shown as the solid line. It is a Gaussian function.

$$\mathcal{F}_{\text{QCD}}(x) = k_0 B_{0,7}(x) + k_1 B_{1,7}(x) + k_2 B_{2,7}(x) + k_3 B_{3,7}(x) + k_4 B_{4,7}(x) + k_5 B_{5,7}(x) + k_6 B_{6,7}(x) + k_7 B_{7,7}(x) \quad (3.2)$$

where $B_{i,n}(x) = \frac{n!}{i!(n-i)!} x^i (1-x)^{n-i}$, and k_i are the Bernstein polynomial coefficients, which are determined using the fit to data and where x is a transform of the m_{dijet} axis such that x is between 0 and 1. The coefficients, k_i, are restricted to be ≥ 0. The second Bernstein coefficient k_2 is fixed to 0, since this significantly improves the fit stability. There are seven free parameters in the background model. The number of terms required in the function is determined by testing the $\chi^2/\text{n}_{\text{d.o.f.}}$ with an increasing number of terms and picking the point at which the $\chi^2/\text{n}_{\text{d.o.f.}}$ stops improving with the addition of an extra term. Bernstein polynomials are used, since their positive-definite nature makes them well-behaved when fitting probability density functions.

Figure 3.11 shows the QCD model fitted to the data in the control region. The data in the control region is predicted to be dominated by QCD background events. The model describes the data well, with a $P\left(\chi^2, \text{n}_{\text{d.o.f.}}\right)$ of 0.33.

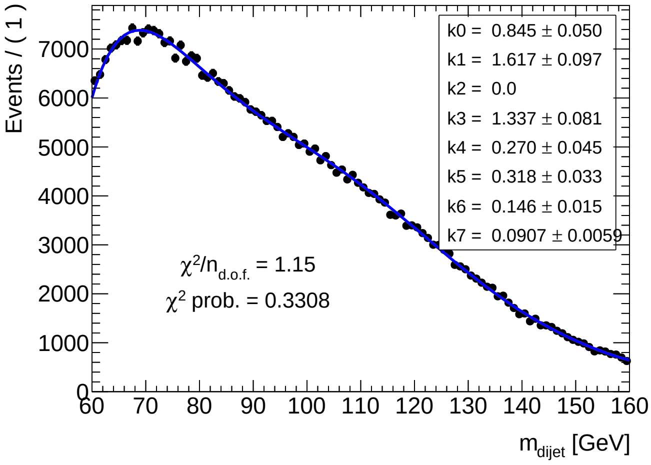

Figure 3.11.: The distribution of m_{dijet} in data, in the control region, fitted with the QCD background model; a 7th degree Bernstein polynomial.

3.4.2. Simultaneous Fit to the Control and Signal Regions

The functions that make up the $Z \to b\bar{b}$ signal and the different background components are used in an extended maximum likelihood [60] fit to the data in both the signal and control regions simultaneously. Histograms of the m_{dijet} distribution using a bin width of 1 GeV are fitted. There are 10 free parameters in the fit:

- 7 coefficients of the Bernstein polynomial used for the QCD background model normalised to the control region. The shape is common to both the signal and control regions.
- The mean of the central Gaussian of the $Z \to b\bar{b}$ signal model, m_{peak}. Common to both the signal and control regions.
- The ratio of the number of QCD background events in the signal region to the control region, $\mathrm{N}_{\mathrm{QCD}}^{\mathrm{signal}}/\mathrm{N}_{\mathrm{QCD}}^{\mathrm{control}}$.
- The number of $Z \to b\bar{b}$ events in the signal region, $N_{Z\to b\bar{b}}^{\mathrm{signal}}$.

The shape parameters of the QCD background model are common between the signal and control regions, meaning that the function is exactly the same in both regions other than the normalisations, which are different. This allows the QCD background dominated control region to constrain the shape of the QCD background in the signal region.

There is some amount of $Z \to b\bar{b}$ signal present in the control region, the size of this contamination predicted by MC is shown in Table 3.1, it is at a fraction that is too small to be determined by a fit. The number of $Z \to b\bar{b}$ events in the control region, $N^{\text{control}}_{Z\to b\bar{b}}$, is instead determined by fixing the ratio of the number of $Z \to b\bar{b}$ events in the signal region to that in the control region:

$$R_Z = \frac{N^{\text{control}}_{Z\to b\bar{b}}}{N^{\text{signal}}_{Z\to b\bar{b}}}. \tag{3.3}$$

R_Z is fixed to the value predicted by Sherpa MC. This constrains the number of $Z \to b\bar{b}$ events in the control region to be $N^{\text{control}}_{Z\to b\bar{b}} = R_Z \, N^{\text{signal}}_{Z\to b\bar{b}}$. The Sherpa $Z \to b\bar{b}$ MC modelling of $\mathcal{S}_{\mathcal{NN}}$, which defines the signal and control regions, is tested using $Z \to \mu\mu$ events in data, as described in Section 3.5.1.

3.4.3. Results of the Fit

Figure 3.12 shows the results of the simultaneous extended maximum likelihood fit to the data. Table 3.2 shows the fitted values and associated errors of the individual parameters of the fit, for both the Pythia 8 and Sherpa $Z \to b\bar{b}$ signal models. Studies are carried out using pseudo-experiments to test the accuracy of the fit and assess any bias. The background and signal models are randomly sampled from, in both the signal and control regions, generating the number of events from the fit to data, and these are combined to make a single pseudo-experiment. The pseudo-experiment is fitted with the same procedure as the data. In total 21000 pseudo-experiments are generated. The results from the pseudo-experiment fits show that the bias on $N^{\text{signal}}_{Z\to b\bar{b}}$ is negligibly small and that the uncertainties that the fit returns are accurate.

Figure 3.12 shows the fitted value of ΔM_Z, which is defined as the signed difference between the value of m_{peak} obtained from the fit to data and the value predicted by MC:

Fit Parameter	Value in SHERPA Fit	Value in PYTHIA 8 Fit
QCD k_0	0.84 ± 0.17	0.84 ± 0.03
QCD k_1	1.58 ± 0.32	1.57 ± 0.05
QCD k_3	1.19 ± 0.22	1.18 ± 0.07
QCD k_4	0.41 ± 0.12	0.42 ± 0.06
QCD k_5	0.23 ± 0.04	0.22 ± 0.05
QCD k_6	0.17 ± 0.04	0.17 ± 0.02
QCD k_7	0.085 ± 0.017	0.085 ± 0.004
$N^{\mathrm{signal}}_{Z\to b\bar{b}}$	6418 ± 641	6279 ± 623
m_{peak}	91.66 ± 0.74	91.36 ± 0.72
$\mathrm{N}^{\mathrm{control}}_{\mathrm{QCD}}$	403980 ± 776	404074 ± 769
$\mathrm{N}^{\mathrm{signal}}_{\mathrm{QCD}}$	197330 ± 818	197481 ± 801

Table 3.2.: The fitted value of each parameter of the signal+background model. Shown for the two different $Z \to b\bar{b}$ models from the PYTHIA 8 and SHERPA MC generators. The fit is carried out in the restricted dijet mass range $60 < m_{\mathrm{dijet}} < 160\,\mathrm{GeV}$.

$$\Delta M_Z = m^{\mathrm{fitted}}_{peak} - m^{\mathrm{MC}}_{peak} \tag{3.4}$$

The compatibility of ΔM_Z with 0 is assessed in Section 3.4.5 where the systematic uncertainty on the MC prediction of m_{peak} is assessed.

3.4.4. Systematic Uncertainties on the Fit Results

Table 3.3 shows the size of the uncertainty from different sources on the fitted number of $Z \to b\bar{b}$ events, $N^{\mathrm{signal}}_{Z\to b\bar{b}}$, and the fitted $Z \to b\bar{b}$ peak position, relative to the prediction ΔM_Z.

The uncertainties on the results of the fit arising from the uncertainty on the jet energy scale, described in Section 2.6.2, and the b-tagging efficiency, described in Section 2.7.1, are calculated by applying the $\pm 1\sigma$ eigenvector variations to the $Z \to b\bar{b}$ MC and repeating the simultaneous fit. The uncertainty on the fit results from the

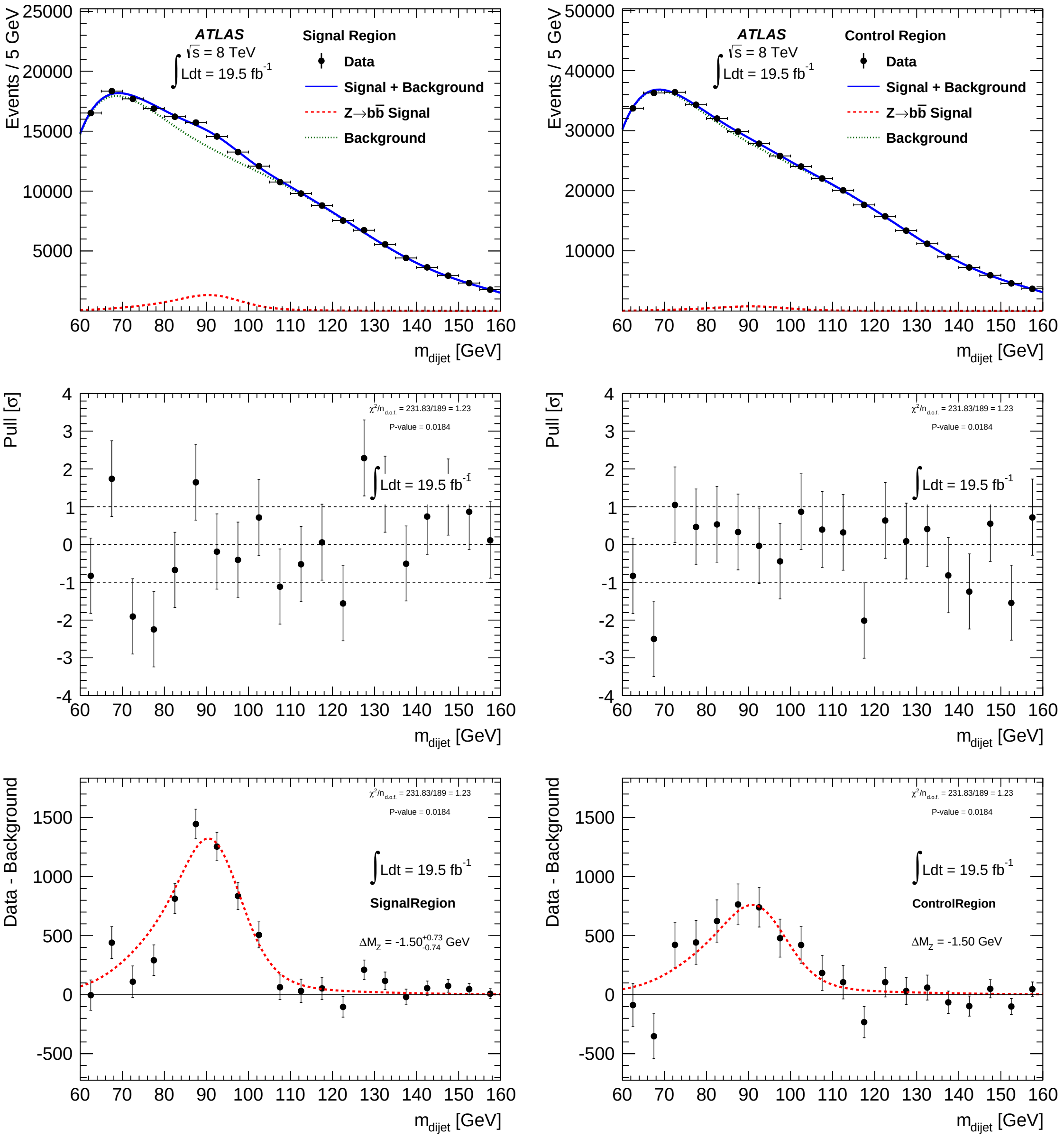

Figure 3.12.: The result of the simultaneous extended maximum likelihood fit to the data. The Sherpa $Z \to b\bar{b}$ signal model is used. The LHS shows the signal region, the RHS shows the control region. The data is shown as black points. The top row is the m_{dijet} distribution, the middle row is the pull in each bin and the bottom row is the m_{dijet} distribution with the background prediction subtracted from the data.

uncertainty on the jet energy resolution, described in Section 2.6.2, is calculated by smearing the measured energy of the jets, in simulated events, to increase the resolution to the $+1\sigma$ point and then symmetrising the resultant uncertainty.

Systematic Source	$\Delta N^{\text{signal}}_{Z\to b\bar{b}}$	$\Delta N^{\text{signal}}_{Z\to b\bar{b}}$ (%)	$\Delta\Delta M_Z$ (GeV)
JES	+194/-95	+3.0/-1.5	+3.33/-2.24
JER	±341	±5.3	±0.2
B-Tagging Efficiency	±8	±0.1	0.0
Signal m_{dijet} Shape	±139	±2.2	±0.1
Signal $\mathcal{S}_{\mathcal{NN}}$ Modelling	±58	±0.9	0.0
$Z \to c\bar{c}$ Normalisation	±23	±0.4	0.0
$t\bar{t}$ Normalisation	±75	±1.2	±0.1
$W \to$ hadrons Normalisation	±62	±1.0	±0.1
Control Region Bias	+331/-330	±5.2	+0.32/-0.34
Functional Form	negl.	negl.	negl.

Table 3.3.: The individual systematic uncertainties on the fitted number of $Z \to b\bar{b}$ events in the signal region, $N^{\text{signal}}_{Z\to b\bar{b}}$, and on the difference between the fitted and predicted position of the Z peak, ΔM_Z.

Figure 3.13 shows the effect of these systematic shifts on the signal model. For illustrative purposes the JES and b-tagging uncertainty shifts are shown as the total shift rather than the eigenvector component shifts which are actually used to derive the uncertainty. The significant shift in the position of the Z peak from the JES shifts has no impact on the fit results, since m_{peak} is a free parameter in the fit.

Another uncertainty on the m_{dijet} shape comes from the MC modelling of the $Z \to b\bar{b}$ process. This is evaluated by comparing the results of the fit using the signal model fitted to Pythia 8 MC to the baseline. It is referred to as 'Signal m_{dijet} Shape' in Table 3.3 and has a value of 2.2%. Figure 3.14 shows a comparison of the m_{dijet} distribution from the two generators.

Other than the m_{dijet} shape, the other way systematic uncertainty enters into the fit results, is through the value of R_Z, the relative fraction of $Z \to b\bar{b}$ events in the control region to the signal region. This is evaluated using the $Z \to \mu\mu$ data, described in Section 3.5.1. Table 3.4 shows the value of R_Z calculated in $Z \to \mu\mu$ data and MC, using the analogous variables as inputs to the ANN. This comparison is made for different values of the dimuon p_{T} cut, since there is no one-to-one correspondence to a value of the dijet p_{T} cut in the $Z \to b\bar{b}$ case. The largest difference between the data and MC is 2.8%, the systematic uncertainty on

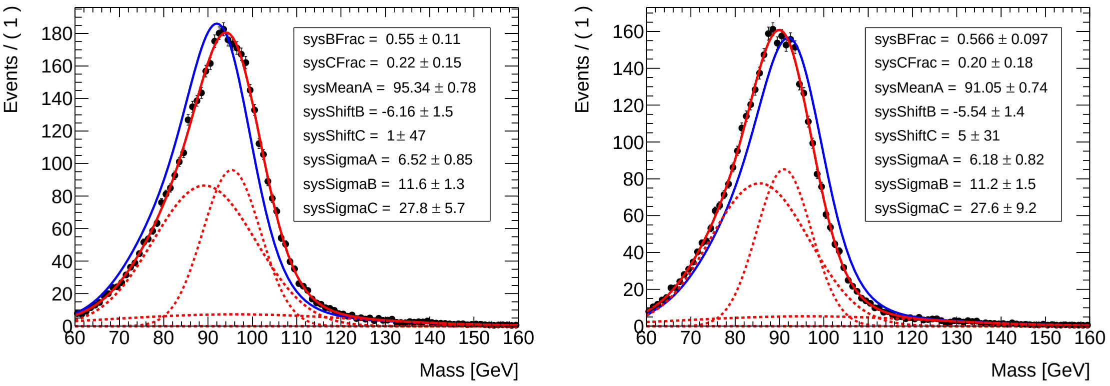

(a) JES Up (b) JES Down

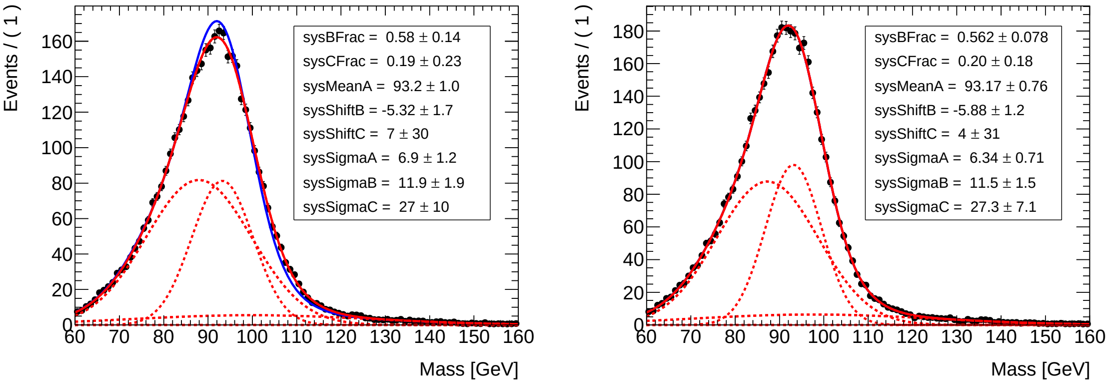

(c) JER (d) B-tagging Efficiency Up

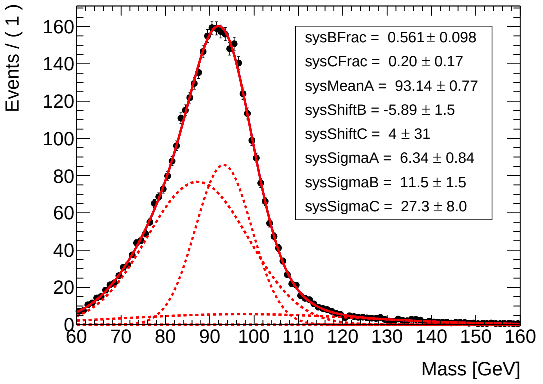

(e) B-tagging Efficiency Down

Figure 3.13.: The signal models obtained after applying the various systematic uncertainties on the simulated events. The black points show the shifted Sherpa $Z \to b\bar{b}$ MC and the red line shows the fitted signal model. The baseline value of the signal model is shown in blue, for comparison.

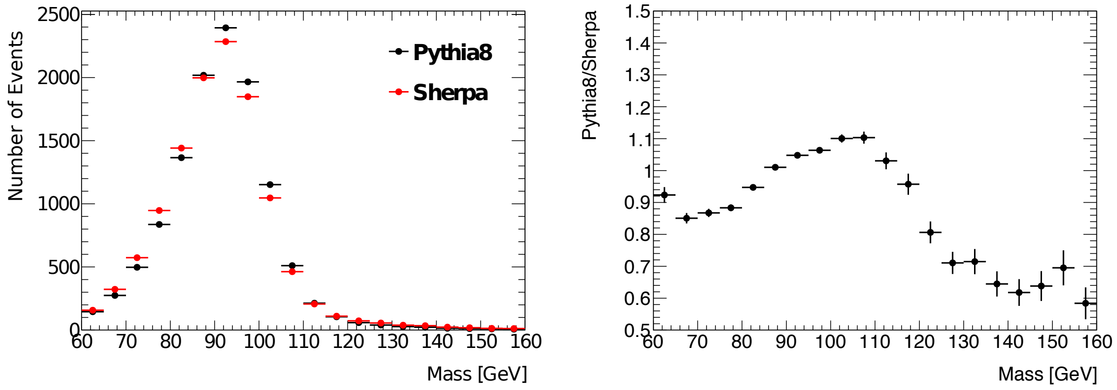

(a) (b)

Figure 3.14.: (a) The $Z \to b\bar{b}$ m_{dijet} distributions predicted by SHERPA and PYTHIA 8, normalised to equal area. (b) The ratio of PYTHIA 8 to SHERPA in (a).

Dimuon p_{T} cut	Data R_Z	SHERPA R_Z	ΔR_Z (Data-SHERPA) (%)
$p_{\text{T}} > 150$ GeV	0.454 ± 0.008	0.467 ± 0.003	-2.8
$p_{\text{T}} > 200$ GeV	0.458 ± 0.014	0.470 ± 0.005	-2.6
$p_{\text{T}} > 250$ GeV	0.487 ± 0.024	0.494 ± 0.008	-1.4

Table 3.4.: The value of R_Z, in $Z \to \mu\mu$ + jet events in data and in SHERPA MC, for different values of the minimum dimuon p_{T} cut.

R_Z is taken as a conservative 4%. Repeating the fit with ±4% variations on R_Z results in an uncertainty of 0.9% on the fitted number of $Z \to b\bar{b}$ events.

The uncertainty on the normalisation of the small $t\bar{t}$ and $W \to \bar{q}q'$ components in the fit is taken as a conservative 50%. They are both varied separately in the different regions and varied simultaneously in the two regions and the largest deviation in $N^{\text{signal}}_{Z \to b\bar{b}}$ is taken as the uncertainty. The size of the uncertainties is found to be ±1.2% and ±1.0% respectively.

Another source of uncertainty on $N^{\text{signal}}_{Z \to b\bar{b}}$ comes from the modelling of the rate of charm hadrons passing the b-tagging for simulated $Z \to c\bar{c}$ events. This is evaluated using the corresponding uncertainty eigenvectors which are derived using D* decays [61]. This is treated as uncorrelated with the corresponding uncertainty on the efficiency of B-hadrons to pass the b-tagging.

Control Region Bias

The fitting procedure relies on the approximation that the control region provides an unbiased m_{dijet} distribution in the QCD background relative to the signal region. Figure 3.6(b) shows that the control region m_{dijet} distribution does give a good description of the m_{dijet} distribution in the signal region. However, this needs to be quantified, since due to the low s/b of this measurement, even a small bias could produce a significant change in the observed $N^{\text{signal}}_{Z\to b\bar{b}}$.

Figure 3.15 shows the ratio of the m_{dijet} distributions in the signal to the control region, when the value of the cut on $\mathcal{S}_{\mathcal{NN}}$, which defines the control region, is varied. This is seen to introduce a bias in the description of the background. This effect is used to estimate the uncertainty from the approximation that the m_{dijet} distribution of the QCD background is unbiased in the control region with respect to the signal region.

Values of $N^{\text{signal}}_{Z\to b\bar{b}}$ are extracted from the fit using different values of the cut on $\mathcal{S}_{\mathcal{NN}}$. Table 3.5 shows the results of the different fits. Values of $N^{\text{signal}}_{Z\to b\bar{b}}$ are taken into account if the $P\left(\chi^2, \text{n}_{\text{d.o.f.}}\right)$ of the fit is > 0.001, taken as an arbitrary cut-off on fit quality. This covers the range $\mathcal{S}_{\mathcal{NN}} < [0.40, 0.50]$, and corresponds to a range in the gradients of the linear fits of the signal to control region ratio from 1.40×10^{-4} to -3.50×10^{-4}, where the baseline value is $(-1.37 \pm 1.10) \times 10^{-4}$ and the linear fits are for illustrative purposes only. This results in a systematic uncertainty on $N^{\text{signal}}_{Z\to b\bar{b}}$ of ± 330 events ($\pm 5.1\%$) and on ΔM_Z of $\pm 0.33\,\text{GeV}$.

QCD Background Function Choice

A 7th degree Bernstein polynomial is used to model the QCD background. There is an uncertainty on $N^{\text{signal}}_{Z\to b\bar{b}}$, of $\pm$ 11%, from the statistical uncertainties on the fitted parameters of that function, however it could be possible that a different choice of function could give a result outside of those uncertainties. In order to assess the extent of the dependency of the result on the choice of the QCD functional form, several different functional forms were used to model the QCD background and 4 were found which resulted in a good fit to the control region data m_{dijet} distribution. The 4 functions are:

$\mathcal{S}_{\mathcal{NN}} <$	$\chi^2/\mathrm{n}_{\mathrm{d.o.f.}}$ (p-value)	$N_{Z\to b\bar{b}}$	$\Delta \left\langle \mathrm{N}_{\mathrm{Z\to b\bar{b}}} \right\rangle$	ΔM_Z [GeV]	$\Delta \langle \delta M_Z \rangle$ [GeV]
0.39	1.36 (0.0007)	5942	-476	-1.19	+0.31
0.40	1.33 (0.0016)	6088	-330	-1.18	+0.32
0.41	1.30 (0.0031)	6243	-175	-1.23	+0.27
0.42	1.23 (0.0186)	6174	-244	-1.33	+0.17
0.43	1.25 (0.0102)	6284	-134	-1.21	+0.29
0.44	1.25 (0.0104)	6347	-71	-1.37	+0.13
0.45	1.23 (0.0184)	6418	-	-1.50	-
0.46	1.24 (0.0139)	6436	+18	-1.49	+0.01
0.47	1.31 (0.0028)	6513	+95	-1.63	-0.13
0.48	1.32 (0.0023)	6596	+178	-1.82	-0.32
0.49	1.31 (0.0027)	6664	+246	-1.85	-0.35
0.50	1.34 (0.0013)	6749	+331	-1.84	-0.34
0.51	1.37 (0.0006)	6685	+267	-2.04	-0.54

Table 3.5.: The results of the simultaneous maximum likelihood fit, varying the value of the cut on $\mathcal{S}_{\mathcal{NN}}$ which defines the control region. The baseline fit defines the control region as $\mathcal{S}_{\mathcal{NN}} < 0.45$.

- $\mathcal{F}_{\mathrm{A}}$: An 8th degree Bernstein polynomial where the k_2, k_4 and k_6 coefficients are all fixed to zero, leaving 6 free parameters.
- $\mathcal{F}_{\mathrm{B}}$: An 8th degree Bernstein polynomial where the k_2 coefficient is fixed to zero, leaving 8 free parameters.
- $\mathcal{F}_{\mathrm{C}}$: A 9th degree Bernstein polynomial where the k_4 coefficient is fixed to zero, leaving 9 free parameters.
- $\mathcal{F}_{\mathrm{D}}$: A Lognormal function convoluted with a 4th degree Bernstein polynomial. This has 7 free parameters.

Since there are some number of signal events in the control region, it is important that the function chosen to describe the QCD background has the freedom to accommodate a reasonable range in the amount of signal in the control region, whilst still giving a good fit to the data. In order to assess this, the control region is fitted with a signal + background model where the position of the $Z \to b\bar{b}$ peak is fixed to the MC prediction and the number of $Z \to b\bar{b}$ events in the control region, $N^{\mathrm{control}}_{Z\to b\bar{b}}$,

Functional Form	No. Free Parameters	$N^{\text{control}}_{Z\rightarrow b\bar{b}}$ =196 Fit $\chi^2/\text{n}_{\text{d.o.f.}}$	$N^{\text{control}}_{Z\rightarrow b\bar{b}}$ =1960 Fit $\chi^2/\text{n}_{\text{d.o.f.}}$	$N^{\text{control}}_{Z\rightarrow b\bar{b}}$ =3920 Fit $\chi^2/\text{n}_{\text{d.o.f.}}$	$N^{\text{control}}_{Z\rightarrow b\bar{b}}$ 7840= Fit $\chi^2/\text{n}_{\text{d.o.f.}}$	$N^{\text{control}}_{Z\rightarrow b\bar{b}}$ =11760 Fit $\chi^2/\text{n}_{\text{d.o.f.}}$
$\mathcal{F}_{\text{QCD}}$ (Default)	7	1.14 (0.168)	1.10 (0.234)	1.09 (0.254)	1.17 (0.122)	1.39 (0.008)
$\mathcal{F}_{\text{A}}$	6	1.26 (0.045)	1.24 (0.056)	1.28 (0.037)	1.51 (0.001)	1.96 (0.000)
$\mathcal{F}_{\text{B}}$	8	1.27 (0.045)	1.27 (0.043)	1.30 (0.028)	1.40 (0.007)	1.55 (0.001)
$\mathcal{F}_{\text{C}}$	9	1.13 (0.194)	1.15 (0.154)	1.19 (0.102)	1.36 (0.014)	1.60 (0.000)
$\mathcal{F}_{\text{D}}$	7	1.11 (0.213)	1.10 (0.243)	1.09 (0.251)	1.13 (0.180)	1.24 (0.059)

Table 3.6.: The goodness-of-fit results for fits to the control region data, using different values of the fixed number of $Z \rightarrow b\bar{b}$ events, and different functional forms for the QCD background model. The corresponding p-values are shown in parentheses.

Functional Form	No. Free Parameters	$\chi^2/\text{n}_{\text{d.o.f.}}$ (P-value)	Fitted $N^{\text{signal}}_{Z\rightarrow b\bar{b}}$	$\Delta N^{\text{signal}}_{Z\rightarrow b\bar{b}}$ w.r.t Baseline
Default	7	1.23 (0.018)	6418 ± 694	-
$\mathcal{F}_{\text{D}}$	7	1.29 (0.004)	6632 ± 772	+214 (+3.3%)

Table 3.7.: The results of the simultaneous fit using the default and an alternative functional form for the QCD background model.

is fixed to a range of different values between 5% and 300% of the Sherpa predicted value. The results of this test of the different functional forms are summarised in table 3.6. It is seen that using the default function and $\mathcal{F}_{\text{D}}$, the fit quality is stable as the number of $Z \rightarrow b\bar{b}$ events in the control region is varied, while for the other functions the fit quality degrades sharply.

Table 3.7 shows the results of the fit using the default QCD background function and the $\mathcal{F}_{\text{D}}$ function. The results are very consistent within statistical errors and so no systematic is assigned for the choice of the functional form of the QCD background.

3.4.5. Z Peak Position Results

The final column in Table 3.3 lists the size of the individual sources of uncertainty on the difference between the fitted and predicted values of the Z mass peak position, ΔM_Z. The uncertainty is dominated by the JES, which shifts the predicted value without having a significant effect on the fitted value. The resulting value is $\Delta M_Z =$ -1.5 ± 0.8 (stat.) ± 3.8 (sys.) GeV, which is consistent with the $Z \rightarrow b\bar{b}$ hypothesis.

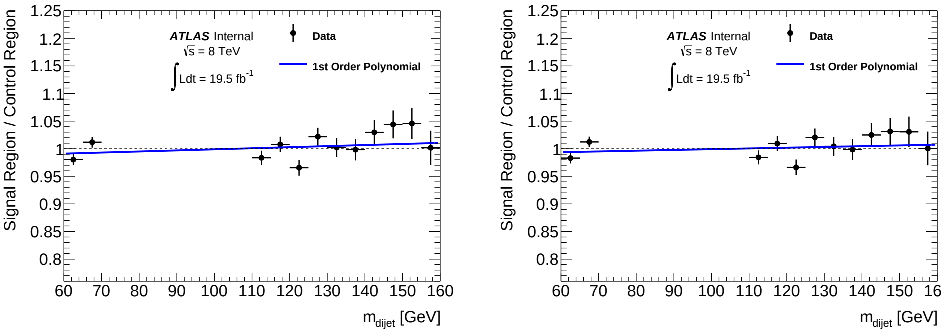

(a) Control Region $\mathcal{S}_{\mathcal{NN}} < 0.39$ (b) Control Region $\mathcal{S}_{\mathcal{NN}} < 0.40$

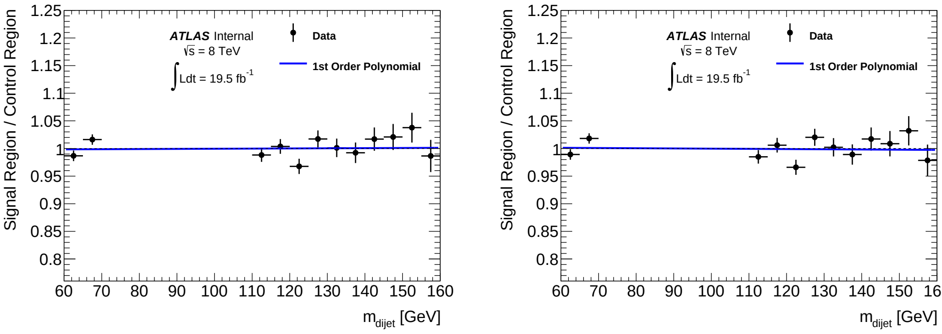

(c) Control Region $\mathcal{S}_{\mathcal{NN}} < 0.43$ (d) Control Region $\mathcal{S}_{\mathcal{NN}} < 0.44$

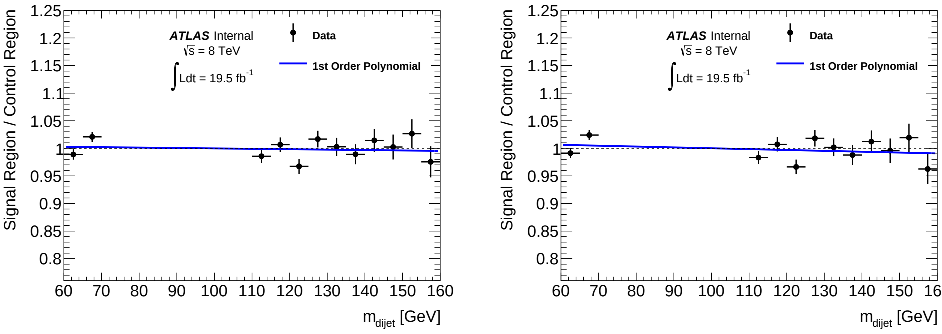

(e) Control Region $\mathcal{S}_{\mathcal{NN}} < 0.45$ (f) Control Region $\mathcal{S}_{\mathcal{NN}} < 0.47$

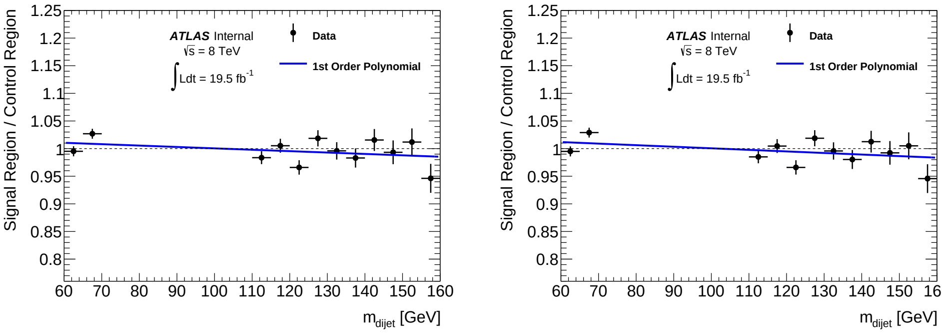

(g) Control Region $\mathcal{S}_{\mathcal{NN}} < 0.50$ (h) Control Region $\mathcal{S}_{\mathcal{NN}} < 0.51$

Figure 3.15.: Ratio of data in the signal region to the control region, for different values of the cut on $\mathcal{S}_{\mathcal{NN}}$, which defines the control region. The data within the Z mass window is excluded. A linear fit to the ratio is shown.

3.5. Acceptance Correction

A correction factor is needed to convert from the number of $Z \to b\bar{b}$ events measured in data to the fiducial cross section of the physical process defined in Section 3.1.1. This accounts for the fraction of events which meet the fiducial cross section definition but do not end up in the data measurement. For example, the b-tagging of jets containing B-hadrons is $\sim$ 70% efficient and so $\sim$ 50% of true $Z \to b\bar{b}$ events will not pass the double b-tagging requirement of the selection. This correction factor is referred to as the acceptance correction, $\mathcal{C}_{Z\to b\bar{b}}$, and is defined as:

$$\mathcal{C}_{Z\to b\bar{b}} = \frac{N^{\text{signal}}_{Z\to b\bar{b}}}{N^{\text{truth}}_{Z\to b\bar{b}}}, \tag{3.5}$$

where $N^{\text{truth}}_{Z\to b\bar{b}}$ is the number of events, according to MC, that satisfy the requirements on the truth particles that define the measured cross section. This acceptance correction can be factorised into individual components:

$$\mathcal{C}_{Z\to b\bar{b}} = \mathcal{C}^{b-\text{tag+kin}}_{Z\to b\bar{b}} \cdot \mathcal{C}^{\text{njets}}_{Z\to b\bar{b}} \cdot \mathcal{C}^{\mathcal{SNN}}_{Z\to b\bar{b}} \cdot \mathcal{C}^{\text{trig}}_{Z\to b\bar{b}}, \tag{3.6}$$

with:

$$\mathcal{C}^{b-\text{tag+kin}}_{Z\to b\bar{b}} = \frac{N^{b-\text{tag+kin}}_{Z\to b\bar{b}}}{N^{\text{truth}}_{Z\to b\bar{b}}} \quad \mathcal{C}^{\text{njets}}_{Z\to b\bar{b}} = \frac{N^{\text{njets}}_{Z\to b\bar{b}}}{N^{b-\text{tag+kin}}_{Z\to b\bar{b}}} \quad \mathcal{C}^{\mathcal{SNN}}_{Z\to b\bar{b}} = \frac{N^{\mathcal{SNN}}_{Z\to b\bar{b}}}{N^{\text{njets}}_{Z\to b\bar{b}}} \quad \mathcal{C}^{\text{trig}}_{Z\to b\bar{b}} = \frac{N^{\text{trig}}_{Z\to b\bar{b}}}{N^{\mathcal{SNN}}_{Z\to b\bar{b}}}, \tag{3.7}$$

where $N^{\text{b−tag+kin}}_{Z\to b\bar{b}}$ is the number of $Z \to b\bar{b}$ events after requiring a b-tagged dijet in the event; $N^{\text{njets}}_{Z\to b\bar{b}}$ is the number of $Z \to b\bar{b}$ events after also cutting on n_{jets} and n_{bjets}; $N^{\mathcal{SNN}}_{Z\to b\bar{b}}$ is the number of these events which are also in the signal region; and $N^{\text{trig}}_{Z\to b\bar{b}}$ is the number of $Z \to b\bar{b}$ events which pass all these cuts and are also selected by the triggers used.

Table 3.8 shows the values of the overall acceptance factor and the break-down into the individual components, for both the Pythia 8 and Sherpa $Z \to b\bar{b}$ MC. The

	Sherpa	Pythia 8	Pythia 8/Sherpa
$\mathcal{C}_{Z\to b\bar{b}}$	0.162	0.185	1.14
$\mathcal{C}_{Z\to b\bar{b}}^{\mathrm{b-tag+kin}}$	0.620	0.631	1.02
$\mathcal{C}_{Z\to b\bar{b}}^{\mathrm{njets}}$	0.850	0.865	1.02
$\mathcal{C}_{Z\to b\bar{b}}^{\mathcal{S}_{NN}}$	0.350	0.388	1.11
$\mathcal{C}_{Z\to b\bar{b}}^{\mathrm{trig}}$	0.881	0.872	0.99

Table 3.8.: The acceptance correction and its components for the two MC generators used to model $Z \to b\bar{b}$. The last column shows the fractional difference between the two predictions. The uncertainty on these numbers come from the number of events of the MC samples and are 0.000.

significant difference in the values of $\mathcal{C}_{Z\to b\bar{b}}$ is almost exclusively from the component relating to the $\mathcal{S}_{\mathcal{NN}}$ cut. Figure 3.16 shows the modelling of the ANN output variable and its two component variables by Pythia 8 and Sherpa, which show significant disagreement. Studies using $Z \to \mu\mu$ events in data, described in section 3.5.1 show that Sherpa models these variables well and so is the generator used to calculate the value of $\mathcal{C}_{Z\to b\bar{b}}$. The combined difference between the two generators for the other components of the acceptance is 2.5%.

3.5.1. Testing $Z \to b\bar{b}$ MC Modelling using $Z \to \mu\mu$ Events

Sherpa and Pythia 8 disagree on the modelling of the distributions of the input variables to the ANN used to define the signal and control regions. It is therefore important to evaluate which generator, if either, is modelling these variables accurately. This is done using $Z \to \mu\mu$ events in data, exploiting the fact that η of the b-tagged dijet is approximately equivalent to the η of the Z boson.

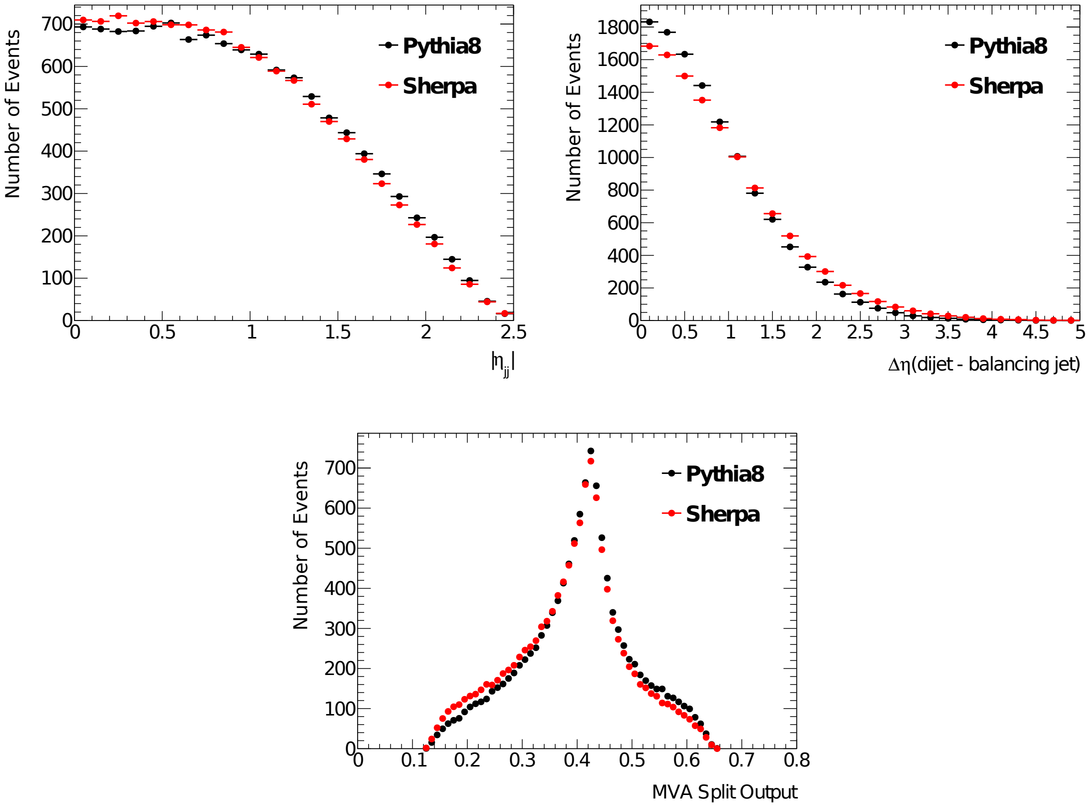

Figure 3.16.: The distributions, predicted by the two different MC generators, of selected $Z \to b\bar{b}$ events, of the two variables used to form the ANN: (a) the absolute $|\eta|$ position of the b-tagged dijet; (b) the difference in η of the b-tagged dijet and the balancing jet in the event. (c) The ANN output.

A sample with a high purity of $Z \to \mu\mu$ events is extracted from the data using the following criteria to select events:

- Pass a trigger which selects events containing at least one isolated muon with $p_{\mathrm{T}} > 24$ GeV.
- Contain at least 2 reconstructed muons which meet the requirements:
  - Isolation using ID tracks: (sum of p_{T} of tracks) / (p_{T} of muon candidate) < 0.04 within cone of ΔR=0.2 around muon candidate.
  - Isolation using calorimeter information: (sum E_T) / (E_T of muon candidate) < 0.07 within cone of ΔR=0.3 around muon candidate.
  - Muon-jet overlap removal: reject muon candidate if within $\Delta R < 0.4$ of a jet with $p_{\mathrm{T}} > 20$ GeV.
  - $p_{\mathrm{T}} > 25$ GeV.
  - $|\eta| < 2.5$.
- At least 1 dimuon, formed by adding the 4-vectors of a pair of muons, which satisfies:
  - Invariant mass consistent with a Z decay: $75 < M_{\mu^-\mu^+} < 105$ GeV.
  - $p_T^{\mu^-\mu^+} > 150$ GeV.
- At least one jet in the event with $p_{\mathrm{T}} > 20$ GeV and $|\eta| < 2.5$.

Applying this selection to data results in 27075 selected events. Figure 3.17 shows the distributions of variables that are analogous to the ANN variables. Sherpa $Z \to \mu\mu$ MC models the data well in both variables and the ANN output, $\mathcal{S_{NN}}$. The modelling is also found to be good when the p_{T} cut on the dimuon system is increased from 150 to 200 and 250 GeV. Based on this Sherpa is chosen to model the acceptance. Sherpa is expected to model these event variables more accurately, since they are sensitive to extra hard radiation in the event, which is calculated in the matrix element in Sherpa, whereas for Pythia 8 it is handled purely by the parton shower.

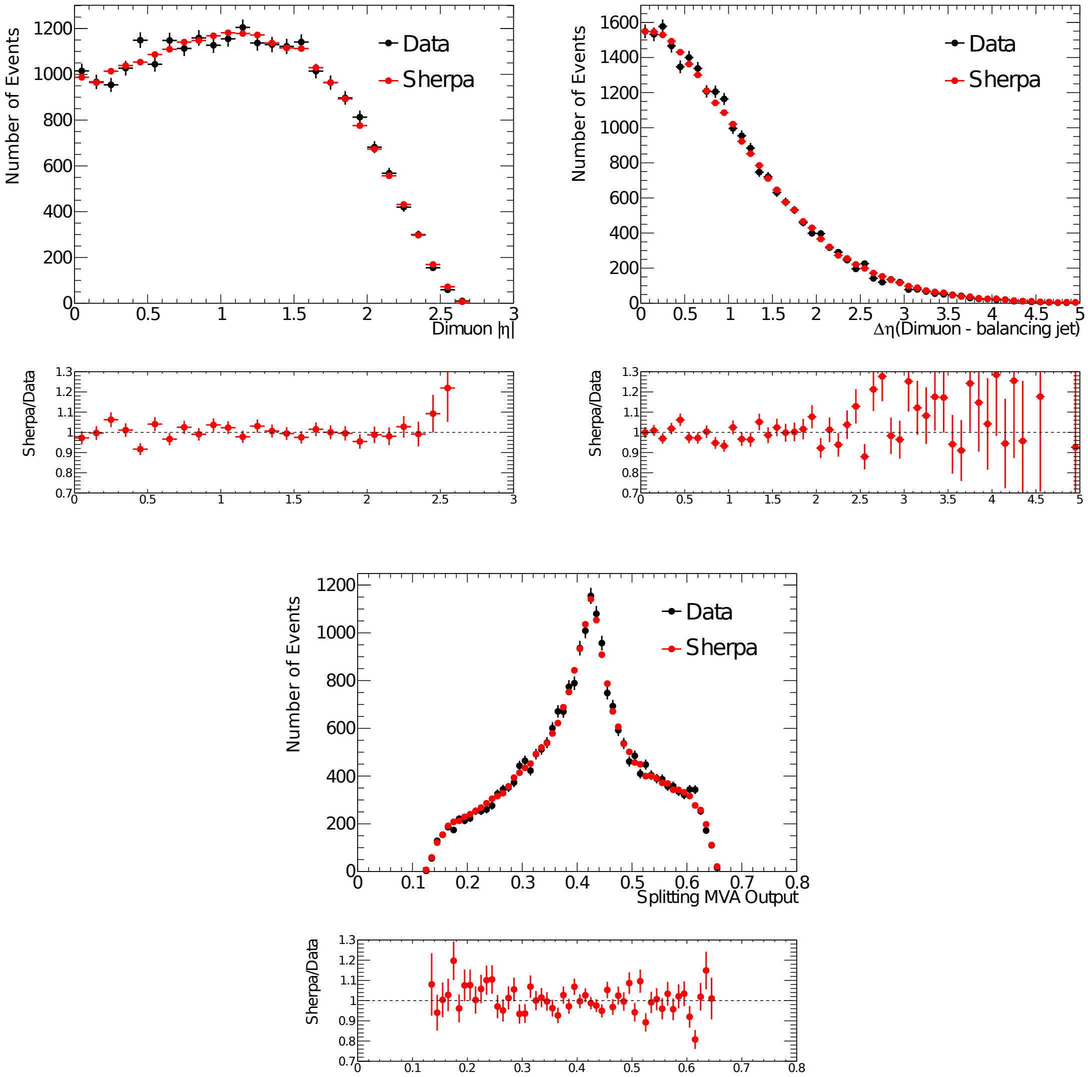

Figure 3.17.: The distribution of (a) the $|\eta|$ of the dimuon system; (b) the difference in η between the muon and balancing jet in the event; (c) the output of the ANN. Data and Sherpa $Z \to \mu\mu$ MC events that pass the $Z \to \mu\mu$ selection criteria are compared. The MC is normalised to the same number of events as observed in the data.

3.5.2. Systematic Uncertainties on the Acceptance

Table 3.9 gives a summary of the systematic uncertainties on the acceptance correction, $\mathcal{C}_{Z\to b\bar{b}}$, from the various different sources that have been considered. The uncertainties from the jet energy scale and b-tagging efficiency are calculated by applying the ±1σ eigenvector variations (see Sections 2.6.2, 2.7.1) to the Sherpa

Systematic Source	$\Delta\mathcal{C}_{Z\to b\bar{b}}$	$\Delta\mathcal{C}_{Z\to b\bar{b}}$ (%)
JES Up	+0.013	+8.3
JES Down	-0.014	-8.5
JER	±0.0003	±0.2
b-Tag Efficiency Up	+0.006	+3.6
b-Tag Efficiency Down	-0.006	-3.7
Signal $\mathcal{S}_{\mathcal{NN}}$ Modelling	±0.0032	±2.0
Trigger Modelling	±0.010	±6.0

Table 3.9.: The individual sources of systematic uncertainty on the acceptance correction, $\mathcal{C}_{Z\to b\bar{b}}$.

$Z \to b\bar{b}$ MC and recalculating the acceptance. The uncertainty from the JER (see Section 2.6.2) is obtained by applying the $+1\sigma$ smearing, recalculating the acceptance and symmetrising the resulting uncertainty.

One source of uncertainty is the accuracy of the MC modelling of the kinematics of the $Z \to b\bar{b}$ events. Table 3.8 shows the factorised acceptance values for two different MC generators; SHERPA and PYTHIA 8. It is seen that the only significant difference between the two is in the factor coming from the modelling of $\mathcal{S}_{\mathcal{NN}}$, which is constrained by the comparison of SHERPA to data in $Z \to \mu\mu$ + jet events. The differences between the other factors of the acceptance between SHERPA and PYTHIA 8 are small enough to be neglected. Table 3.10 shows the acceptance values of the signal region $\mathcal{S}_{\mathcal{NN}}$ cut, using the analogous input variables to the ANN in $Z \to \mu\mu$ + jet events, comparing data to MC. This is done for 3 different values of the cut on dimuon p_{T}, since there is no one-to-one equivalence for dimuon and dijet p_{T}. The largest difference between data and SHERPA is 1.5%, this is rounded to a ±2% uncertainty on the acceptance.

Uncertainty on Trigger Efficiency

Another source of uncertainty on the acceptance comes from the uncertainty on the simulated value of the trigger efficiency for $Z \to b\bar{b}$ events. The accuracy of this modelling is assessed by using a subset of data which passed a trigger which is highly

Dimuon p_{T} cut	Data $\mathcal{C}^{\mathcal{S}_{NN}}_{Z\to\mu\mu}$	SHERPA $\mathcal{C}^{\mathcal{S}_{NN}}_{Z\to\mu\mu}$	$\Delta\mathcal{C}^{\mathcal{S}_{NN}}_{Z\to\mu\mu}$ (Data-SHERPA) (%)
$p_{\mathrm{T}} > 150$ GeV	0.438 ± 0.003	0.433 ± 0.001	+1.0
$p_{\mathrm{T}} > 200$ GeV	0.418 ± 0.006	0.412 ± 0.002	+1.5
$p_{\mathrm{T}} > 250$ GeV	0.388 ± 0.009	0.390 ± 0.003	-0.6

Table 3.10.: The acceptance factor from the signal region selection, $\mathcal{C}^{\mathcal{S}_{NN}}_{Z\to\mu\mu}$, in $Z \to \mu\mu +$ jet events, for different values of the cut on dimuon p_{T}.

efficient for the signal but is prescaled, meaning that a small fixed fraction of events which pass the trigger are recorded. The prescaled trigger requires at least one anti-k_t R = 0.4, jet in the event with $p_{\mathrm{T}} > 145$ GeV and so is henceforth referred to as the 'j145' trigger. The predicted efficiency in simulated QCD events is compared to that in the data. Since there is a difference in the kinematics between QCD events and $Z \to b\bar{b}$ events, this is investigated as a function of various kinematic variables. Since the flavour composition of QCD events is different to that of the pure bb of the $Z \to b\bar{b}$ events, the effect of making a pure bb flavour requirement on the QCD MC is also investigated.

Figure 3.18 compares the kinematics of the PYTHIA 8 QCD MC to the data in several variables, for events which pass the prescaled trigger and the analysis preselection cuts. Reasonable agreement is observed.

The j145 trigger has a predicted efficiency for selected signal events, using SHERPA $Z \to b\bar{b}$ MC, of 96.4%. This efficiency is shown, in Figure 3.19, as a function of the p_{T} of the b-tagged dijet. The relative efficiency used to compare data to MC is defined as:

$$\frac{N_{pass}(\text{j145 AND Analysis Trigger Selection})}{N_{pass}(\text{j145})}, \tag{3.8}$$

where N_{pass} is the number of events passing the respective triggers, and the 'Analysis Trigger Selection' is the OR of the 6 triggers used in the analysis. The overall values of this efficiency are listed in Table 3.11. Figures 3.20 and 3.21 show the efficiency as a function of various kinematic variables. The large uncertainties on the QCD MC efficiency are due to limited statistics in the available samples after applying the

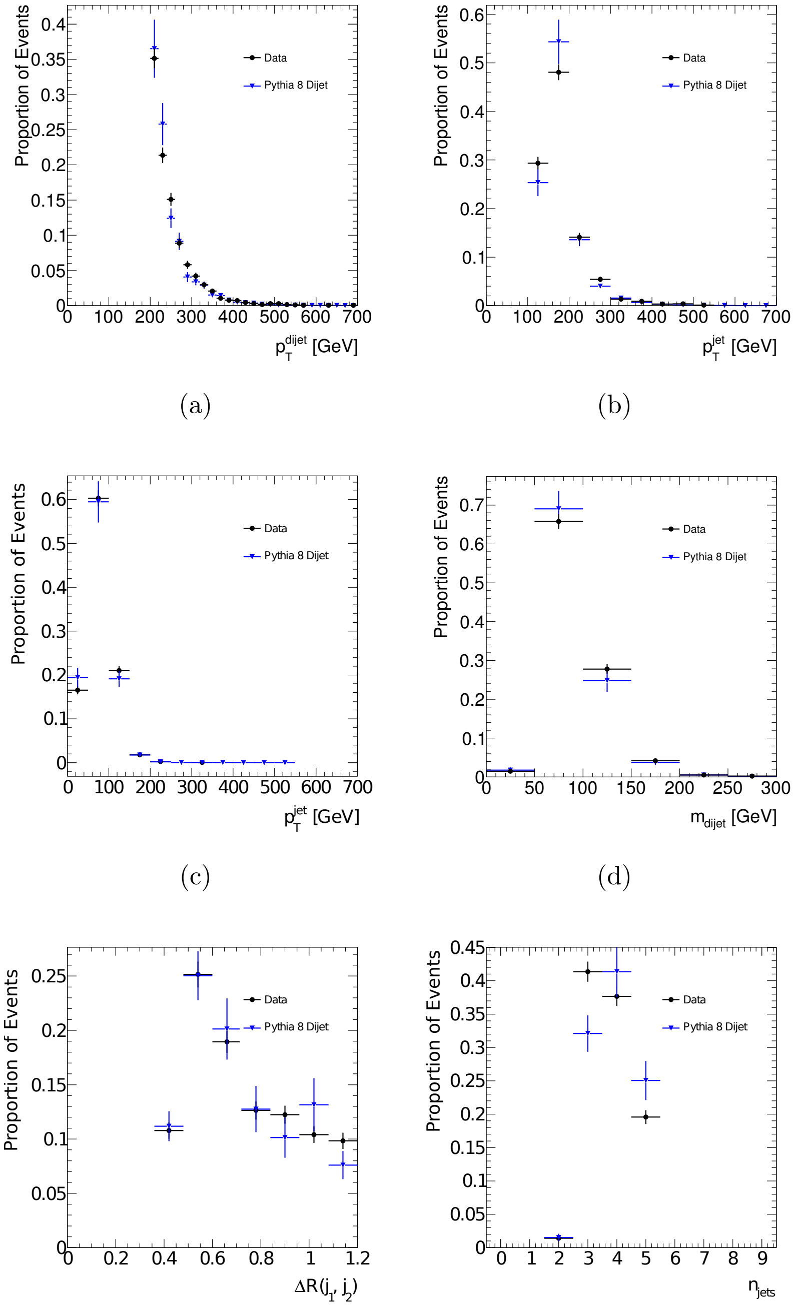

(a) (b)

(c) (d)

(e) (f)

Figure 3.18.: Plots comparing the kinematics of QCD MC to data for events that pass the j145 trigger and the analysis preselection. The histograms are normalised to unit area. The comparison is shown as a function of (a) the p_T of the b-tagged dijet, (b) the p_T of the higher p_T jet of that dijet, (c) the p_T of the lower p_T jet of that dijet, (d) the invariant mass of that dijet, (e) the angular separation between the two jets in the dijet, (f) the number of jets in the event.

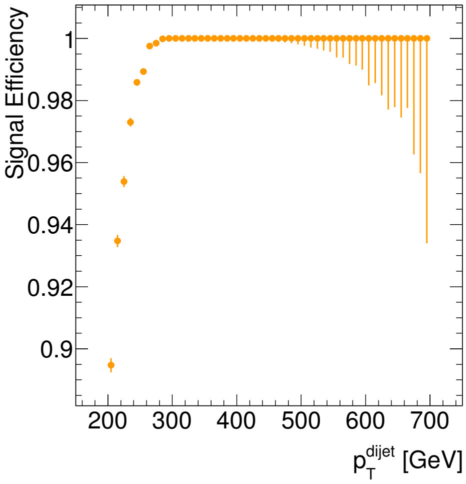

Figure 3.19.: The efficiency for selected signal events of the j145 trigger as a function of the p_{T} of the b-tagged dijet

	Data	QCD MC	QCD MC, truth bb matched
Trigger Efficiency	78 ± 1 %	83 ± 2 %	86 ± 2 %

Table 3.11.: The trigger efficiencies of events that pass the preselection in data and Pythia 8 QCD MC. These efficiencies are calculated using events that pass the prescaled j145 trigger.

event selection. The 'Truth bb Matched' QCD MC points are calculated using only events where both jets in the dijet are matched to a B-hadron. The overall trigger efficiency is observed to be higher in the QCD MC than in the data.

These comparisons are repeated, with the Pythia 8 QCD MC and the data reweighted to the Sherpa signal MC kinematics. This is in order to both remove the effect, on the MC efficiency, of possible kinematic mis-modelling of the data by the MC and also to test the agreement between data and MC in the kinematic distribution of the signal. This is done by reweighting on 3 variables: the p_{T} of the two jets in the dijet and the p_{T} of the balancing jet in the event. The events are reweighted by first taking the product of the weights from the three individual distributions and then recalculating the distributions after this initial reweighting and obtaining another multiplicative weight from these distributions, the events are then reweighted with this improved weight and the distributions are recalculated

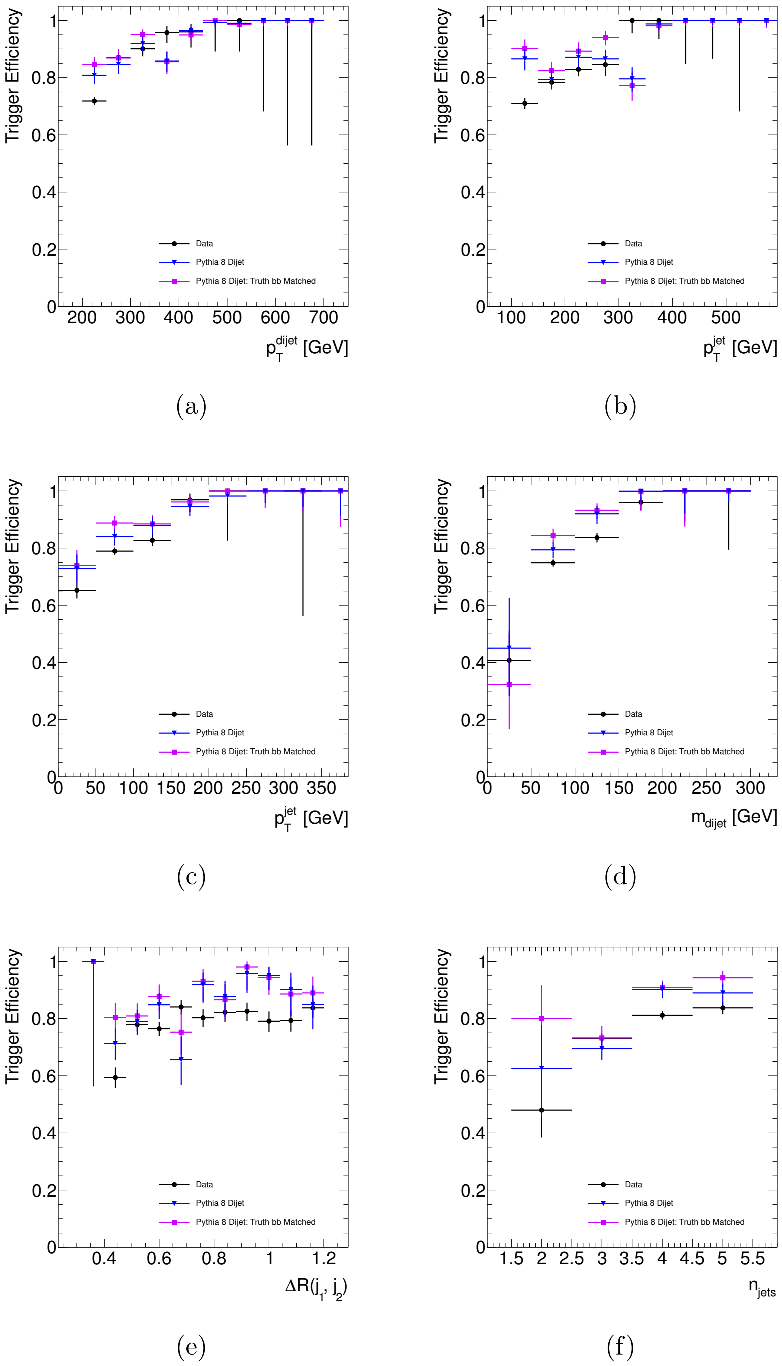

(a) (b)

(c) (d)

(e) (f)

Figure 3.20.: Plots of the trigger efficiency for events passing the preselection, calculated using events that pass the prescaled j145 trigger. The efficiency is shown as a function of (a) the p_T of the b-tagged dijet, (b) the p_T of the higher p_T jet of that dijet, (c) the p_T of the lower p_T jet of that dijet, (d) the invariant mass of that dijet, (e) the angular separation between the two jets in the dijet, (f) the number of jets in the event.

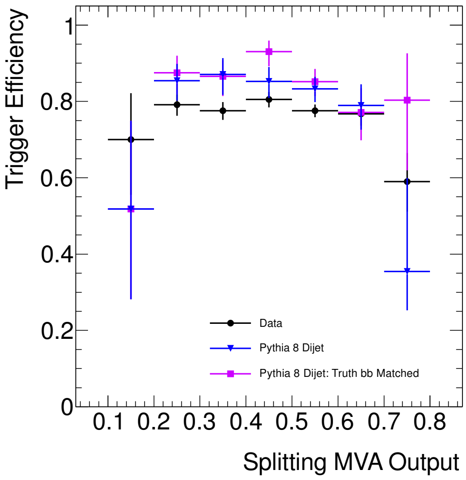

Figure 3.21.: A plot of the trigger efficiency for events passing the preselection, calculated using events that pass the prescaled j145 trigger. The efficiency is shown as a function of the ANN output, $\mathcal{S}_{\mathcal{N}\mathcal{N}}$.

again. This procedure is iterated 25 times and appears to do a good job of accounting for the correlations between the three variables in this case. Figures 3.22 show a comparison of the kinematics between the SHERPA signal MC, PYTHIA 8 QCD MC and data, for events passing the preselection and the j145 trigger, after this reweighting.

Figures 3.23 show comparisons between the trigger efficiency of selected signal MC, QCD MC and data events, after reweighting the QCD MC and data, as a function of different kinematic variables. Table 3.12 shows the overall trigger efficiency after this reweighting. The value for truth bb matched dijet MC is in good agreement with the value of 89% for the efficiency, relative to the j145 trigger, of the signal MC. This shows that the reweighting has covered the kinematics that are most relevant to the trigger efficiency. The value assigned for this systematic uncertainty is taken as the difference in the overall trigger efficiency between the reweighted data and QCD MC, which is 5% absolute, 6% relative.

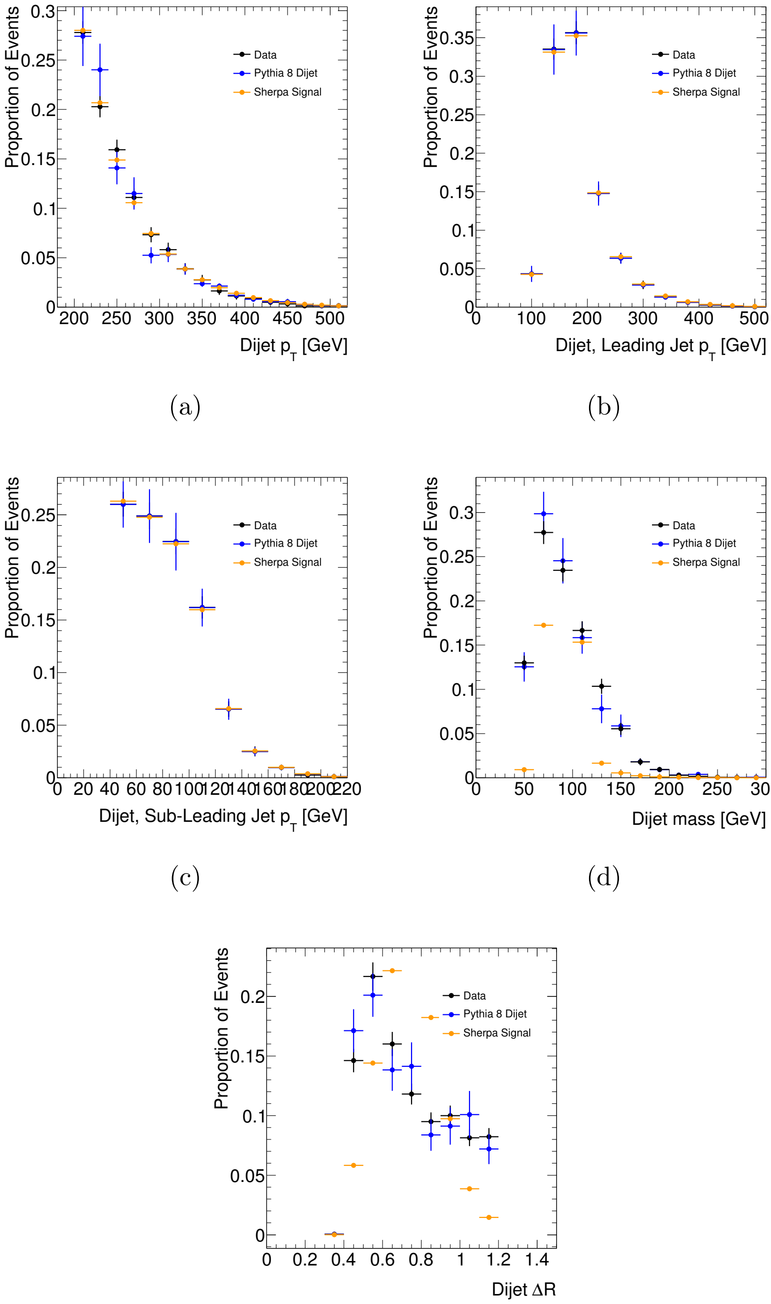

(a)

(b)

(c)

(d)

(e)

Figure 3.22.: Plots comparing the kinematics of QCD MC to data for events that pass the j145 trigger and the analysis preselection. The data and QCD MC have been reweighted to the p_{T} distributions of the Sherpa signal MC. The histograms are normalised to unit area. The comparison is shown as a function of (a) the p_{T} of the b-tagged dijet, (b) the p_{T} of the higher p_{T} jet of that dijet, (c) the p_{T} of the lower p_{T} jet of that dijet, (d) the invariant mass of that dijet, (e) the angular separation between the two jets in the dijet.

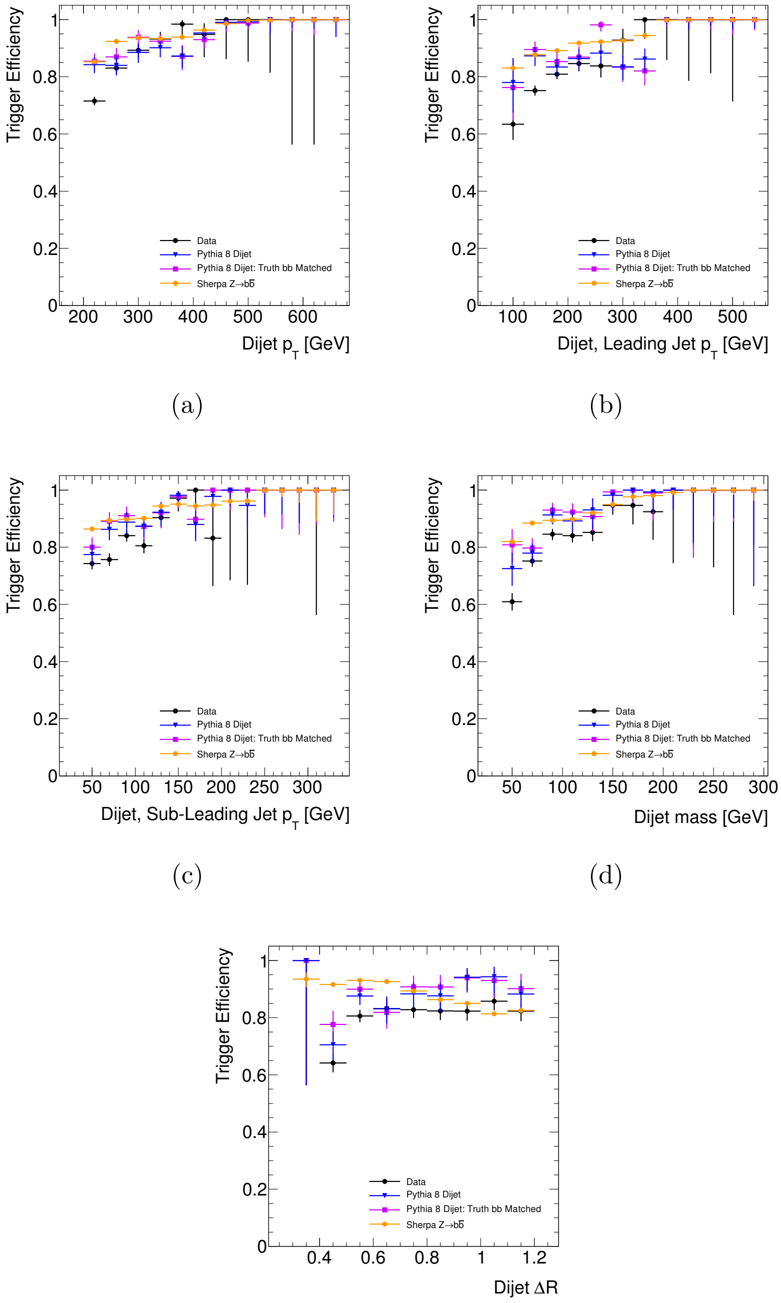

(a)

(b)

(c)

(d)

(e)

Figure 3.23.: Plots of the trigger efficiency for events passing the preselection, calculated using events that pass the prescaled j145 trigger. The data and QCD MC have been reweighted to the p_{T} distributions of the Sherpa signal MC. The efficiency is shown as a function of (a) the p_{T} of the b-tagged dijet, (b) the p_{T} of the higher p_{T} jet of that dijet, (c) the p_{T} of the lower p_{T} jet of that dijet, (d) the invariant mass of that dijet, (e) the angular separation between the two jets in the dijet.

	Data	QCD MC	QCD MC, truth bb matched
Trigger Efficiency	80 ± 1 %	85 ± 2 %	89 ± 2 %

Table 3.12.: The trigger efficiencies of events that pass the preselection in data and MC. The data and Pythia 8 QCD MC have been reweighted to the p_T distributions of the Sherpa signal MC. These efficiencies are calculated using events that pass the prescaled j145 trigger.

3.6. Results and Theoretical Predictions

The resulting fiducial cross section, calculated using the number of observed $Z \to b\bar{b}$ events, the acceptance and the luminosity, with Equation 3.1, is:

$$\boldsymbol{\sigma_{Z\to b\bar{b}} = 2.02 \pm 0.20\ (\textbf{stat.})\ \pm 0.25\ (\textbf{syst.}) \pm 0.06\ (\textbf{lumi.}) = 2.02\ \pm 0.33\ \textbf{pb}}$$

$$\boldsymbol{= 2.02 \pm 10.0\%\ (\textbf{stat.})\ \pm 12.4\%\ (\textbf{syst.}) \pm 2.8\%\ (\textbf{lumi.}) = 2.02\ \textbf{pb}\ \pm 16.3\%},$$

where the statistical uncertainty comes from the fitted value of $N^{\mathrm{signal}}_{Z\to b\bar{b}}$, the luminosity uncertainty comes from the 2.8% uncertainty on the measured value of the integrated luminosity and the systematic uncertainty is the combination of those on $N^{\mathrm{signal}}_{Z\to b\bar{b}}$ and the acceptance, summarised in Table 3.13.

Two different NLO plus parton shower MC predictions are generated to compare to the measured cross section. One using POWHEG [62] and one using aMC@NLO [63]. For both of these generators, the Z + 1 jet process is calculated at NLO for the matrix element. For aMC@NLO, the Z decay is simulated with MadSpin [64]. POWHEG is interfaced to Pythia 8 for the parton showering, hadronisation and underlying event stages of the simulation, whilst aMC@NLO is interfaced to Herwig++ [22]. The predicted values are obtained by applying the particle level selection described in Section 3.1.1 to the simulated events. The predicted cross sections are:

POWHEG + Pythia 8: $\sigma_{Z\to b\bar{b}} = 2.02^{+0.25}_{-0.19}$ (scales) ${}^{+0.03}_{-0.04}$ (PDF) pb,

aMC@NLO + Herwig++: $\sigma_{Z\to b\bar{b}} = 1.98^{+0.16}_{-0.08}$ (scales) ±0.03 (PDF) pb.

Systematic Source	$\Delta N^{\text{signal}}_{Z\to b\bar{b}}$ (%)	$\Delta \mathcal{C}_{Z\to b\bar{b}}$ (%)	$\Delta \sigma_{Z\to b\bar{b}}$ (%)
JES	+3.0/-1.5	±8.4	+6.5/-5.0
JER	±5.3	±0.2	±5.1
b-Tag Efficiency	±0.1	±3.6	±3.6
Signal m_{dijet} Shape	±2.2	N/A	±2.2
Signal $\mathcal{S}_{\mathcal{NN}}$ Modelling	±0.9	∓2.0	±2.9
$Z \to c\bar{c}$ Normalisation	±0.4	N/A	±0.4
$t\bar{t}$ Normalisation	±1.2	N/A	±1.1
$W \to \bar{q}q'$ Normalisation	±1.0	N/A	±1.0
Control Region Bias	±5.2	N/A	±5.2
Trigger Mismodelling	N/A	±6	±6

Table 3.13.: The relative systematic uncertainties on the fitted number of $Z \to b\bar{b}$ events, the acceptance and the measured fiducial cross section from each of the systematic sources considered.

Both generators use the CT10 [65] PDF for the central value of the prediction. The uncertainties from the PDF are evaluated by running over the 52 eigenvector PDFs and adding in quadrature the maximum deviation of each of the pairs of variations and then applying a scaling factor to go from 90% CL to 68% CL. This uncertainty is found to be 1-2%. The factorisation and renormalisation scales for both POWHEG and aMC@NLO are the p_{T} of the Z boson. These scales are varied simultaneously by a factor of 2.0 and 0.5 in order to evaluate the uncertainty in the prediction coming from the choice of these scale values. These scale uncertainties are ~4-12% and thus completely dominate the overall uncertainty. Both predictions are consistent with the measured cross section to within the uncertainties on the measurement and theory.

Predictions are also made using two alternative NLO PDF sets; MSTW2008 [66] and NNPDF2.3 [67]. The uncertainty on MSTW is evaluated with the same method as with CTEQ but without the scaling from 90% CL needing to be applied since the eigenvectors are produced at 68% CL. For NNPDF the uncertainty is the standard deviation of the 100 replica PDFs.

$$\text{POWHEG + PYTHIA 8, CTEQ10:} \qquad \sigma_{Z\to b\bar{b}} = 2.02^{+0.03}_{-0.04}\ \text{(PDF) pb}$$

POWHEG + Pythia 8, MSTW2008: $\sigma_{Z\to b\bar{b}} = 2.11 \pm 0.02$ (PDF) pb

POWHEG + Pythia 8, NNPDF 2.3: $\sigma_{Z\to b\bar{b}} = 2.07 \pm 0.01$ (PDF) pb

aMC@NLO + Herwig++, CTEQ10: $\sigma_{Z\to b\bar{b}} = 1.98 \pm 0.03$ (PDF) pb

aMC@NLO + Herwig++, MSTW2008: $\sigma_{Z\to b\bar{b}} = 2.10 \pm 0.02$ (PDF) pb

In order to compare the measured cross section to the parton level generator MCFM, a correction, from the parton level cross section defined by Z boson $p_T > 200$ GeV, to our fiducial cross section, is derived, which is refered to as A. The values of this using the two different NLO+PS generators, with the CT10 PDF are:

POWHEG + Pythia 8: $A = 0.53$

aMC@NLO + Herwig++: $A = 0.47$

Figure 3.24 shows the value of this correction as a function of the Z boson p_{T}, where the Z boson is the one in the event record before any parton shower or underlying event. It can be seen that there is a turn on at lower values of the Z p_{T}, due to the particle level dijet p_{T} cut and then a downwards slope above 400 GeV where the b quarks from the Z decay are starting to merge into a single anti-k_t 0.4 jet.

The MCFM [49] prediction for $Z \to b\bar{b}$, with Z boson $p_T > 200$ GeV, using factorisation and renormalisation scales of $\sqrt{M^2(Z) + p_T^2(Z)}$ and the CT10 PDF is $4.29^{+0.40}_{-0.36}$ pb, where the uncertainty comes from varying the scales by a factor of 0.5/2.0. Using the mean of the two values of A and taking the difference from the individual values to the average as the uncertainty, the corrected MCFM prediction is

MCFM x A: $\sigma_{Z\to b\bar{b}} = 2.14^{+0.20}_{-0.18}$ (scales) ± 0.13 (parton level correction) pb,

which is again in good agreement with the measured value.

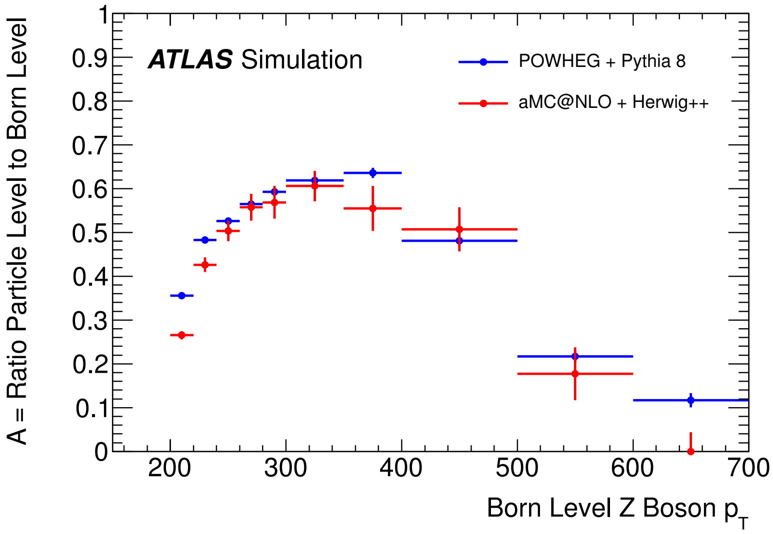

Figure 3.24.: The ratio of $Z \to b\bar{b}$ events passing the fiducial cross section definition to those passing the parton level cut of $p_T(Z) > 200$ GeV as a function of the p_{T} of the Z.

3.7. Cross-Checks and Additional Studies

Several cross checks are made in order to test the robustness of the measurement. These involve repeating the measurement with some variation of the analysis event selection which alters the background m_{dijet} shape substantially. The results of these are summarised in Table 3.14 and the fits in the signal region are shown in Figures 3.25.

The first cross check is to raise the p_{T} cut on the b-tagged dijet to 250 and 300 GeV. The second is to tighten the b-tagging from the 70% efficiency working point to the 60% efficiency working point. The last is to split the data up into two subsets based on the triggers that they passed. Subset 1 is all events which passed the most efficient of the 6 triggers used, which is EF_2b35_loose_j145_j35_a4tchad as described in Section 2.3. Subset 2 is events which did not pass that trigger but did pass at least one of the other 5 triggers. Each check results in a consistent value of the measured cross section.

Variation	Yield	Acceptance	Cross Section [pb]
Baseline	6418 ± 641	0.162	2.02 ± 0.20
Dijet $p_{\mathrm{T}} > 250$ GeV	2784 ± 370	0.067	2.11 ± 0.28
Dijet $p_{\mathrm{T}} > 300$ GeV	830 ± 201	0.027	1.58 ± 0.38
MV1 60% Working Point	4721±537	0.119	1.98±0.22
Trigger subset 1	5057±570	0.117	2.17±0.24
Trigger subset 2	1654±398	0.045	1.87±0.44

Table 3.14.: The results from various different cross-checks, where the event selection has been modified in the specified way. The errors shown are only the statistical errors from the fit. The cross sections are all using the same fiducial definition for direct comparison.

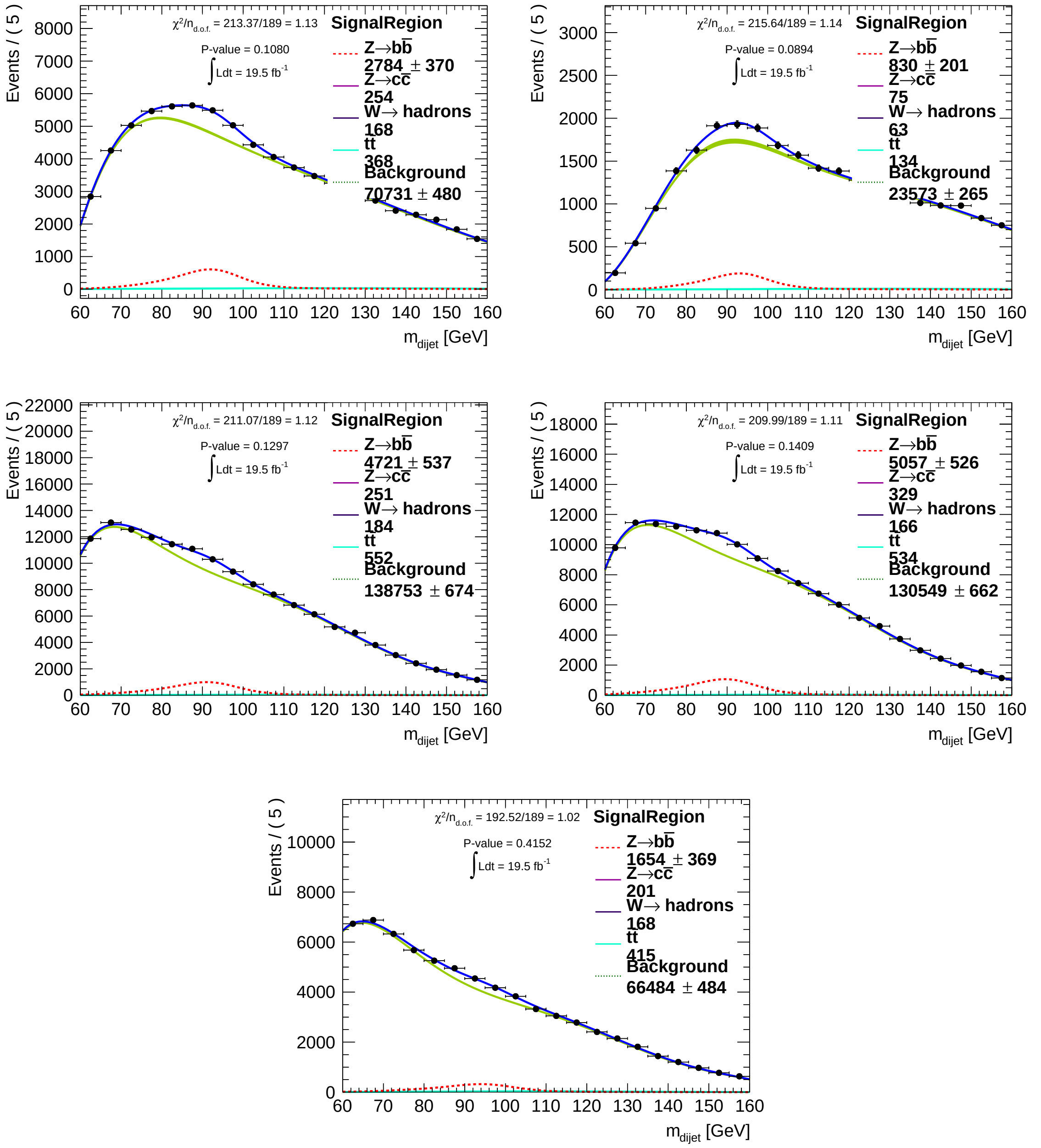

Figure 3.25.: The signal region m_{dijet} distribution with the simultaneous fit results for the different cross check variations of the event selection. (a)/(b) dijet p_{T} cut increased to 250/300 GeV, (c) lower efficiency/higher purity b-tagging point used, (d)/(e) two subsets of the data which passed different triggers.

Chapter 4.

Search for $X \to HH/ZZ \to b\bar{b}b\bar{b}$

4.1. Introduction

The studies on simulated events described in Section 4.2, below, show that the decay channel $HH \to b\bar{b}b\bar{b}$ has sensitivity down to very low cross sections for any resonance with a mass $>$ 500 GeV decaying to HH. The rest of this chapter describes the search performed in this channel using the pp data collected with the ATLAS detector in 2012 at a centre of mass energy of 8 TeV.

4.2. Initial Sensitivity Study

Introduction

The discovery of the Higgs boson at ~125 GeV [10,11] has opened up new possibilities for searches for BSM processes involving Higgs bosons. One example of this is a search for a new, heavy particle decaying to two Higgs bosons. With a predicted branching ratio of 58%, the most common decay of the SM Higgs is to $b\bar{b}$ [68]. For high masses of such a resonance, the two Higgs bosons will be given a substantial boost in p_{T}, resulting in two high-p_{T} $b\bar{b}$ dijets. This signal topology has several important advantages: firstly, the QCD backgrounds will be substantially reduced by requiring two high-p_{T} sets of close-by b-tagged jets; secondly, there is no ambiguity in which b-jets are paired together to form the two Higgs candidates; lastly, the high

p_{T} of the jets will allow for efficient selection at the level 1, hardware based triggers of ATLAS and CMS.

There is an implicit assumption in this search channel that the observed Higgs boson decays with a significant branching ratio to $b\bar{b}$, as the Standard Model predicts, despite the fact that at the time of writing this has not been experimentally verified. However, the current measurements of the properties of the 125 GeV Higgs have all been consistent with the SM predictions [69–71]. In particular, the recent observation of the $H \to \tau\tau$ [72] decay, confirms that the Higgs couples to at least one of the fermions. So the assumption that the Higgs decays to $b\bar{b}$ is a reasonable one. Since the branching ratio $H \to b\bar{b}$ is not measured, all search significances and exclusion limits are quoted in terms of $\sigma(X \to HH \to b\bar{b}b\bar{b})$ rather than $\sigma(X \to HH)$, where X is the heavy BSM particle.

There are a number of different theory models which predict such a heavy resonance. Most notable amongst these are 2-Higgs-doublet models (2HDM), where the lighter CP-even Higgs is the 125 GeV particle and the heaver CP-even Higgs can decay via $H \to hh$ [73]. Another model, described in [74], predicts a Randall-Sundrum bulk graviton excitation, which generally decays with a significant branching ratio to two SM Higgs bosons.

This section contains studies using MC events in order to obtain an estimate of the sensitivity of a search using ATLAS or CMS for a heavy resonance, X, decaying via $X \to HH \to b\bar{b}b\bar{b}$.

Signal and Background Models

The benchmark signal model used in these studies is a Randall-Sundrum bulk graviton excitation (G^*) described in Section 1.1.2. The signal is simulated using MadGraph [64] based on the scenario proposed in [15, 74] with $k/\bar{M}_{\mathrm{Pl}} = 1$, where k is the curvature scale of the extra dimension and $\bar{M}_{\mathrm{Pl}}$ is the reduced Planck mass. The CTEQ6L1 PDFs [75] are used and MadGraph is interfaced to Pythia 8.170 [23] for parton showering and to simulate hadronisation and underlying event.

The dominant backgrounds for this search are QCD multijet events, with real b-jets and also mis-tagged c and light jets, and $t\bar{t}$. The backgrounds from Z+jets and diboson events are found to be small enough to neglect for the purposes of this sensitivity study.

SHERPA 1.4.3 [24] is used to model the QCD multi-jet processes. Studies using Pythia to generate all $2 \to 2$ QCD processes, indicate that, after b-tagging, the QCD is dominated by $b\bar{b}b\bar{b}$ events with the next largest contribution from $b\bar{b}c\bar{c}$ events according to the flavour of the selected four jets. These are the two classes of QCD multijet events that are simulated with SHERPA, in terms of the $2 \to 4$ matrix elements. Other QCD multijet contributions are ignored. The uncertainty on the generated cross section is determined by varying the renormalisation and factorisation scales by factors of 1/2 and 2 from the nominal values of $\frac{1}{4}\sqrt{\sum_i p_{T,i}^2}$. It is found in [76] that, with the same choice of scales, this variation covers the NLO prediction.

The $t\bar{t}$ contribution is simulated using Pythia 8.170, with the cross section scaled to the average cross section measured by ATLAS and CMS at 8 TeV [77, 78]. The flavour composition of the jets passing the selection, in these simulated $t\bar{t}$ events, is found to be predominantly $bc - bc$, coming from the hadronic decays of both tops; $t \to bW \to bcs$. The uncertainty on the measured cross section is used as the uncertainty on the normalisation of the $t\bar{t}$ background model.

Event Selection

Jets are constructed out of stable final state particles in the event, excluding muons and neutrinos, using the anti-k_t algorithm [35] with radius parameter $R = 0.4$. A simple event selection is applied, which consists of requiring at least 2 independent dijets to be formed out of b-tagged jets with $p_{\mathrm{T}} > 40$ GeV and $|\eta| < 2.5$, where the jets in the dijets have $\Delta R(\mathrm{jet1}, \mathrm{jet2}) < 1.2$, $p_T^{dijet} > 200$ GeV and $100 < M^{\mathrm{dijet}} < 130$ GeV. These cuts have not been optimised.

The b-tagging is simulated by assigning weights to jets according to their flavour, where the weights are the approximate tagging/mis-tagging efficiency of the typical b-tagging algorithms used in ATLAS and CMS [79,80]. If a jet has a B-hadron within $\Delta R < 0.3$ of it's centre, it is labeled a b-jet and given a weight of 0.7, if a jet is not labeled a b-jet but has a charm hadron within $\Delta R < 0.3$ then it is labeled a c-jet and given a weight of 0.2 and if a jet is neither a b-jet or c-jet it is labeled a light-jet and given a weight of 0.01.

The efficiency of this selection as a function of the mass of the RS graviton is shown in Figure 4.1. At low signal masses the efficiency is reduced due to the dijet p_{T} cut. At high signal masses, efficiency is lost due to the two b-quarks merging into a single anti-k_t, $R = 0.4$, jet.

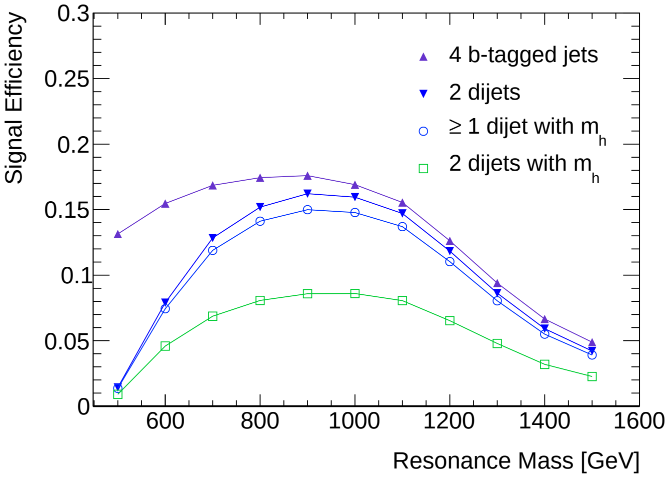

Figure 4.1.: The signal efficiency as a function of the mass of the RS graviton, for each subsequent selection requirement.

The distribution of the combined invariant mass of the 4 b-tagged jets, m_{4b}, is used to search for the resonance. In real experimental data, the m_{4b} of the signal would be smeared out by the resolution of the detector, however the width of the RS graviton resonance is already $\sim 5\%$ of its mass and it would also be possible to use the known mass of the Higgs to fit the kinematics in order to improve the experimental resolution of the peak and so detector resolution is ignored in this sensitivity study.

Requirement	G^* ($\mathrm{m}_{\mathrm{G}^*} = 800\,\mathrm{GeV}$)	QCD	$t\bar{t}$
4 b-tagged jets	13.2	19700	3590
2 dijets	11.4	414	151
$\geq$ 1 dijet with m_H	10.7	183	89
2 dijets with m_H	6.1	28^{+20}_{-11}	21 ± 3

Table 4.1.: The expected signal and background yields for $\int \mathcal{L}dt = 20\ \mathrm{fb}^{-1}$ at $\sqrt{s} = 8\,\mathrm{TeV}$ at each stage of the event selection.

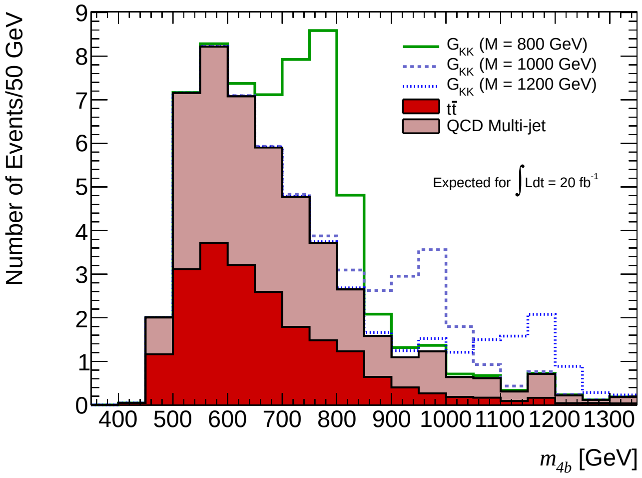

Figure 4.2.: The m_{4b} distribution for various RS graviton masses and for the background. The signal is normalised to the number of events needed for 3σ evidence in $20\,\text{fb}^{-1}$ of pp collisions at $\sqrt{s} = 8\,\text{TeV}$.

Results and Conclusions

Table 4.1 shows the predicted number of selected events in signal and background. Figure 4.2 shows the m_{4b} distribution in signal and background. In order to obtain the search sensitivity for 20 fb^{-1} of pp collisions at $\sqrt{s} = 8\,\text{TeV}$, an asymmetric mass window is defined around each signal mass, m_{G^*}, between $(\text{m}_{\text{G}^*} - 100)\,\text{GeV}$ and $(\text{m}_{\text{G}^*} + 50)\,\text{GeV}$. The signal efficiency and number of expected background events inside these windows is determined and they are used to calculate the value of cross section times branching ratio, $\sigma(pp \to G^* \to HH \to b\bar{b}b\bar{b})$, at which the number of signal events satisfies $N_{sig} = 3\sqrt{N_{bkg}}$. This estimate is used since, due to the low number of predicted background events, statistical uncertainty is likely to dominate over systematic uncertainty. These estimates of the point at which a 3σ significance observation could be made are shown in Figure 4.3. The predicted sensitivity of this search is down to ∼10 fb at resonance masses around 1 TeV, which is more sensitive than the $ZZ \to llqq$ channel for this signal model. These estimates would be degraded by detector systematic uncertainties but improved by optimisation of the analysis selection. The conclusion of this sensitivity study is that the $X \to HH \to b\bar{b}b\bar{b}$ is a very sensitive channel to any possible di-higgs resonance around 1 TeV in mass, which is a channel that, at the time of publication of this study [2], was unexplored with current LHC data. The remainder of this chapter deals with the implementation and results of this search using data collected with the ATLAS detector.

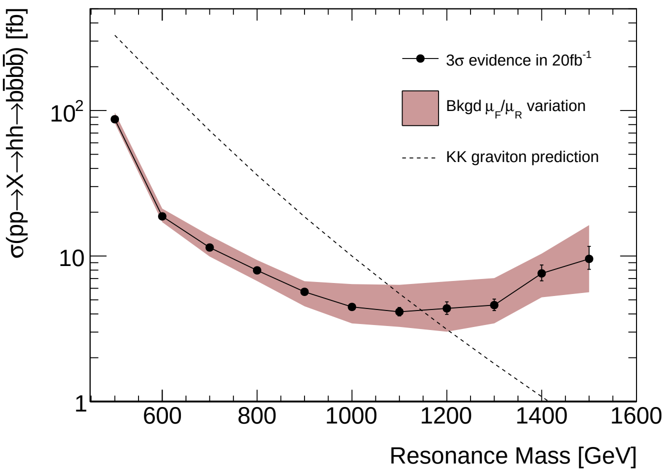

Figure 4.3.: The signal cross section × branching ratio needed to obtain 3σ evidence in $20\,\text{fb}^{-1}$ of pp collisions at $\sqrt{s} = 8\,\text{TeV}$. The error bars show the statistical uncertainties, and the shaded band indicates renormalization and factorization scale (μ_F/μ_R) uncertainties on the QCD MC. The predicted $G^* \to HH \to b\bar{b}b\bar{b}$ cross section is also shown, however this is affected by a bug which results in an overestimation of the cross section by a factor of ~10. Figure originally published in [2]

4.3. Event Selection

4.3.1. Optimisation of Event Selection

In order to decide on the values of the cuts used in the analysis selection, various studies were performed. This section summarises those studies. The final cuts were selected based on a compromise between performance and simplicity. The figure of merit used to optimise the cuts is the expected exclusion limits. An illustrative selection of these optimisation plots is given in Figures 4.4 to 4.6.

It is found that the analysis is not very sensitive to changing the value of the individual jet p_T cut and so a value of 40 GeV is chosen, as it is safely above the typical p_T of jets coming from pile-up or underlying event. The effect of varying the values of the cuts on dijet p_T and ΔR between the jets in the dijet is found to be strongly dependent on the signal mass other than in the case where the cut on ΔR is varied for values > 1.2.

One approach tested is to use two different sets of cuts for the high and low signal mass range, with the high mass range being defined as 900 GeV and above and the low as below 900 GeV. The optimal cut points for the high mass region were found to be:

- Leading dijet $p_{\mathrm{T}} > 400$ GeV
- Sub-leading dijet $p_{\mathrm{T}} > 325$ GeV
- Leading dijet $\Delta R_{bb} < 0.8$
- Sub-leading dijet $\Delta R_{bb} < 0.9$

Figure 4.4 shows the comparison of the high and low mass optimised selections. A substantial improvement in the sensitivity at higher masses is seen. However, in the end it was decided that having two separate selections was not worth the extra complexity and time added to the analysis.

In optimising the Higgs mass window cut on the dijets, the optimal value of a simple rectangular cut was initially found to be [100, 140] GeV. The more sophisticated approach of using an elliptical cut, as detailed in Section 4.3.4, was optimised and compared to the simple mass window. The comparison is shown in Figure 4.5 and it is seen that the elliptical cut gives an improvement in sensitivity across the entire mass range.

Various options for the b-tagging were investigated. Figure 4.6 shows the effect on the sensitivity of varying the b-tag efficiency point used. Other b-tagging strategies investigated include changing the requirement that all four jets are b-tagged to only requiring that at least three are; using different efficiency points on the leading and sub-leading dijets; and using a specifically charm-rejection trained algorithm to try and reduce the $t\bar{t}$ background fraction. Tagging all four jets with the MV1 70% working point is found to be the best mixture of performance and simplicity.

4.3.2. Data Selection

Data is only considered if it was taken at a point in time where the detector passes a set of data quality requirements, in order to ensure all the relevant components of the detector were operating correctly. In both data and MC, events are vetoed if they

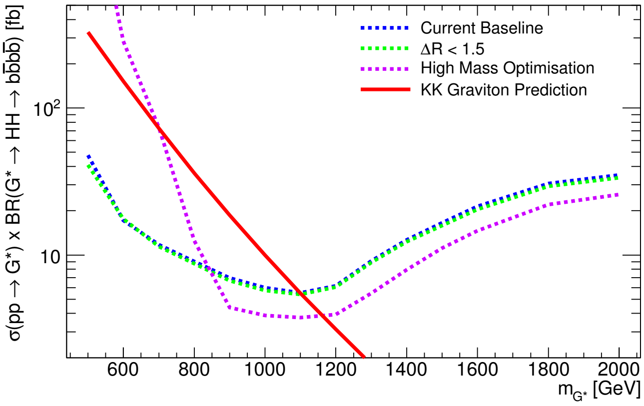

Figure 4.4.: The median expected exclusion limits in the HH channel, comparing different sets of cuts; (1) optimised for the overall mass range (2) the same as (1) but with the dijet ΔR cut changed from 1.2 to 1.5. (3) a selection optimised for signal masses of 900 GeV and above.

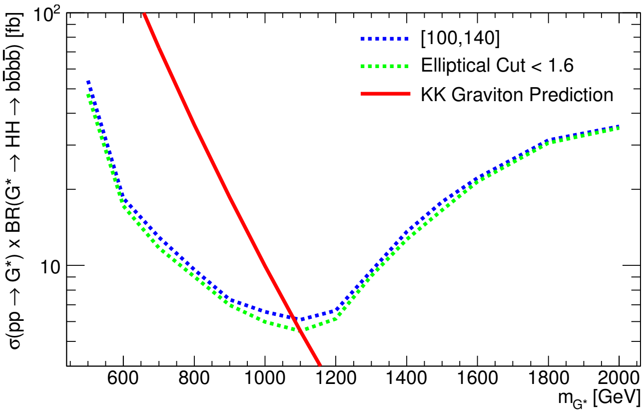

Figure 4.5.: The median expected exclusion limits in the HH channel, comparing the optimised elliptical m_h dijet mass cut with the optimised rectangular cut.

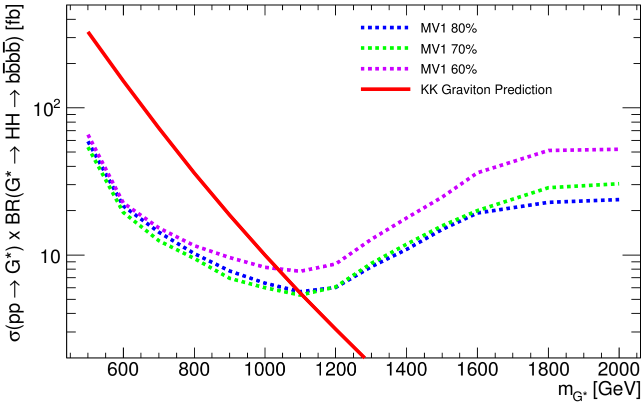

Figure 4.6.: The median expected exclusion limits in the HH channel, comparing different efficiency points of the MV1 b-tagging algorithm.

m_{G^*} [GeV]	500	600	700	800	900	1000	1100	1200	1300	1400	1500
Efficiency for $G^* \to HH$ (%)	99.5	99.7	99.9	99.9	99.8	99.8	99.5	99.6	99.7	99.9	99.8
Efficiency for $G^* \to ZZ$ (%)	99.4	99.5	99.4	98.6	98.4	98.5	98.7	99.0	99.3	98.3	99.3
Efficiency for $t\bar{t}$ (%)	95.9										

Table 4.2.: The predicted trigger efficiencies for the RS graviton → HH/ZZ mass points using the trigger selection and the $t\bar{t}$ MC, after applying the basic kinematic cuts

contain jets with $p_{\mathrm{T}} > 20$ GeV that fail the 'Looser' jet cleaning cuts as prescribed in [58]. This is intended to identify jets caused by noise in the detector, non-collision backgrounds and cosmic rays.

Both data and MC events are required to pass any of 5 triggers, which are described in Section 2.3. None of the 5 triggers had a prescale applied to them, meaning that every event which passed any one of the triggers was recorded. The efficiency of the 500 GeV mass graviton, in the HH channel, for events that pass the rest of the event selection is 99.5%. Table 4.2 shows the estimated trigger efficiency for the signal and $t\bar{t}$ MC samples.

4.3.3. Preselection

Together the cuts described below labelled 'Basic Kinematic Cuts' and '$t\bar{t}$ Veto' form the 'Preselection'.

Basic Kinematic Cuts

Jets are constructed in the event from clusters of energy deposits in the calorimeter using the anti-k_t algorithm [35] with a radius parameter of 0.4. These jets are calibrated to the hadronic jet energy scale, as described in Section 2.6.2. Muons within $\Delta R < 0.4$ of the jet axis are combined with the jet to take account of semi-leptonic decays of the b-quarks. The reconstructed muons are required to be within the inner detector acceptance ($|\eta| < 2.5$) and pass a variety of quality cuts. If multiple muons are matched to a jet, the one closest to the jet axis is used. The combination is performed by adding the 4-vectors of the jet and muon and by subtracting the estimated energy deposited into the calorimeter by the muon.

Jets are selected which fulfill the following requirements:

- $|\eta| < 2.5$
- $p_{\mathrm{T}} > 40\,\mathrm{GeV}$
- b-tagged using the MV1 tagging algorithm at the 70% efficiency point.
- if $|\eta| < 2.4$ and $p_T < 50\,\mathrm{GeV}$, then Jet vertex fraction, JVF > 0.5.

From the four highest p_{T} of these selected jets, pairs of the jets are formed by vectorially adding the jet 4-vectors. It is required that at least two independent (i.e. do not contain any of the same jets) dijets can be formed that satisfy the following criteria:

- Dijet $p_{\mathrm{T}} > 200$ GeV.
- Angular separation of the two jets ΔR(jet1,jet2) < 1.5.

If more then one dijet, which satisfies these requirements, can be formed containing the same individual jet, the dijet with the highest mass is selected.

$t\bar{t}$ Veto

After the selection cuts listed thus far, $t\bar{t}$ makes up 20% of the background. MC studies predict it is predominantly events where both top quarks have decayed via $t \rightarrow bW \rightarrow bcs$, and the c-jet has been mis-tagged as a b-jet. To reduce this component of the background there is a veto on events where a top candidate is reconstructed.

There are three hard partons from each top decay and so with six hard partons per event, there are, on average, more jets in $t\bar{t}$ events. First, any extra jets in the event are found. An extra jet is defined as a jet in the event, other than the four b-tagged jets which make up the signal candidate, which satisfy the requirements:

- $|\eta| < 2.5$
- $p_{\mathrm{T}} > 30\,\mathrm{GeV}$

- if $|\eta| < 2.4$ and $p_{\mathrm{T}} < 50\,\mathrm{GeV}$, then Jet vertex fraction, JVF > 0.5
- Angular separation of the dijet and the extra jet $\Delta R(\text{dijet, extra jet}) < 1.2$.

The extra jets are matched to the closest of the two dijets in R. If no extra jets are found, then the event passes the $t\bar{t}$ veto.

The variable m_W is defined as the invariant mass of the 2-jet system formed by adding the 4-vectors of the extra jet and the jet with the lower b-tagging weight of the matched dijet system. The variable m_t is defined as the mass of the three-jet system obtained by adding the 4-vectors of the extra jet and the matched dijet.

Figure 4.7 shows the distributions of m_W and m_t in the $t\bar{t}$ MC and the $G^* \to HH$ signal MC. Peaks at the W and top quark mass respectively are seen in the $t\bar{t}$ MC.

A variable that describes an ellipse around m_t and m_W is defined as:

$$X_{tt} = \sqrt{\left(\frac{m_W - 80.4}{0.1 m_W}\right)^2 + \left(\frac{m_t - 172.5}{0.1 m_t}\right)^2} \tag{4.1}$$

The values of 80.4 GeV and 172.5 GeV correspond to the approximate values of the masses of the W boson and top quark.

Events are vetoed if any extra jet and matched dijet gives $X_{tt} < 3.2$. The value of the cut is chosen to give ∼90% efficiency in the signal MC. The MC predicted signal efficiency is approximately independent of $\mathrm{m_{G^*}}$. After applying this veto the $t\bar{t}$ is estimated to make up less than 10% of the total background in the HH region.

4.3.4. Signal Region Definitions

Three orthogonal signal regions are defined for the decays $X \to HH$, $X \to ZZ$, and $X \to ZH$. These are defined as separate regions in the dijet masses plane. The signal regions were kept blind, meaning that the number of events in them or the distributions of those events were not observed, until the background models, systematic uncertainties and the statistical treatment of the search and limit setting were all fixed. This analysis focuses on the $X \to HH$ region. The $X \to ZZ$ region is also tested, however the $4b$ channel is less sensitive than the $llqq$ channel [81]. The $X \to ZH$ is not investigated and is kept blind for future investigation.

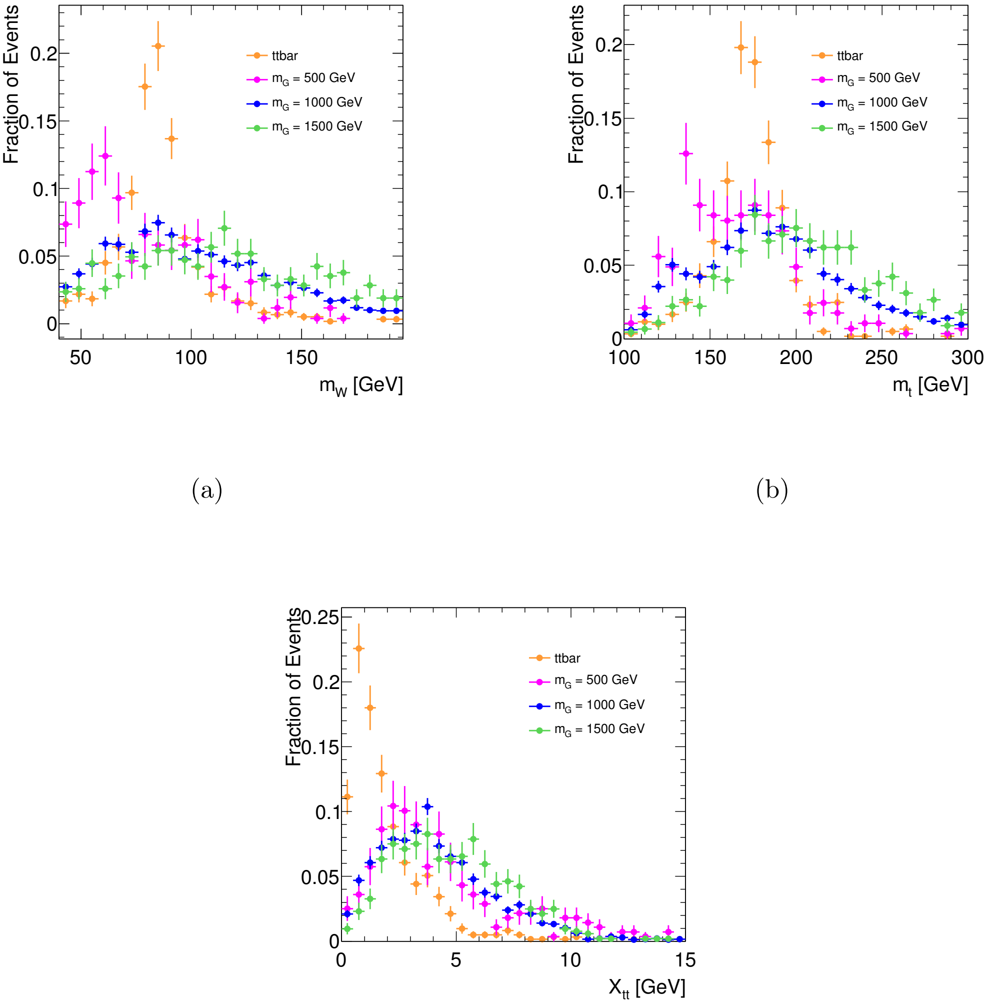

(a)

(b)

(c)

Figure 4.7.: The distribution of the variables used in the $t\bar{t}$ veto for the $G^* \rightarrow HH$ and $t\bar{t}$ MC. (a) the reconstructed W mass, (b) the reconstructed top mass, (c) the elliptical combination of these two reconstructed masses. It should be noted that only events with extra jets that pass the requirements have entries in these histograms and that the fraction of events passing those requirements is higher for $t\bar{t}$ events than for signal events.

The signal regions are defined as ellipses in the plane defined by the mass of the higher-p_{T} (leading) dijet, $\mathrm{m}_{\mathrm{2j}}^{\mathrm{lead}}$, and the mass of the lower-p_{T} (sub-leading) dijet, $\mathrm{m}_{\mathrm{2j}}^{\mathrm{subl}}$. The central values of the ellipses are chosen by investigating the median values of the innermost 90% quantile of the dijet masses predicted by the signal MC for different signal masses. The leading dijet is found to have a higher average mass than the sub-leading dijet. The variables that define the ellipses are:

$$X_{HH} = \sqrt{\left(\frac{\mathrm{m}_{\mathrm{2j}}^{\mathrm{lead}} - 124.0}{\sigma_{\mathrm{m}_{\mathrm{2j}}^{\mathrm{lead}}}}\right)^2 + \left(\frac{\mathrm{m}_{\mathrm{2j}}^{\mathrm{subl}} - 115.0}{\sigma_{\mathrm{m}_{\mathrm{2j}}^{\mathrm{subl}}}}\right)^2}, \tag{4.2}$$

$$X_{ZZ} = \sqrt{\left(\frac{\mathrm{m}_{\mathrm{2j}}^{\mathrm{lead}} - 93.0}{\sigma_{\mathrm{m}_{\mathrm{2j}}^{\mathrm{lead}}}}\right)^2 + \left(\frac{\mathrm{m}_{\mathrm{2j}}^{\mathrm{subl}} - 86.0}{\sigma_{\mathrm{m}_{\mathrm{2j}}^{\mathrm{subl}}}}\right)^2}, \tag{4.3}$$

$$X_{ZH} = \sqrt{\left(\frac{\mathrm{m}_{\mathrm{2j}}^{\mathrm{lead}} - 93.0}{\sigma_{\mathrm{m}_{\mathrm{2j}}^{\mathrm{lead}}}}\right)^2 + \left(\frac{\mathrm{m}_{\mathrm{2j}}^{\mathrm{subl}} - 115.0}{\sigma_{\mathrm{m}_{\mathrm{2j}}^{\mathrm{subl}}}}\right)^2}, \tag{4.4}$$

$$X_{HZ} = \sqrt{\left(\frac{\mathrm{m}_{\mathrm{2j}}^{\mathrm{lead}} - 124.0}{\sigma_{\mathrm{m}_{\mathrm{2j}}^{\mathrm{lead}}}}\right)^2 + \left(\frac{\mathrm{m}_{\mathrm{2j}}^{\mathrm{subl}} - 86.0}{\sigma_{\mathrm{m}_{\mathrm{2j}}^{\mathrm{subl}}}}\right)^2}, \tag{4.5}$$

where the $\sigma_{m_{2j}}$ represents the width of the mass distributions and is taken as $0.1m_{2j}$.

The ellipses are defined as the regions:

- $X_{HH} < 1.6$
- $X_{ZZ} < 1.5$
- $X_{HZ} < 1.6$ OR $X_{ZH} < 1.6$

The elliptical dijet mass requirement rejects 95% of the, mainly QCD, background events. Figure 4.8 shows the distribution in the dijet mass plane of signal events with a graviton mass of 500 GeV and the distribution of X_{HH} in signal. It is seen that the distribution of X_{HH} does not vary significantly with the signal mass. The

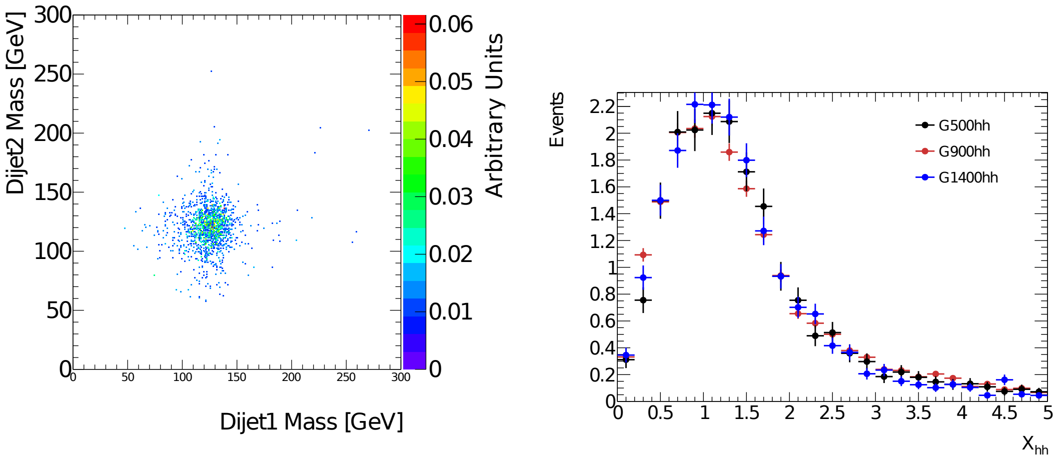

(a) (b)

Figure 4.8.: (a) A 2D histogram showing the leading and sub-leading dijet mass of HH decay signal MC events with a graviton mass of 500 GeV. (b) The X_{HH} of signal MC events with various dijet masses, normalised to equal area.

equivalent distributions in the ZZ decay mode are shown in Figure 4.9. There is a small overlap between the signal ellipses. In order to keep the regions separate; if an event is within both the HH and ZH ellipses it is attributed to the HH signal region and if an event lies within both the ZZ and ZH ellipses, it is attributed to the ZH signal region. Only a few percent of signal events are in these overlapping regions. The ZH signal region is kept blinded for future investigation.

Figures 4.10 show the bb-bb invariant mass distributions for the graviton signal model. It is seen that the spacing in between the signal masses adequately covers the spectrum, without leaving any significant gaps. Figure 4.11 shows the signal efficiencies as the cuts are implemented in sequence, as a function of graviton mass. The drop in efficiency for the 500 GeV mass point comes from the dijet p_{T} cut. The drop in efficiency towards the higher end of the mass spectrum comes from an increasing fraction of the dijets merging into a single jet as the p_{T} of the boson increases.

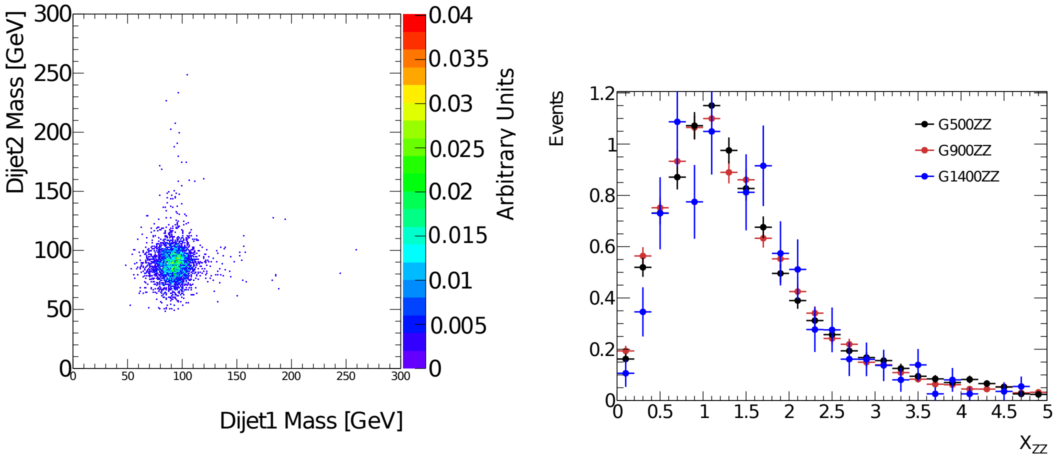

(a) (b)

Figure 4.9.: (a) A 2D histogram showing the leading and sub-leading dijet mass of ZZ decay signal MC events with a graviton mass of 500 GeV. (b) The X_{ZZ} of signal MC events with various dijet masses, normalised to equal area.

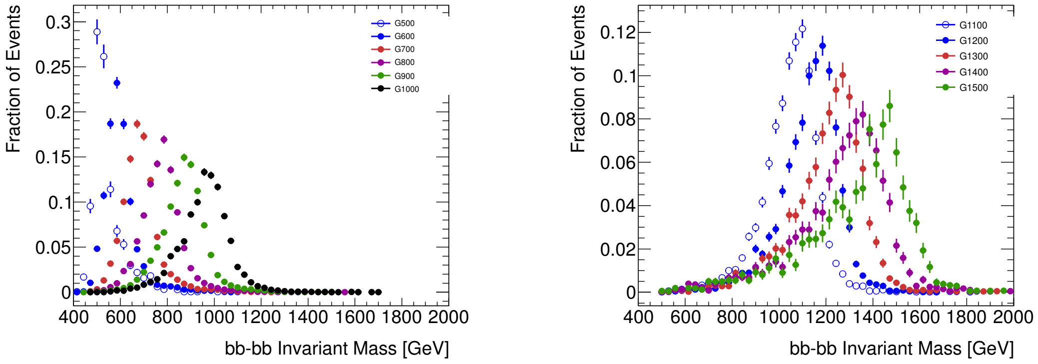

(a) (b)

Figure 4.10.: The *bb*-*bb* invariant mass distributions for the graviton → HH MC for the (a) 500 - 1000 GeV and (b) the 1100 - 1500 GeV mass samples.

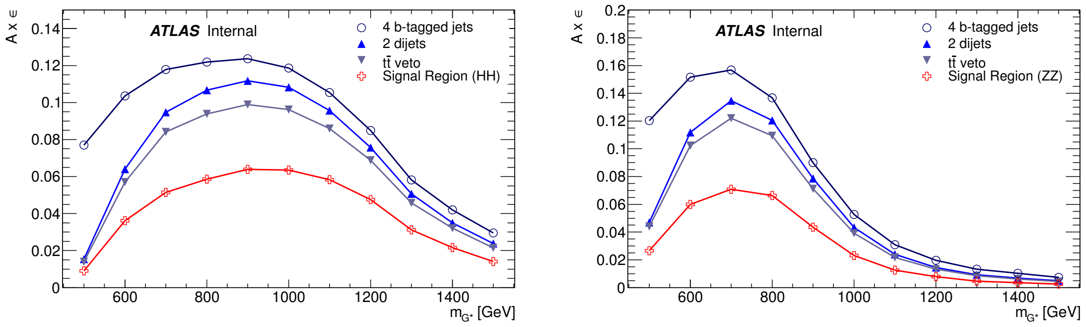

(a) (b)

Figure 4.11.: The signal efficiency times acceptance ($A \times \epsilon$) at various stages of the analysis cut flow for all the mass points in (a) the graviton → HH MC and (b) the graviton → ZZ MC

4.4. Background Models

When the event selection detailed in Section 4.3 is applied there are two main sources of background: QCD-produced multijets and $t\bar{t}$ production. There is also a small contribution from Z+jets. This section describes how these backgrounds are modelled.

The contribution of non-resonant production of $ZZ \to b\bar{b}b\bar{b}$ is roughly estimated using SHERPA MC events, which have not gone through the detector simulation. The analysis cuts are approximated by making the same selection on jets clustered out of stable particles. The b-tagging efficiency is approximated as 70%. The contribution in the signal region is estimated at $<<$ 1 fb and so is ignored.

4.4.1. Z+jets Background

PYTHIA 8 $Z \to b\bar{b}$ MC is used to model the Z+jets background. The normalisation is scaled using a k-factor defined as the ratio of the POWHEG+PYTHIA 8 NLO+PS prediction to the LO PYTHIA 8 prediction for $Z \to b\bar{b}$ events with $p_T^Z > 200$ GeV. The summary of the total background prediction in table 4.6 shows that Z+jets is a small component of the overall background.

4.4.2. QCD Background

The QCD background is modelled using data that passes a modified selection, with the kinematics reweighted to data passing the full selection in a separate region and where the normalisation is taken from that separate region.

Construction of the QCD Model

In order to construct and test the QCD background model, regions in the plane of the mass of the leading p_{T} dijet, $\mathrm{m}_{2\mathrm{j}}^{\mathrm{lead}}$, and the mass of the sub-leading p_{T} dijet, $\mathrm{m}_{2\mathrm{j}}^{\mathrm{subl}}$, are defined:

- **Sideband Region**: ($\mathrm{m}_{2\mathrm{j}}^{\mathrm{subl}} < 60\,\mathrm{GeV}$ OR $\mathrm{m}_{2\mathrm{j}}^{\mathrm{subl}} > 160\,\mathrm{GeV}$) OR ($\mathrm{m}_{2\mathrm{j}}^{\mathrm{lead}} < 60\,\mathrm{GeV}$ OR $\mathrm{m}_{2\mathrm{j}}^{\mathrm{lead}} > 160\,\mathrm{GeV}$)
- **Control Region**: $\mathrm{m}_{2\mathrm{j}}^{\mathrm{subl}} > 60\,\mathrm{GeV}$ AND $\mathrm{m}_{2\mathrm{j}}^{\mathrm{subl}} < 160\,\mathrm{GeV}$ AND $\mathrm{m}_{2\mathrm{j}}^{\mathrm{lead}} > 60\,\mathrm{GeV}$ AND $\mathrm{m}_{2\mathrm{j}}^{\mathrm{lead}} < 160\,\mathrm{GeV}$ AND (event is outside the HH, ZZ or ZH signal regions)

The region definitions are chosen to give an approximately equal number of data events in the Sideband and Control Regions. The regions are orthogonal to each other and to the signal regions.

The QCD model is made using events in data that pass a modified version of the selection listed in Section 4.3. The only difference in this modified selection is that instead of requiring both dijets to be made up of b-tagged jets, it is only required that at least one of the two is made of b-tagged jets. The modified selection will henceforth be referred to as the ‘2-tag selection’. In comparison the nominal analysis event selection will be referred to as the ‘4-tag selection’. There are 336340 data events passing this modified selection and those events are predicted to be dominated by QCD; the predicted $t\bar{t}$ contamination, using MC, is 2.0%. Figure 4.12 shows the Sideband and Control Regions in the $\mathrm{m}_{2\mathrm{j}}^{\mathrm{lead}}$-$\mathrm{m}_{2\mathrm{j}}^{\mathrm{subl}}$ plane for the events that pass this modified selection.

The normalisation of the QCD background model is set by scaling the number of data events passing the modified selection by the factor

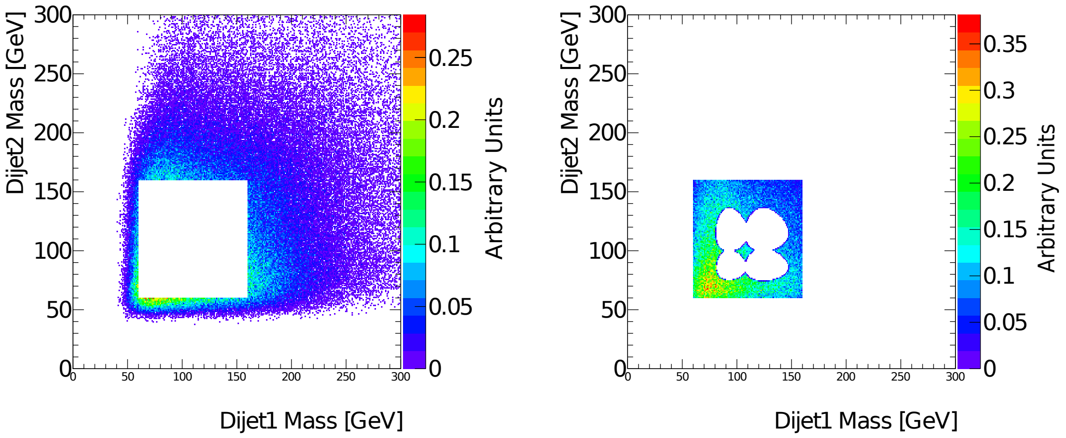

(a) Sideband Region

(b) Control Region

Figure 4.12.: The Sideband Region and Control Region in the $\mathrm{m}_{2\mathrm{j}}^{\mathrm{lead}}$-$\mathrm{m}_{2\mathrm{j}}^{\mathrm{subl}}$ plane for the 2-tag data sample. The ellipses that define the HH, ZZ and ZH signal regions are visible as excluded regions inside the Control Region.

$$\mu_{\mathrm{QCD}} = \frac{N_{\mathrm{data}}^{\mathrm{sideband}} - N_{\mathrm{t\bar{t}}}^{\mathrm{sideband}} - N_{\mathrm{Z+jets}}^{\mathrm{sideband}}}{N_{\mathrm{2\text{-}tag\ data}}^{\mathrm{sideband}}} \tag{4.6}$$

where $N_{\mathrm{data}}^{\mathrm{sideband}}$ is the number of events in the Sideband Region in data passing the full selection. $N_{\mathrm{t\bar{t}}}^{\mathrm{sideband}}$ and $N_{\mathrm{Z+jets}}^{\mathrm{sideband}}$ are the number of $t\bar{t}$ and Z+jets events in the Sideband Region predicted by the data-driven $t\bar{t}$ (see section 4.4.3) and Z+jets Monte Carlo samples respectively. $N_{\mathrm{2\text{-}tag\ data}}^{\mathrm{sideband}}$ is the number of events in the Sideband Region in the data passing the 2-tag selection. This scales the QCD background prediction to the data such that the total background (QCD + $t\bar{t}$ + Z+jets) exactly equals the data in the Sideband Region. In the Sideband Region, after the full selection, the non-QCD background sources make up a small fraction of the total background: for $t\bar{t}$ this is ~2%, and for the Z+jets it is ~1%.

Figures 4.13 show the distributions of various kinematic variables in the Sideband Region. The total background, after the normalisation of the QCD model, is compared to data passing the full selection. In most of these distributions there is a significant difference between the background model and the data. Since the total background is dominated by QCD, this must be a result of the difference between the 4-tag selection of the data and the 2-tag selection of the QCD model. Only requiring at least one of the two dijets to be b-tagged will affect both the flavour composition of the QCD and also the kinematics through the variation of the b-tagging efficiency as a function of the jet p_{T} and $|\eta|$ [80]. Since most jets here have p_{T} much higher than the b-quark mass, the variation of the b-tagging efficiency is thought to be the dominant effect.

In order to correct the discrepancy in the QCD model, each event in the model is reweighted to the data in the sideband region, using three kinematic variables:

- The p_{T} of the higher p_{T} dijet (Figure 4.13(a)).
- The ΔR between the jets in the lower p_{T} dijet (Figure 4.13(d)).
- The ΔR between the dijets (Figure 4.13(e)).

The reweighting is performed by calculating a weight as a product of the weights from the three individual 1D distributions and iterating this procedure 5 times in order to account for the correlations between the variables. The number of iterations is enough so that any more iterations make no appreciable difference. After this reweighting, the QCD model is again normalised to the data in the Sideband Region as before, in order to account for the change in the relative populations of the regions that the reweighting will incur.

Figures 4.14, show the distributions of various kinematic variables, comparing total background, after the normalisation and reweighting of the QCD model, to data passing the full selection, in the Sideband Region. The ratios of the variables which are reweighted on (Figures 4.14(a), 4.14(d) and 4.14(e)) are, as expected, in very close agreement. There is good agreement between the total background and data across all the other variables. Figure 4.14(f) shows the distribution of $\mathrm{m}_{4\mathrm{j}}$ in the Sideband region, which is the variable that is used in the search. It is well described by the background model.

Testing the Background Prediction in the Control Region

Since the Control Region is close to the signal regions and has a low predicted fraction of $t\bar{t}$, of ∼2%, it is used to test the QCD background model.

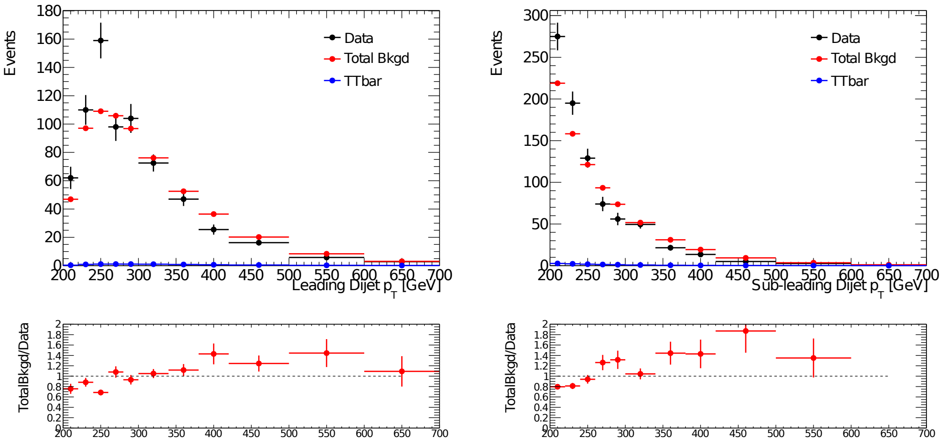

(a) Leading dijet p_T (b) Sub-leading dijet p_T

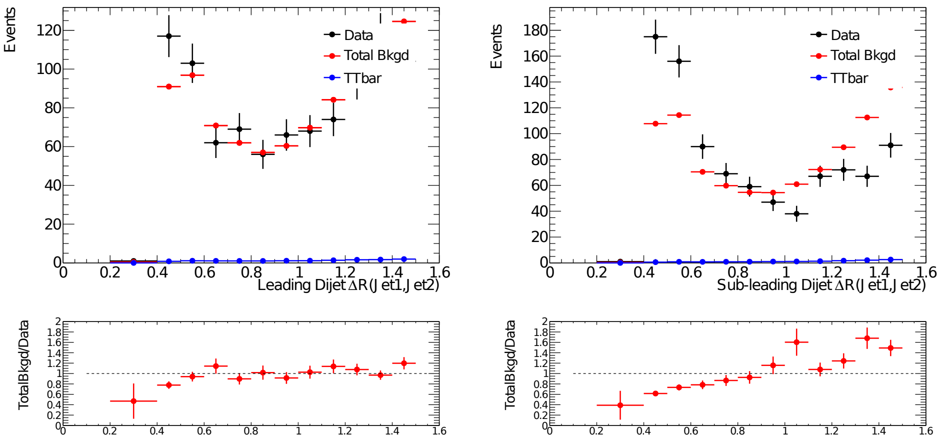

(c) Leading dijet jet-jet ΔR (d) Sub-leading dijet jet-jet ΔR

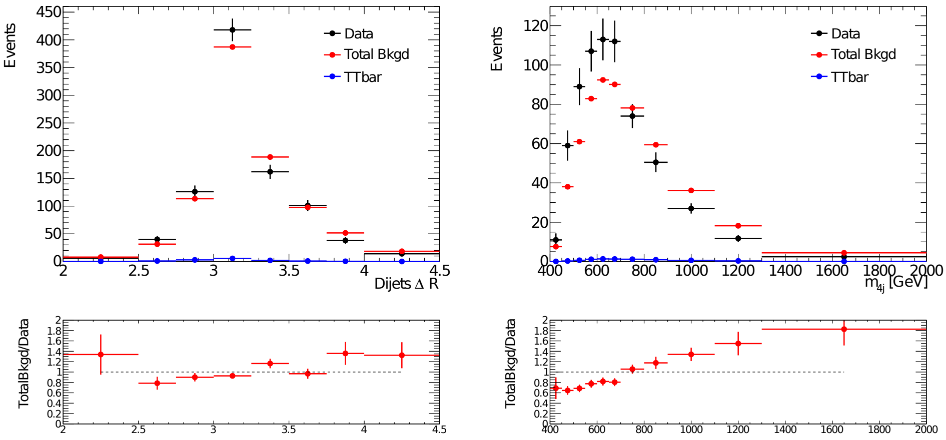

(e) ΔR separation of the dijets (f) $\mathrm{m_{4j}}$

Figure 4.13.: The distributions of various kinematic variables in the data and in the total background model, in the Sideband Region, before the reweighting of the QCD model. The $t\bar{t}$ component of the background is also shown.

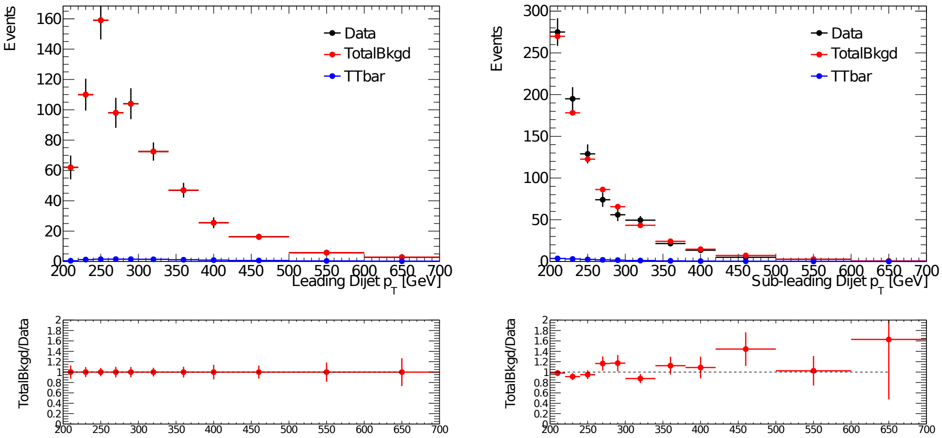

(a) Leading dijet p_{T} (b) Sub-leading dijet p_{T}

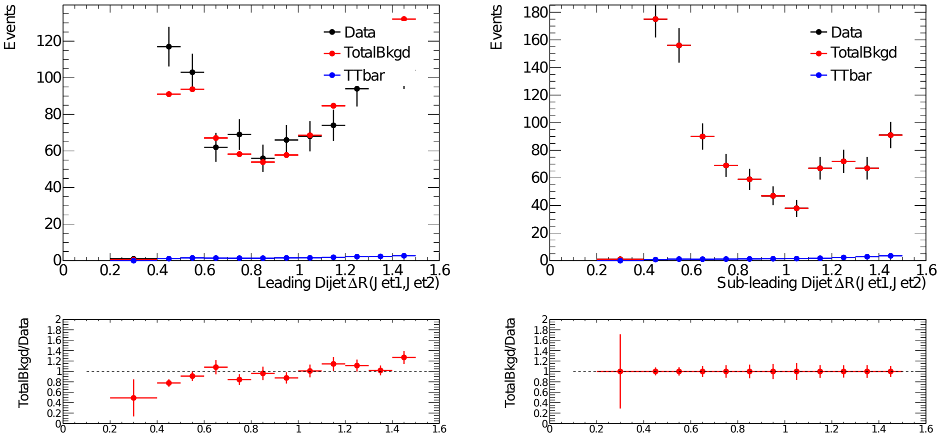

(c) Leading dijet jet-jet ΔR (d) Sub-leading dijet jet-jet ΔR

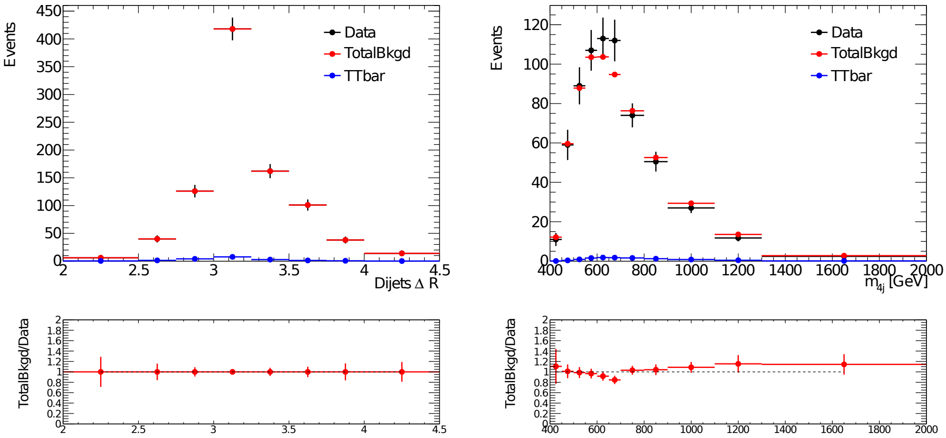

(e) ΔR separation of the dijets (f) $\mathrm{m}_{4\mathrm{j}}$

Figure 4.14.: The distributions of various kinematic variables in the data and in the total background model, in the Sideband Region, after the reweighting of the QCD model. The $t\bar{t}$ component of the background is also shown.

Sample	Entire $\mathrm{m}_{2\mathrm{j}}^{\mathrm{lead}}$-$\mathrm{m}_{2\mathrm{j}}^{\mathrm{subl}}$ plane	Sideband Region	Control Region
QCD	2346.2 ± 4.3	902.9 ± 2.6	935.4 ± 2.8
$t\bar{t}$	70.4 ± 0.4	19.0 ± 0.2	26.7 ± 0.3
Z+jets	40.7 ± 1.7	11.1 ± 0.9	16.9 ± 1.1
Total Bkgd	2457.3 ± 4.7	933.0 ± 2.8	978.9 ± 3.0
Data	2357 (± 48.5)	933 (± 30.5)	933 (±30.5)

Table 4.3.: The number of events in data and predicted by the background model after preselection and in the Sideband and Control Regions. The uncertainties on these numbers are purely statistical. The $\sqrt{N}$ of the data number is shown in parenthesis.

Table 4.3 shows the number of data and predicted background events after the analysis preselection without making any cuts on the dijet masses and in the Sideband and Control Regions. The number of data and background events are identical in the Sideband Region, since the background model is normalised in that region. In the Control Region the data and background prediction are in agreement at a level of 1.5σ. This agreement is used to set the systematic uncertainty on the normalisation of the QCD model, as described in Section 4.5.2. The equal number of 933 events in both the Sideband and Control regions is a coincidence.

Figures 4.15 show the distributions of various kinematic variables, comparing total background to data passing the full selection, in the Control Region. In general, the agreement is good. The agreement in the $\mathrm{m}_{4\mathrm{j}}$ distribution, shown in Figure 4.15(f), is used to set the systematic uncertainty on the shape of the QCD model, as described in Section 4.5.2.

4.4.3. $t\bar{t}$ Background

The $t\bar{t}$ background makes up ~10% of the total background. For a hadronically decaying top quark, taking two of the three resulting jets can often lead to a di-jet system with mass near m_H. For hadronic $t\bar{t}$, MC studies have shown that typically the events passing the selection have two mis-tagged charm quarks from the W boson decays.

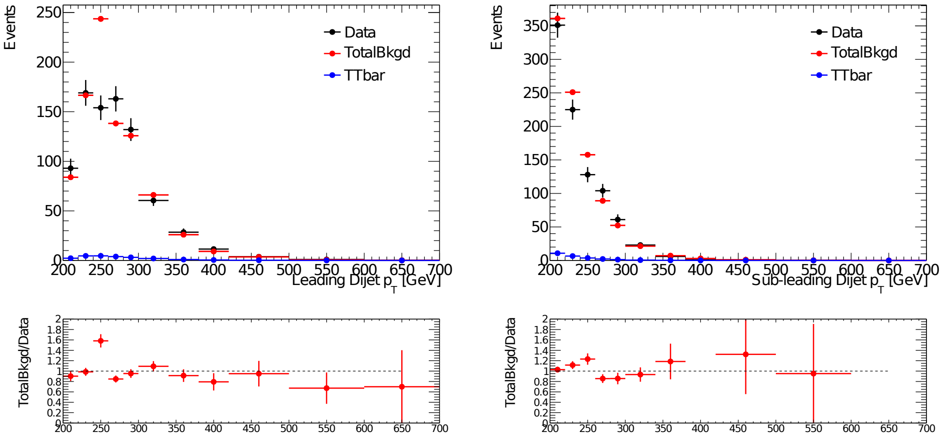

(a) Leading dijet p_T (b) Sub-leading dijet p_T

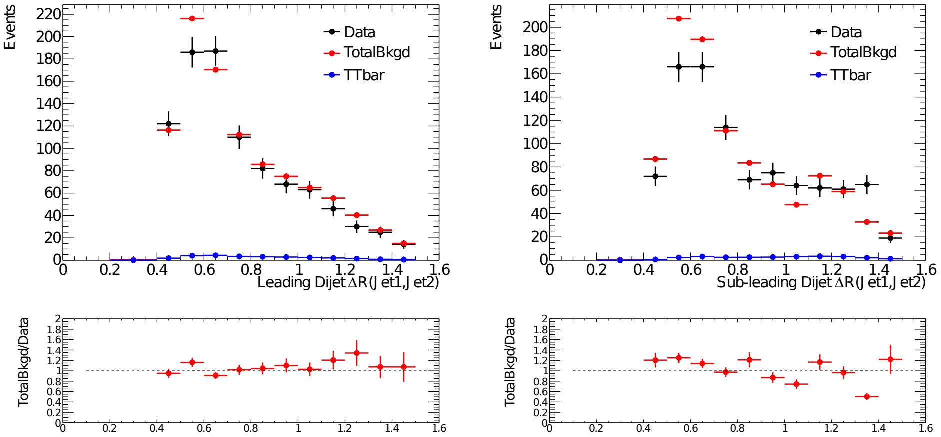

(c) Leading dijet jet-jet ΔR (d) Sub-leading dijet jet-jet ΔR

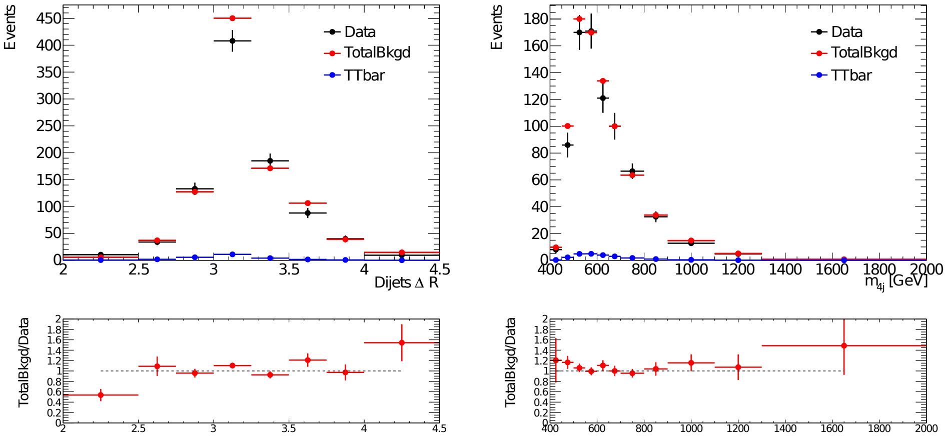

(e) ΔR separation of the dijets (f) m_{4j}

Figure 4.15.: The distributions of various kinematic variables in the data and in the total background model, in the Control Region. The $t\bar{t}$ component of the background is also shown.

$t\bar{t}$ Normalisation

Method Overview

A data driven method is used to estimate the $t\bar{t}$ normalisation. The method works using a $t\bar{t}$ control region, defined by reversing the $t\bar{t}$ veto, and then extrapolating the number of $t\bar{t}$ events in this region into the signal region using a value for the veto efficiency measured in a semi-leptonic $t\bar{t}$ data sample. The equation below is used to calculate the normalisation of the $t\bar{t}$ background:

$$N_{t\bar{t}}^{HH \text{ Region}} = \frac{\epsilon^2}{1-\epsilon^2} \times N_{t\bar{t}}^{\text{TT}HH \text{ Region}} \tag{4.7}$$

where ϵ is the $t\bar{t}$ veto efficiency, and $N_{t\bar{t}}^{\text{TT}HH \text{ Region}}$ is the number of $t\bar{t}$ events in the HH signal region, with the $t\bar{t}$ veto reversed. The equivalent equation is used for the ZZ region.

This method relies on the assumption that the probabilities for the dijets to pass the $t\bar{t}$ veto are uncorrelated and the assumption that the probability of a dijet passing the veto in the semi-leptonic data is the same as in the standard selection. Both of these assumptions are investigated with MC closure tests. The first assumption is tested by comparing the fractions of events in MC where both dijets pass the veto to the fraction of events where one dijet fails and one dijet passes the veto, and assessing the consistency of those two fractions with a single uncorrelated efficiency. The second assumption is tested by comparing the veto efficiencies in $t\bar{t}$ MC after the standard and semi-leptonic selections. No significant localised non-closure is found as a function of various kinematic variables. The closure tests find agreement at a level of better than 10% and this value is used as a systematic uncertainty on ϵ.

$t\bar{t}$ Control Region Using Reversed $t\bar{t}$ Veto

This section describes the determination of the number of $t\bar{t}$ events in the signal region with the $t\bar{t}$ veto reversed, $N_{t\bar{t}}^{\text{TT}HH \text{ Region}}$, of Equation 4.7. Reversing the $t\bar{t}$ veto means that if at least one of the dijets in the event fails the $t\bar{t}$ elliptical cut then

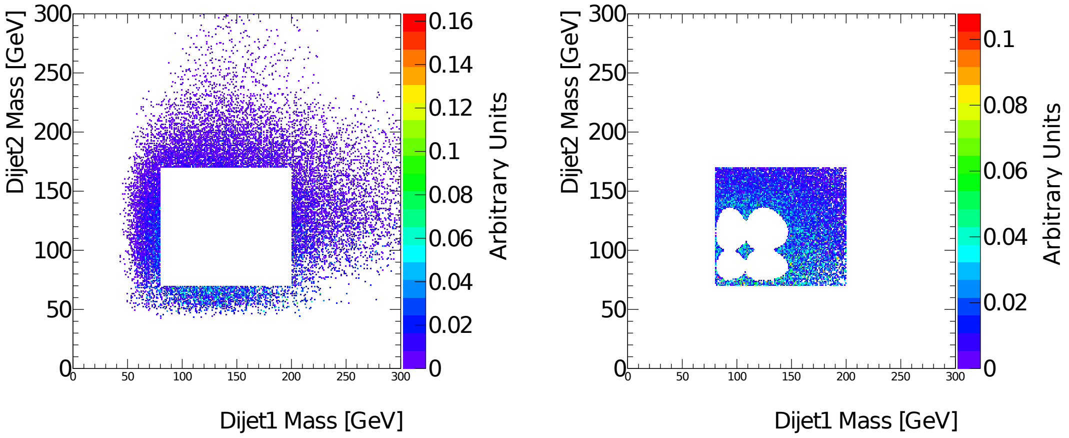

(a) TTSideband Region (b) TTControl Region

Figure 4.16.: The TTSideband Region and TTControl Region in the $\mathrm{m}_{2\mathrm{j}}^{\mathrm{lead}}$-$\mathrm{m}_{2\mathrm{j}}^{\mathrm{subl}}$ plane for the 2-tag data sample after reversal of the $t\bar{t}$ veto.

it is in this $t\bar{t}$ control region. Reversing the $t\bar{t}$ veto gives a data sample enhanced in $t\bar{t}$ events. The predicted composition is ∼70% QCD and ∼30% $t\bar{t}$.

In order to determine $N_{t\bar{t}}^{\mathrm{TT}HH\ \mathrm{Region}}$, a prediction for the number of QCD events in this region is needed. This is obtained in a way very similar to the QCD estimation for the standard selection described in Section 4.4.2.

Analogous regions to those used in the construction of the QCD background model are defined with the $t\bar{t}$ veto reversed. The regions are slightly different as they are optimised to have a QCD dominated TTSideband Region and a TTControl Region enhanced in $t\bar{t}$. The regions are defined as:

- **TTSideband Region**: ($\mathrm{m}_{2\mathrm{j}}^{\mathrm{subl}} < 70\,\mathrm{GeV}$ OR $\mathrm{m}_{2\mathrm{j}}^{\mathrm{subl}} > 170\,\mathrm{GeV}$) OR ($\mathrm{m}_{2\mathrm{j}}^{\mathrm{lead}} < 80\,\mathrm{GeV}$ OR $\mathrm{m}_{2\mathrm{j}}^{\mathrm{lead}} > 200\,\mathrm{GeV}$)
- **TTControl Region**: $\mathrm{m}_{2\mathrm{j}}^{\mathrm{subl}} > 70\,\mathrm{GeV}$ AND $\mathrm{m}_{2\mathrm{j}}^{\mathrm{subl}} < 170\,\mathrm{GeV}$ AND $\mathrm{m}_{2\mathrm{j}}^{\mathrm{lead}} > 80\,\mathrm{GeV}$ AND $\mathrm{m}_{2\mathrm{j}}^{\mathrm{lead}} < 200\,\mathrm{GeV}$ AND (event does not pass HH, ZZ or Zh signal ellipse selection)

Figure 4.16 shows the TTSideband and TTControl regions in data passing the 2-tag selection. The QCD is again modelled using the data passing the 2-tag selection, in this case with the $t\bar{t}$ veto reversed. The kinematics of the 2-tag data are reweighted to those of the 4-tag data in the TTSideband Region using the same variables and method for the QCD background in the standard selection. Instead of normalising this QCD prediction to the 4-tag data in the TTSideband Region, the prediction is normalised using the same value of μ_{QCD} calculated using Equation 4.6. This relies on the assumption that the ratio of QCD events passing the 2-tag and 4-tag selections is independent of the events passing the $t\bar{t}$ veto. This then gives an independent prediction of the QCD normalisation in the TTControl Region. Good agreement is seen when comparing the distributions of various kinematic variables between the background prediction and the data in the TTSideband Region.

Table 4.4 compares the number of events observed in data to the background prediction, with the $t\bar{t}$ veto reversed, in the different regions of the dijet mass plane. In the QCD dominated TTSideband Region, the data and background are in good agreement. The agreement in the TTControl Region is not as good, however this number is more sensitive to the $t\bar{t}$ prediction, which in the table is done using MC, which has detector and theoretical modelling systematics associated with it, which give an uncertainty of $\sim 30\%$. The last two columns of Table 4.4 show the number of events in the HH and ZZ Signal Regions with the $t\bar{t}$ veto reversed, that are observed in data and predicted by the background models. The number of $t\bar{t}$ events in the signal regions with the $t\bar{t}$ veto reversed are obtained by subtracting the QCD and Z+jets predictions from the number of events in data:

$$\begin{aligned} N_{t\bar{t}}^{\mathrm{TT}HH\ \mathrm{Region}} &= 16.0 \pm 6.9, \\ N_{t\bar{t}}^{\mathrm{TT}ZZ\ \mathrm{Region}} &= 0.8 \pm 3.9, \end{aligned}$$

where the uncertainties are statistical and are mainly due to the limited number of data events. This method assumes that there is no signal contamination in the HH and ZZ regions with the $t\bar{t}$ veto reversed. The efficiency of the signal to fail the $t\bar{t}$ veto is 10%, so this is a reasonable approximation.

Measurement of the $t\bar{t}$ Veto Efficiency

Selecting events containing a double b-tagged dijet and a leptonic top-quark candidate, provides a relatively pure data sample of $t\bar{t}$ events where the efficiency of the $t\bar{t}$ veto can be measured.

This semi-leptonic control region (SLCR) is defined by the following requirements:

Sample	TTSideband Region	TTControl Region	TTHH Region	TTZZ Region
QCD	122.8 ± 1.3	126.3 ± 1.2	30.9 ± 0.5	14.0 ± 0.4
$t\bar{t}$	19.6 ± 1.9	47.6 ± 2.9	23.0 ± 2.1	5.5 ± 1.0
Z+jets	1.2 ± 0.3	0.9 ± 0.2	0.1 ± 0.0	0.3 ± 0.1
Total Bkgd	143.6 ± 2.3	174.7 ± 3.2	54.0 ± 2.2	19.8 ± 1.1
Data	142.0 (± 11.9)	144.0 (± 12.0)	47.0 (± 6.9)	15.0 (± 3.9)

Table 4.4.: The number of events observed in data and predicted by the background model in the TTSideband and TTControl Regions. The prefix 'TT' denotes that the $t\bar{t}$ veto is reversed. The uncertainties are statistical only. The $\sqrt{N}$ of the data number is shown in parenthesis.

- Single muon trigger;
- Leptonic top candidate with $p_T > 200\,\text{GeV}$, defined by:
  - muon with $p_{\text{T}} > 25\,\text{GeV}$, which is isolated:
    - ∗ isolation using Inner Detector tracks: (sum of p_{T} of tracks) / (p_{T} of muon candidate) < 0.04 within cone of ΔR=0.2 around muon candidate;
    - ∗ isolation using calorimeter information: (sum E_T) / (E_T of muon candidate) < 0.07 within cone of ΔR=0.3 around muon candidate;
    - ∗ muon-jet overlap removal: reject muon candidate if within $\Delta R < 0.4$ of a jet with $p_{\text{T}} > 20$ GeV;
  - b-tagged jet;
  - angular separation between the muon and b-jet $\Delta R(\mu, b) < 1.2$;
- double b-tagged dijet.

The p_T of the leptonic top candidate is defined as the vector sum of the muon p_T, the b-jet p_T and the missing energy. The b-tagged jet in the semi-leptonic top candidate must be distinct from the b-jets in the dijet and so events in the SLCR have at least 3 b-tagged jets.

Observable	Before m_H Requirement	After m_H Requirement
N_P	182	78
N_F	80	47
ϵ from Data	0.695 ± 0.029	0.624 ± 0.043
ϵ from MC	0.656 ± 0.008	0.598 ± 0.012

Table 4.5.: The efficiency for a dijet in a $t\bar{t}$ event to pass the $t\bar{t}$ veto measured in data in the SLCR and predicted by $t\bar{t}$ MC. N_P/N_F are the number of events passing/failing the veto. The uncertainties are statistical only.

$t\bar{t}$ Veto Efficiency Results

Table 4.5 shows the efficiency for top events to pass the $t\bar{t}$ veto measured in the SLCR data and predicted by MC. There is reasonable agreement between the predicted and measured values. The veto efficiency is investigated as a function of kinematic variables of the dijet and no significant dependency is observed.

No significant dependence of the veto efficiency or the MC non-closure on dijet kinematics other than the mass of the dijet is observed. The values of the veto efficiency in the HH and ZZ signal regions are:

$$\epsilon_{H_{\text{Data}}} = 0.624 \pm 0.043(\text{stat}) \pm 0.062(\text{sys}), \tag{4.8}$$

$$\epsilon_{Z_{\text{Data}}} = 0.747 \pm 0.051(\text{stat}) \pm 0.075(\text{sys}). \tag{4.9}$$

The uncertainties are determined by the statistical uncertainty on the number of events in the SLCR and a conservative 10% systematic uncertainty from the MC closure studies.

$t\bar{t}$ Normalisation Prediction

Equation 4.7 is used to calculate the data-driven prediction of the $t\bar{t}$ background using the measured veto efficiency and the number of $t\bar{t}$ events in the region where the $t\bar{t}$ veto is reversed. The two values for the predicted number of $t\bar{t}$ events in the HH and ZZ signal regions are:

$$
\begin{aligned}
N_{t\bar{t}}^{HH\ \text{Region}} &= 10.2 \pm 6.0, \\
N_{t\bar{t}}^{ZZ\ \text{Region}} &= 0.9^{+5.0}_{-0.9}.
\end{aligned}
$$

The uncertainties on these numbers are discussed in Section 4.5.4.

As a cross check of the data-driven $t\bar{t}$ normalisation, the normalisation using MC is also obtained. The $t\bar{t}$ MC is normalised to the next-to-next-to-leading order + next-to-leading log (NNLO+NLL) cross section calculation, of 253 pb, and the p_{T} spectrum is reweighted to the unfolded $\sqrt{s} = 7$ TeV ATLAS measurement [82]. This results in a prediction of the number of $t\bar{t}$ events in the HH signal region of 14.3 ± 0.3 and in the ZZ signal region of 5.0 ± 0.1 events. The uncertainties are only the statistical uncertainties from the number of MC events passing the selection. These numbers are in good agreement with the data-driven prediction.

$t\bar{t}$ Shape

The small number of events in the reversed $t\bar{t}$ veto control region means that it is not possible to use this region to model the shape of the $t\bar{t}$ background. The shape is instead modelled using MC. However with the requirement of 4 b-tagged jets in the event, there are a small number of MC events passing, particularly at high $\mathrm{m}_{4\mathrm{j}}$. The solution chosen is to model the shape using $t\bar{t}$ MC events which pass the 2-tag selection, described above, where only one of the dijets is required to be made up of two b-tagged jets. The 2-tag selection gives a sample with a much larger number of $t\bar{t}$ MC events. The approximation that the difference between the 4-tag and 2-tag selections has a negligible impact on the $\mathrm{m}_{4\mathrm{j}}$ distribution is tested in Figure 4.17, where they are compared. They are consistent within the large statistical uncertainties of the 4-tag selected $t\bar{t}$ events. The systematic uncertainty on this approximation of the $t\bar{t}$ $\mathrm{m}_{4\mathrm{j}}$ shape is described in Section 4.5.4.

4.4.4. Total Background Prediction

The predicted number of background events in the HH and ZZ signal regions are summarized in table 4.6. The QCD and $t\bar{t}$ are derived using the data-driven methods described above, whist the Z+jets is from MC. The predicted background $\mathrm{m}_{4\mathrm{j}}$ distributions in the ZZ and HH signal regions are shown in Figure 4.18.

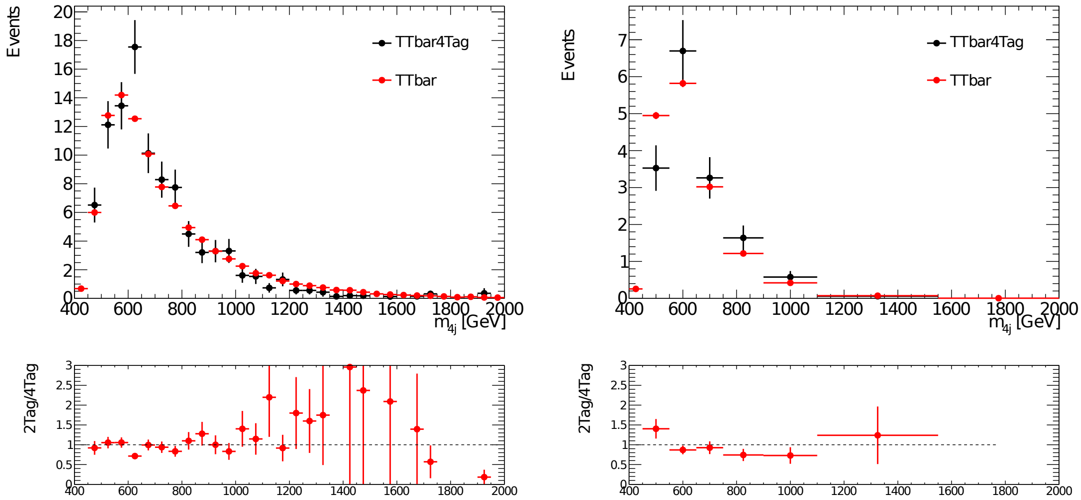

(a) (b)

Figure 4.17.: A comparison of the m$_{4\mathrm{j}}$ distributions produced from the $t\bar{t}$ MC after applying the full preselection (black) and 2-tag preselection (red). The distributions are normalised to equal area: (a) in the entire dijet masses plane (b) for events in the combined $HH + ZZ + ZH$ Signal Regions.

Sample	HH Region	ZZ Region
QCD	108.9 ± 5.4	140.0 ± 7.0
$t\bar{t}$	10.2 ± 6.0	0.9 ± 5.0
Z+jets	0.7 ± 0.2	6.1 ± 0.7
Total Bkgd	119.8 ± 8.1	147.1 ± 8.6

Table 4.6.: The number of predicted background events in each of the HH and ZZ signal regions. The uncertainties on the Z+jets number is purely statistical, reflecting the limited statistics in the Z+jets MC sample. The uncertainty on the $t\bar{t}$ and QCD is the full uncertainty on the data-driven methods explained in Section 4.4.3 for the $t\bar{t}$, and Section 4.5.2 for the QCD.

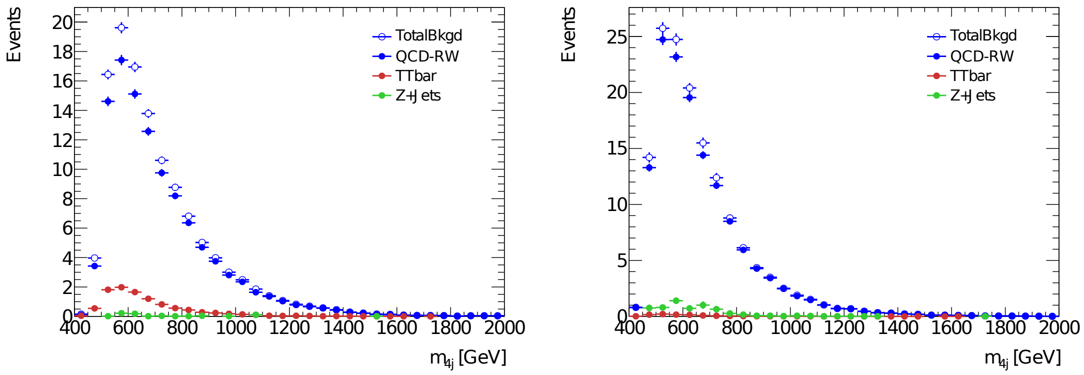

(a) HH Signal Region

(b) ZZ Signal Region

Figure 4.18.: The predicted background m_{4j} distributions in the Signal Regions. Showing the individual contributions from the QCD, $t\bar{t}$ and Z+jets models.

4.5. Systematic Uncertainties

4.5.1. Detector-based Uncertainties

There are two main types of systematic uncertainties to consider in this analysis. The first are uncertainties in the simulation of events. The Z+jets background component, which is modelled by MC, is $< 1\%$ of the total background and so uncertainties on this are neglected. For the $t\bar{t}$ shape, which is modelled by MC, there is a large uncertainty on the shape coming from the use of the 2-tag selection to approximate the 4-tag selection and since this is much larger than the effects on the shape of the modelling uncertainties, those are also ignored. Therefore this first class of uncertainties affects only the signal model. The second type of uncertainties come from the methods used to model the backgrounds.

There is an uncertainty arising from the modeling of the measured energy of jets, known as the jet energy scale (JES). The JES is calibrated and the uncertainties calculated as described in Section 2.6.2.

Another uncertainty comes from the modelling of the resolution of the detector's measurement of a jet's energy, referred to as the jet energy resolution (JER) uncertainty. This is assessed using the p_{T} balance of dijet events as described in section 2.6.2. This uncertainty is assessed by smearing the jet p_{T} by that uncertainty, which is dependant on the p_{T} of the jet. The opposite effect; where the JER is overestimated rather than underestimated, is not considered. This results in a one-sided, conservative estimate of this systematic uncertainty.

A third source of uncertainty comes from the modelling of the efficiency of b-tagging of jets containing a B-hadron. The uncertainty on this efficiency is evaluated by comparing the simulation to $t\bar{t}$ events in data, as described in Section 2.7.1. The size of the uncertainty is dependant on the p_{T} of the b-tagged jet and becomes large at $p_{\mathrm{T}} > 300$ GeV.

The last of these forms of uncertainty comes from the measurement of the integrated luminosity that the detector has recorded, which has a relative error of 2.8%, as described in Section 2.8.

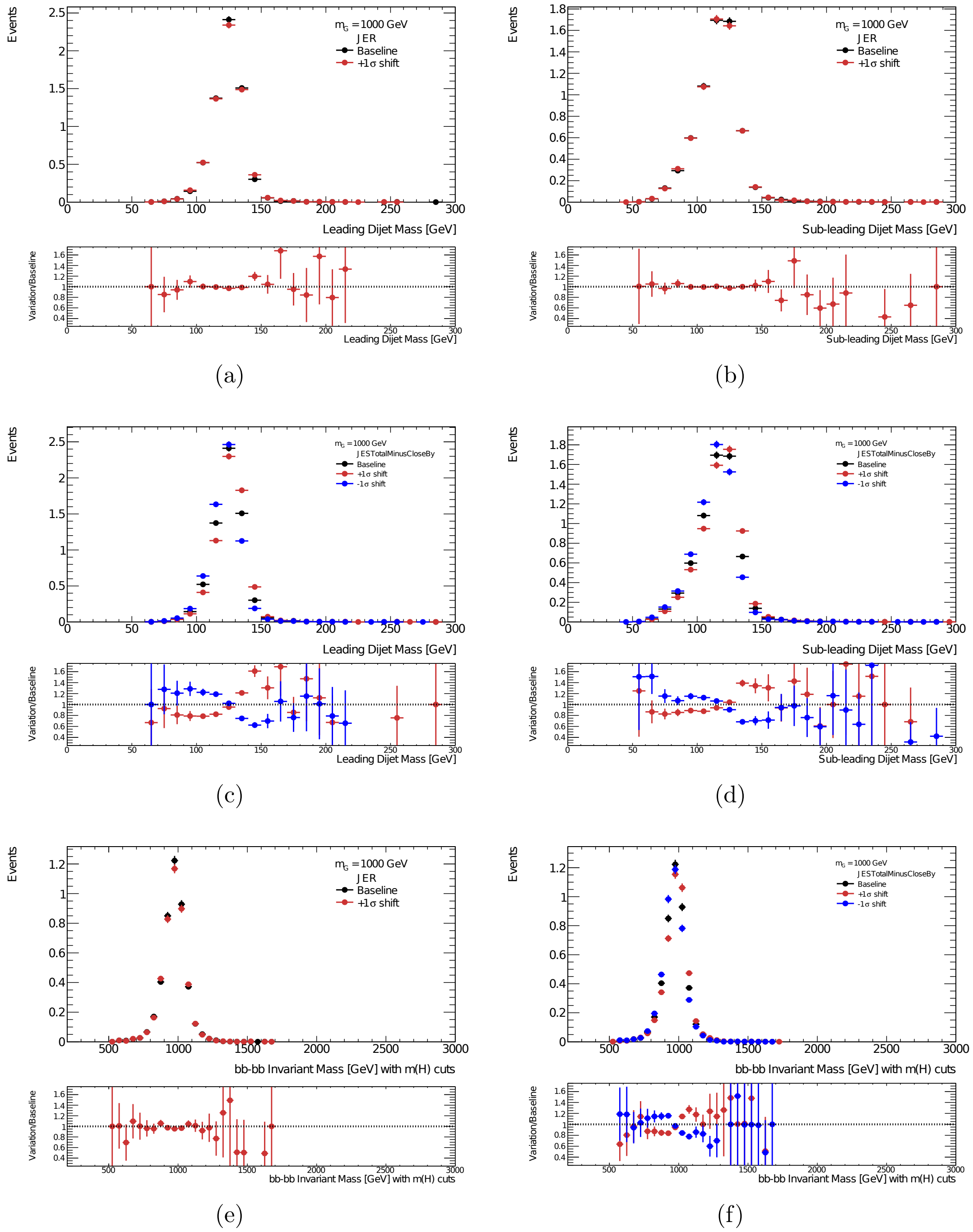

(a) (b)

(c) (d)

(e) (f)

Figure 4.19.: The effect of the jet energy uncertainty shifts on the $m_{G^*} = 1$ TeV signal MC. (a)/(b) The effect on the invariant mass of the leading/sub-leading dijet of the JER smearing. (c)/(d) The effect on the invariant mass of the leading/sub-leading dijet of the JES up and down shifts. (e)/(f) The effect on the m_{4j} distribution of the JER smearing/JES shifts.

	RS Graviton, $\mathrm{m_{G^*}}$ [GeV]										
Variation	500	600	700	800	900	1000	1100	1200	1300	1400	1500
JER	-1.57	-2.92	-2.91	-2.04	-3.01	-1.97	-0.856	-1.51	-2.09	-3.44	-1.76
JES Up	11.9	1.57	0.26	-0.346	-0.889	-0.806	-2.01	-2.41	-3.92	-3.56	-2.88
JES Down	-13.7	-6.79	-4.44	-2.39	-2.37	-1.81	-0.577	-0.396	0.667	-1.04	-2.77
b-Tagging Up	13.4	14.9	17.8	21.2	24.9	28.5	32.4	37	43.2	46.1	48.8
b-Tagging Down	-12.2	-13.5	-15.8	-18.5	-21.2	-23.8	-26.6	-29.7	-33.6	-35.1	-36.7

Table 4.7.: The percentage change in the predicted number of events passing the full analysis cuts, in the HH signal region, for each of the signal MC masses.

Figures 4.19 show the effect of the JER smearing and JES shifts on the masses of the individual dijets and on the $\mathrm{m_{4j}}$ distributions for the signal MC sample with a mass of 1000 GeV. For simplicity, the JES shifts shown are a combined effect of the different components of the uncertainty, whereas in the analysis the individual components of the uncertainty are used.

The percentage change in the number of events passing the full analysis selection, in the HH signal region, for the signal MC is shown in Table 4.7. Again, for the JES and also for the *b*-tagging uncertainties, the total shift is shown, rather than that due to the individual eigenvectors. The table shows that the *b*-tagging uncertainties dominate the uncertainty on the efficiency, except for the lowest mass point, and increase with the mass of the signal. Tables A.1 and A.2 in Appendix A show the impact of each individual *b*-tagging and JES eigenvector uncertainty component.

4.5.2. Uncertainty on QCD Background Normalisation

Table 4.3 compares the predicted number of background events to the data in the Control Region. The predicted fraction of QCD in the Control Region is 95%. The number of predicted events is consistent with the data to the level of $\sim 1.5\sigma$, neglecting the large systematic uncertainty on the $t\bar{t}$ prediction. Since the Control Region is in a similar space in the dijet masses plane to the signal regions, the level of agreement in the Control Region is used to set the uncertainty on the QCD normalisation in the signal regions. The systematic uncertainty is taken as the difference between the total background prediction and the data, giving a relative uncertainty of 5% ((978.9-933.0)/933.0).

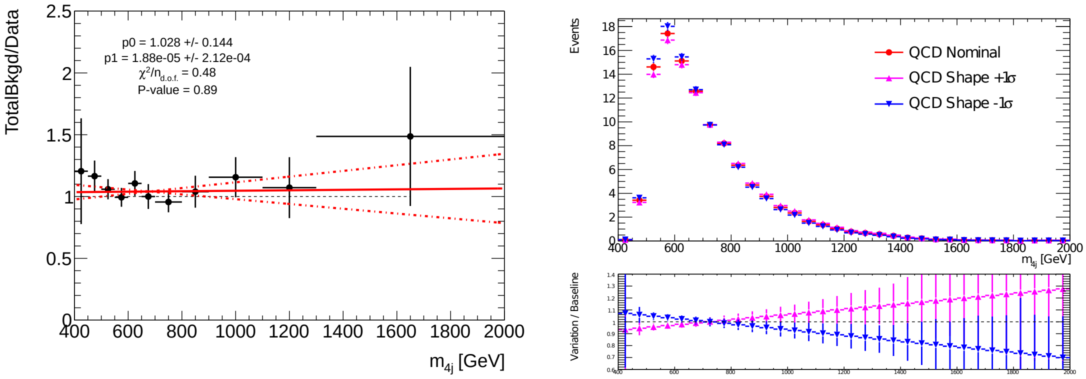

(a) (b)

Figure 4.20.: (a) A first order polynomial fit to the (Total Background)/Data ratio of the $\mathrm{m_{4j}}$ distribution in the Control Region. The dashed lines show the $\pm1\sigma$ uncertainties on the two fitted parameters. (b) The central QCD background prediction and the plus/minus QCD background shape variation histograms, for the HH signal region.

4.5.3. Uncertainty on QCD Background Shape

Figure 4.15(f) shows the $\mathrm{m_{4j}}$ distribution in the Control Region, comparing the background model to the data. The agreement in the shape here is used to set the systematic on the shape of the QCD background model. A linear fit is made to the ratio of background model to data, shown in Figure 4.20. This fit shows good compatibility with the data and is consistent with a gradient of 0, which shows that the shapes of the background model and data are consistent. The systematic is taken using the maximum of the $\pm1\sigma$ variations of the gradient of the linear fit and its inverse and reweighting the QCD background by a linear function with those gradients, whilst keeping the normalisation the same. The resulting $\pm1\sigma$ shifts of the QCD background model shape, in the HH signal region, are shown in Figure 4.20(b).

4.5.4. Uncertainty on $t\bar{t}$ Background Normalisation

The predicted number of $t\bar{t}$ events in the signal regions is stated in Section 4.4.3. The uncertainties are the combination of the statistical uncertainty on $N_{t\bar{t}}^{\mathrm{TT}HH\ \mathrm{Region}}$ and the statistical and systematic uncertainties on the measured veto efficiency. The overall uncertainty is dominated by the statistical uncertainty on $N_{t\bar{t}}^{\mathrm{TT}HH\ \mathrm{Region}}$ due to the small number of data events in the reversed $t\bar{t}$ veto Signal Region. This gives a

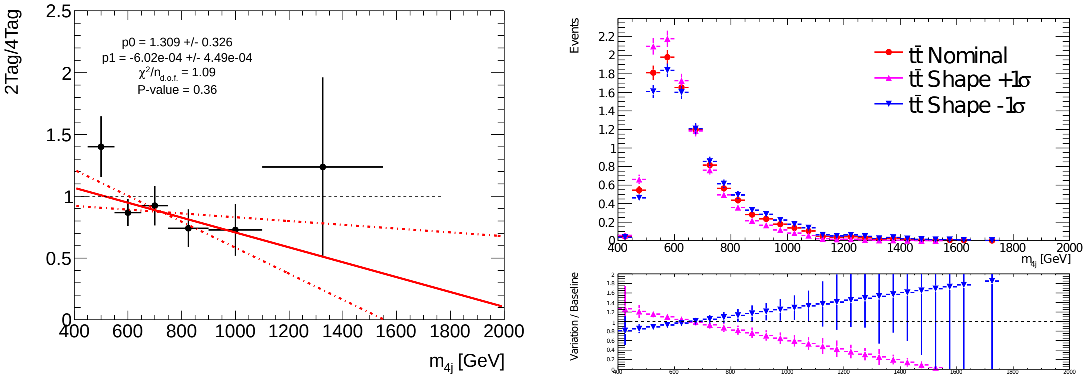

(a) (b)

Figure 4.21.: (a) A straight line fit to the 2-Tag/4-Tag ratio of the $\mathrm{m}_{4\mathrm{j}}$ distribution in the HH+ZZ+ZH signal region of the $t\bar{t}$ MC. The dashed lines show the $\pm 1\sigma$ uncertainties on the two fitted parameters. (b) The central $t\bar{t}$ background prediction, and the plus/minus $t\bar{t}$ background shape variation histograms, for the HH signal region.

58% uncertainty for the HH selection, and a 522% uncertainty for the ZZ selection. The $t\bar{t}$ background comprises less than 1% of the total background in the ZZ signal region compared to 9% in the HH signal region.

4.5.5. Uncertainty on $t\bar{t}$ Background Shape

As described in Section 4.4.3, the $t\bar{t}$ background shape is modelled using MC that passes the modified 2-tag selection. The comparison between the 2-tag and 4-tag selected $t\bar{t}$ events in Figure 4.17 is used to set the shape uncertainty on the $t\bar{t}$ background model. Figure 4.21 shows the linear fit to the ratio of 2-tag to 4-tag $t\bar{t}$ and the maximum gradient of the $\pm 1\sigma$ uncertainties are used to set the shape variations in the same way as for the QCD model shape systematic. The resulting shape shifts on the $t\bar{t}$ model are shown in Figure 4.21(b).

The source of this shape uncertainty is the possible differences between the 2-tag and 4-tag selections and so this does not account for possible mis-modelling of the $t\bar{t}$ kinematics by the MC. However this shape uncertainty is large and when it is implemented into the limit setting, it has a negligible impact on the final limit, as can be seen in Figure 4.26. Based on these considerations, the shape uncertainty from $t\bar{t}$ MC mis-modelling can be ignored.

4.6. Introduction to Limit Setting

4.6.1. The Likelihood Ratio

If a search for new physics in a particular final state finds no significant deviation from the background prediction, the observed data is often used to set upper limits on relevant BSM models.

When considering setting an upper limit on a specific new physics model, we are comparing the data to two hypotheses: the background-only hypothesis and the signal+background hypothesis. The Neyman-Pearson lemma [83] shows that the ratio of the likelihoods of the data, given the two competing hypotheses, is the most powerful test statistic to use when making a test of two hypotheses.

In the case of a binned histogram we define the number of entries in bin i as n_i for the number in data and $\mu s_i + b_i$ for the expected number from the signal+background model, where μ is the signal normalisation ($\mu = 0$ in the case of the background-only model). The value of the likelihood, using poisson statistics is:

$$L(\mu, \boldsymbol{\theta}) = \prod_{i=1}^{N} \frac{(\mu s_i + b_i)^{n_i}}{n_i!} e^{-(\mu s_i + b_i)}. \tag{4.10}$$

Here, the likelihood is also a function of a set of nuisance parameters denoted by $\boldsymbol{\theta}$. In our case, these are the systematic uncertainties of the signal and background model.

In order to use the data to constrain the values of the nuisance parameters, the ratio of so-called profile likelihoods is used as the test statistic. In this case, what is meant by a profile likelihood is to first form a likelihood which is composed of Equation 4.10, together with an additional constraint term for each systematic uncertainty, then to find the maximum value of that likelihood, varying the systematic uncertainties. Typically, the constraint terms are Gaussian, log-normal or delta functions. The test statistic is intended to test the compatibility of the data with the signal+background hypothesis.

4.6.2. CL_s

A procedure used in previous HEP experiments was to exclude models based on the statistic CL_{s+b}, which is equivalent to the probability of the signal+background model producing data which gives the same or less compatibility with the signal+background hypothesis than the observed data, according to the value of the test statistic. The value of the signal normalisation at which $CL_{s+b} = 0.05$ was used as the upper limit at 95% 'confidence level'.

The main problem with this technique arises in the case where the data has a significant downwards fluctuation. If the observed data is significantly below the background-only prediction then the signal+background hypothesis can be ruled out at very low values of μ, below what the test is really able to distinguish from the background.

Instead, a statistic called CL_s [84] is used as the basis of exclusion which takes into account the ability of the test to distinguish between the background-only and signal+background hypotheses:

$$CL_s = \frac{CL_{s+b}}{CL_b}, \tag{4.11}$$

where CL_b is the probability for the background-only hypothesis to produce data which gives the same or less compatibility with the signal+background hypothesis than the observed data, according to the value of the test statistic. Since the test statistic here is testing compatibility with the signal+background hypothesis; $CL_{s+b} \leq CL_b$ and so $0 \leq CL_s \leq 1$. However, CL_s is not strictly a probability.

In order to find the observed and expected exclusion limits, we need to scan over values of μ calculating the value of CL_s at each point in order to find the point where $CL_s = 0.05$. To calculate the value of CL_s at a particular value of μ, the distribution of the test statistic is needed in order to calculate the probabilities given the signal+background and background-only hypotheses. In practice, these distributions are obtained by generating lots of data-sets randomly sampled from the signal+background/background-only models, known as 'pseudo-experiments' or ‘toy MC’. Another approach is to use approximations to obtain an analytical form of the distribution.

4.7. Search For Deviations from the Background Model

A test is made of the data upon unblinding to search for any statistically significant deviation from the background model in the $\mathrm{m_{4j}}$ distribution. The test statistic used is a one sided profile likelihood ratio:

$$q_0 = \begin{cases} -2\ln\frac{L(0,\hat{\hat{\boldsymbol{\theta}}}(0))}{L(\hat{\boldsymbol{\mu}},\hat{\boldsymbol{\theta}})} & \hat{\mu} > 0 \\ 0 & \hat{\mu} < 0, \end{cases} \tag{4.12}$$

where μ is the value of the signal normalisation considered, $\hat{\mu}$ is the maximum likelihood (ML) value of μ, $\boldsymbol{\theta}$ are the set of nuisance parameters, $\hat{\boldsymbol{\theta}}$ is the ML value of $\boldsymbol{\theta}$ and $\hat{\hat{\boldsymbol{\theta}}}$ is the ML value of $\boldsymbol{\theta}$ when μ is fixed at a particular value. L denotes the profile likelihood, $L(\hat{\mu}, \hat{\boldsymbol{\theta}})$ is the likelihood where μ is allowed to take any value, the unconstrained likelihood. $L(0, \hat{\hat{\boldsymbol{\theta}}})$ is the likelihood for the value of $\mu = 0$, the constrained likelihood. In this case $\mu = 1$ corresponds to the predicted number of signal events.

This tests the compatibility of the data with the background hypothesis, $\mu = 0$. The local p-value of a set of data, p_0, is defined as the probability for the background-only hypothesis to have a value of q_0 that is as high or higher than the value of q_0 in that data. In order to obtain p_0, pseudo-experiments are generated with the background-only model and the distribution of the test statistic, q_0, is built up from the values of the pseudo-experiments.

The signal models tested are the RS Graviton with masses between 500 and 1500 GeV at 100 GeV intervals.

If a local p_0 value is obtained that corresponds to a significance of greater than 3σ then a correction for the look elsewhere effect will be computed in order to obtain the global p-value. This correction is obtained using the distribution of the test statistic, q_0, in background-only pseudo-experiments. The average number of upwards crossings, $< N_{1\sigma} >$, across the mass range tested of q_0 at the value of q_0 corresponding to 1σ significance, $q_0^{1\sigma}$, is estimated using the average number from the background-only pseudo-experiments and is used to obtain the correction to the local p-value using the equation [85]:

$$p_0^{global} = p_0^{local} + < N_{1\sigma} > e^{-(q_0^{max} - q_0^{1\sigma})/2} \tag{4.13}$$

Where p_0^{local} is the lowest p_0 value across the mass range tested, corresponding to a test statistic value of q_0^{max}.

4.8. Setting Upper Limits on the Graviton Model

On unblinding of the signal region a test of the background-only hypothesis is performed using the procedure detailed in the previous section. Provided a significant deviation from the background-only hypothesis (defined as a global p-value corresponding to a significance in excess of 3σ) is not observed, upper limits are set on the RS graviton signal cross section using the procedure described below.

4.8.1. Choice of Exclusion Statistics

To evaluate an upper limit of $\sigma(G^* \to HH/ZZ \to b\bar{b}b\bar{b})$ we use a frequentist method where a cross section is excluded on the basis of the statistic CL_s, which is defined as the ratio of CL_{s+b} to CL_b, as described in section 4.6.2. Cross sections are excluded if they have a value of $CL_s \leq 0.05$.

In order to calculate the p-values used to determine CL_{s+b} and CL_b from the $\mathrm{m_{4j}}$ distribution, a test statistic is required. The test statistic chosen is a one-sided profile likelihood ratio defined as:

$$\widetilde{q_\mu} = \begin{cases} -2\ln\frac{L(\mu,\hat{\hat{\boldsymbol{\theta}}}(\mu))}{L(0,\hat{\hat{\boldsymbol{\theta}}}(0))} & \hat{\mu} < 0 \\ -2\ln\frac{L(\mu,\hat{\hat{\boldsymbol{\theta}}}(\mu))}{L(\hat{\mu},\hat{\boldsymbol{\theta}})} & 0 \leq \hat{\mu} < \mu \\ 0 & \hat{\mu} > \mu, \end{cases} \tag{4.14}$$

where, μ is the value of the signal normalisation considered, $\hat{\mu}$ is the maximum likelihood (ML) value of μ, $\boldsymbol{\theta}$ are the set of nuisance parameters, $\hat{\boldsymbol{\theta}}$ is the ML value of $\boldsymbol{\theta}$ and $\hat{\hat{\boldsymbol{\theta}}}$ is the ML value of $\boldsymbol{\theta}$ when μ is fixed at a particular value. L denotes the profile likelihood, $L(\hat{\mu}, \hat{\boldsymbol{\theta}})$ is the likelihood where μ is allowed to take any value, the unconstrained likelihood. $L(\mu, \hat{\hat{\boldsymbol{\theta}}})$ is the likelihood for a particular fixed value of μ, the constrained likelihood.

The definition of the test statistic, $\widetilde{q_\mu}$, takes into account the fact that we're searching for a resonance on top of a background and so the case where $\mu < 0$ is unphysical.

In order to obtain the distributions of the test statistic, $\widetilde{q_\mu}$, the equations derived in [86] are solved numerically. These equations are derived using approximations of the distribution of $\hat{\mu}$ as Gaussian and the asymptotic approximation of the distribution of the profile likelihood ratio to a non-central chi-squared distribution. In order to test the validity of this method for the search, studies using toy MC data-sets are carried out, which are detailed in the following section.

4.8.2. Validation with Toy MC Studies

In order to validate the asymptotic approximation method of obtaining the exclusion limits, limits are produced using the toy MC method and compared to those from the asymptotic method. Using toy MC to obtain the distribution of the test statistic doesn't rely on the approximations used in the asymptotic method, however it takes a factor of $\sim$100 more CPU time.

The method works by generating datasets that are randomly sampled from the background and signal+background models, calculating the value of $\widetilde{q_\mu}$ for each individual dataset and then plotting these in a histogram to obtain the distributions of $\widetilde{q_\mu}$ and hence the p-values. A few example distributions for different values of μ

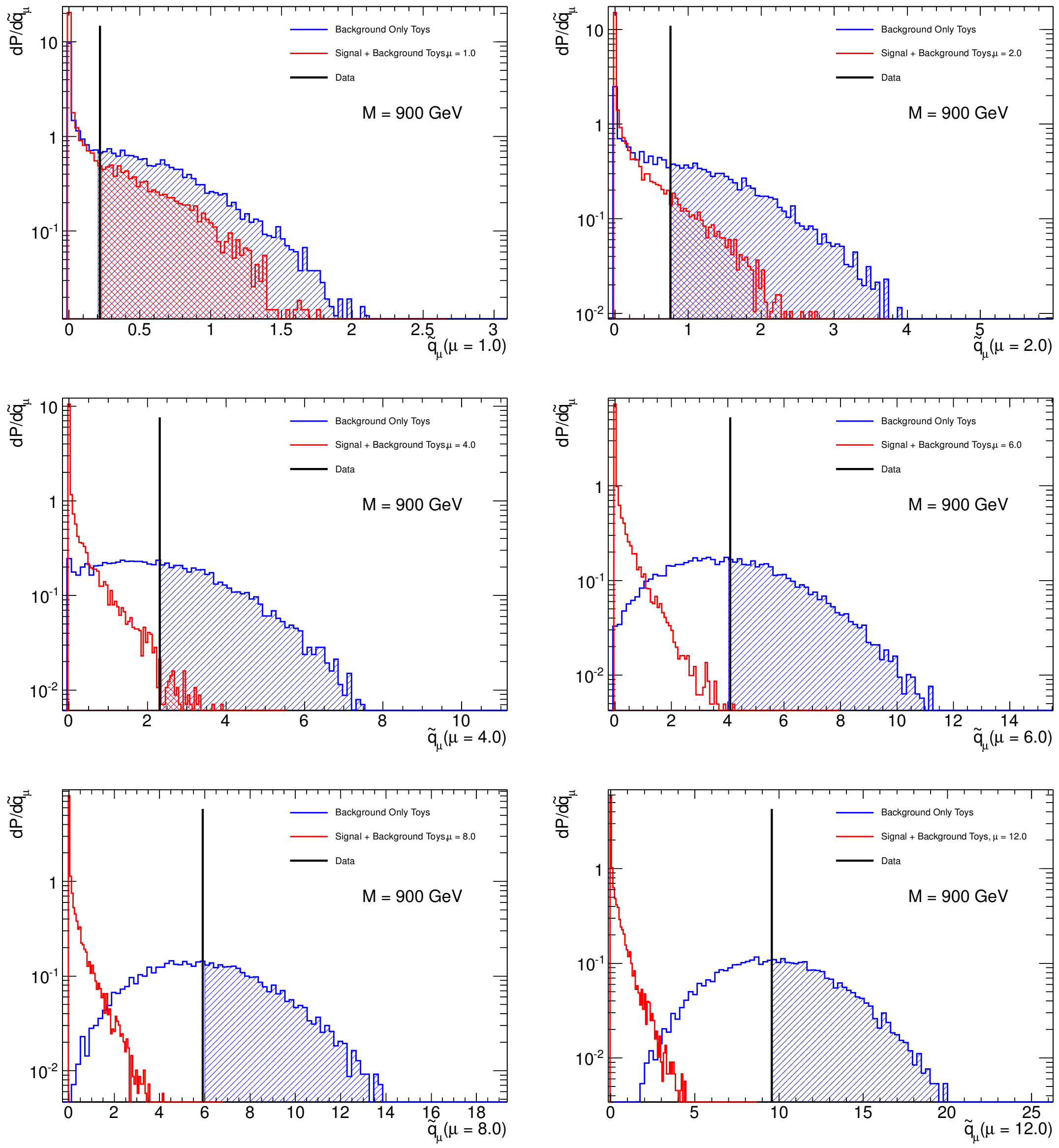

Figure 4.22.: The test statistic distributions from 10000 toy MC datasets for both background-only and signal + background models. The distributions here are all for the 900 GeV signal mass point and are for various values of the signal normalisation, μ. Since the search is blinded, the data point actually corresponds to the central background-only value.

are shown in Figure 4.22. These example distributions do not take into account any systematic uncertainties.

The exclusion limits, for an individual signal mass point, are obtained by scanning over the values of μ, generating 10000 background-only and 10000 signal+background

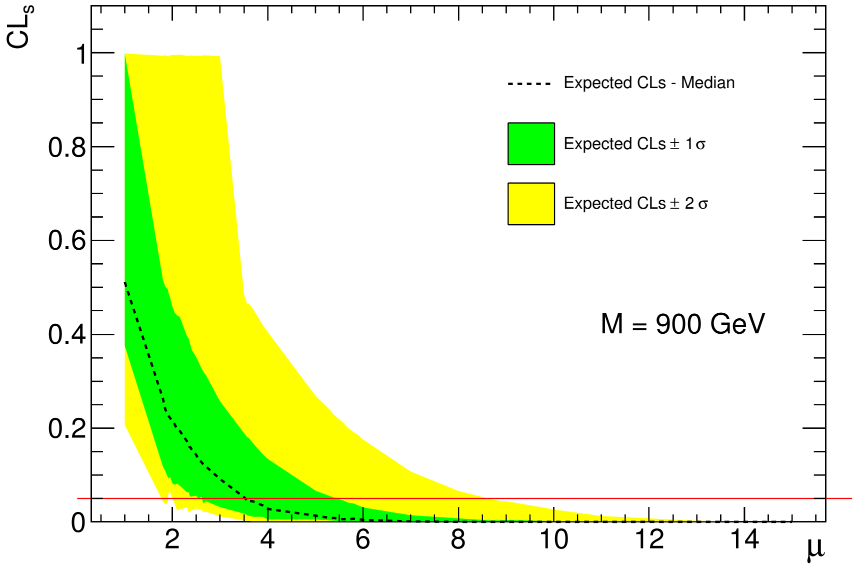

Figure 4.23.: The scan over signal normalisation, μ, for the 900 GeV signal mass point in the HH channel. The p-values are obtained from the generation of toy MC datasets for each point.

toys to find the p-values in order to calculate CL_s at that μ point and interpolating to find the value of μ at which $CL_s = 0.95$. This is done for the data point in the case of the observed limit, for the median value of the background-only distribution in the case of the expected limit and for the points which contain 68%/95% of the background-only distribution in the case of the $\pm 1/2\sigma$ bands on the expected limits. A plot of the scan over μ is shown in Figure 4.23.

Figures 4.24 and 4.25 show the exclusion limits as a function of signal mass, obtained using the toy MC and asymptotic methods respectively. Here the eigenvector decomposition of the JES and b-tagging uncertainties have not been used and the overall shifts have been used instead. This is to speed up the computing time of the toy MC generation. It can be seen that the two methods produce results in good agreement with each other.

4.8.3. Treatment of Uncertainties

The following uncertainties are currently taken into account in the calculation of the limits:

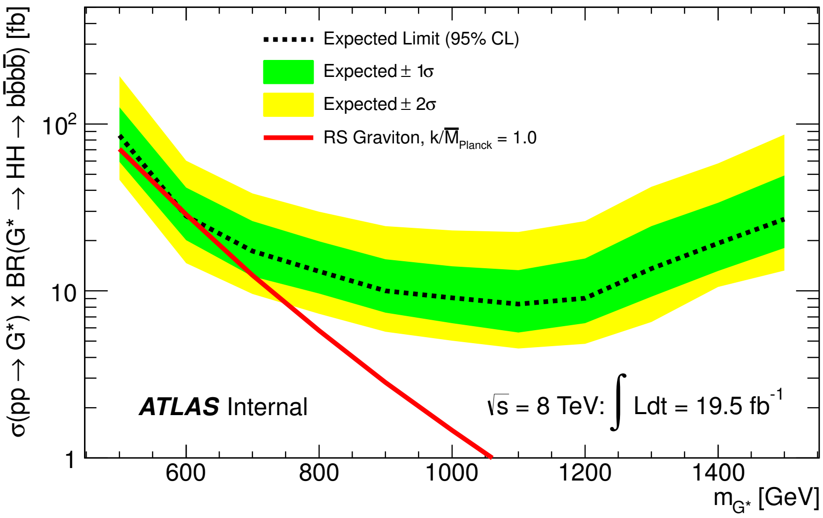

Figure 4.24.: The expected upper limits from toy MC as a function of signal mass. Here the eigenvector decomposition of the JES and b-tagging uncertainties have not been used and the overall shifts have been used instead.

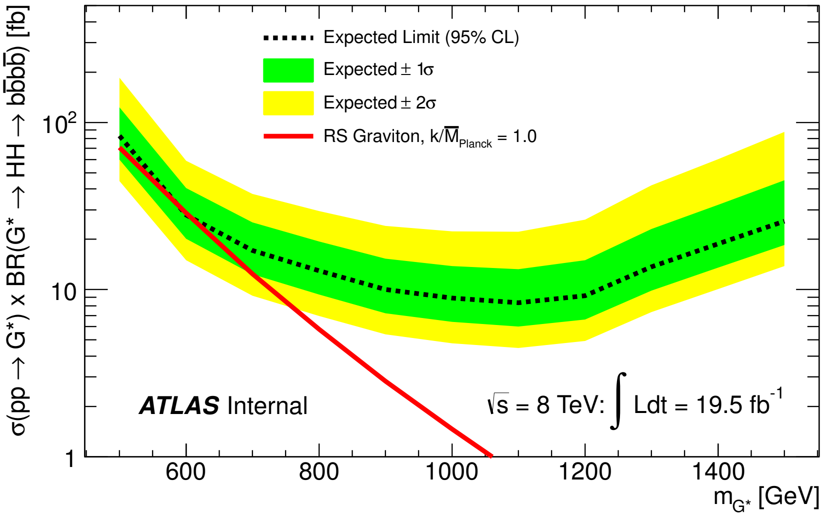

Figure 4.25.: The expected upper limits using the asymptotic method as a function of signal mass. Here the eigenvector decomposition of the JES and b-tagging uncertainties have not been used and the overall shifts have been used instead.

- luminosity: ±2.8%.
- QCD modelling normalisation: ±5%. See section 4.5.2.
- QCD modelling shape. See section 4.5.3.
- $t\bar{t}$ normalisation: ±59%/522%. See section 4.4.3
- $t\bar{t}$ modelling shape. See section 4.5.5.
- b-tagging efficiency modelling in MC. See section 4.5.1.
- Jet Energy Resolution modelling in MC. See section 4.5.1.
- Jet Energy Scale modelling in MC. See section 4.5.1.

These uncertainties are all treated as uncorrelated with one another. The luminosity is applied to signal and Z+jets MC. The b-tagging and jet energy uncertainties are applied to the signal MC. For the jet energy resolution systematic, only the smearing out is applied, there is no consideration for the case when the JER is underestimated and so this is a conservative treatment of that systematic. For the uncertainty on the b-tagging efficiency, the eigenvector decomposition of that systematic is used. Since the impact on the signal efficiency is found to be dominated by some of the eigenvector components, only components which make $> 1\%$ difference to the signal efficiency are considered. Table A.1 shows that these are components 6-9 inclusive and the high-p_{T} component. For the JES components, table A.2 shows that the effect is split fairly evenly between the components and so all eigenvectors are used as nuisance parameters in the limit setting.

The systematics are treated as constraint terms in the profile likelihood. Specifically Gaussian constraint terms are used, with a linear interpolation between the values of the nominal and $\pm 1\sigma$ histograms for the shape systematics and an exponential interpolation for the normalisation systematics, which is equivalent to a log-normal constraint term with a linear interpolation between the histograms. The JES and JER shifts are treated as shape systematics. The b-tagging eigenvectors are treated as normalisation systematics, since their impact on the shape of the $\mathrm{m_{4j}}$ distribution is negligible and they are also large and so better described by the effective log-normal constraint term than a Gaussian one.

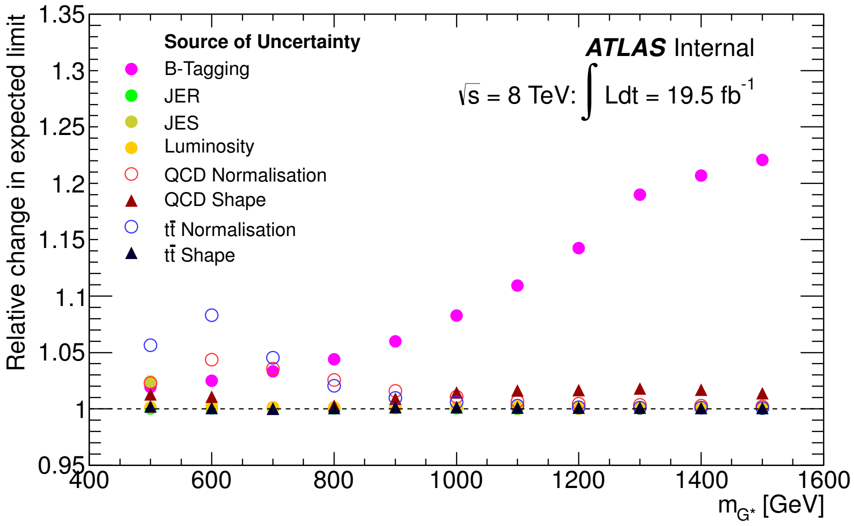

Figure 4.26.: A plot showing the impact of the different uncertainty sources on the expected exclusion limit.

Figure 4.26 shows the ratio of the expected limit, calculated including the specified uncertainty, divided by the limit calculated without taking into account any of the systematic uncertainties. It can be seen here that the b-tagging efficiency uncertainties dominate at the higher signal masses, where the jets are at very high p_{T}. At the lower masses no one component dominates, the uncertainties on the normalisations of the background models are the most significant.

4.8.4. Expected Limits

Figure 4.27 shows the expected exclusion limits, for the HH channel, taking into account all the sources of uncertainty listed in Section 4.8.3. Figure 4.28 shows the same plot for the ZZ channel, which has substantially lower sensitivity to this signal model.

In the ZZ channel, any signal contribution from the $G^* \to ZZ \to c\bar{c}b\bar{b}$ decay is neglected. This contribution is roughly estimated to be ~13% of $G^* \to ZZ \to b\bar{b}b\bar{b}$ (assuming a c-jet mis-tagging efficiency of 0.2 and a b-jet tagging efficiency of 0.7). Therefore the expected upper limits presented in Figure 4.28 are slightly overestimated, and would likely improve by ~10% if $G^* \to ZZ \to c\bar{c}b\bar{b}$ were taken into account. However a 10% improvement would not alter the fact that this ZZ channel is not competitive with the $ZZ \to llqq$ analysis [81]. Combining the HH

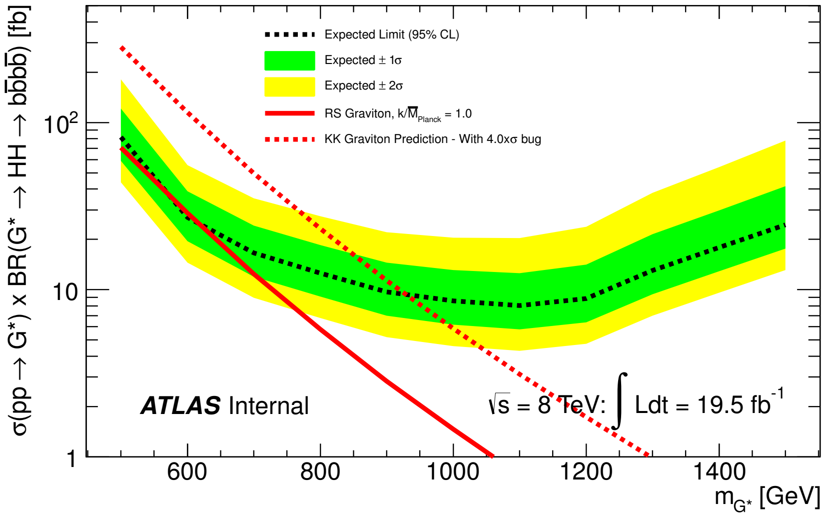

Figure 4.27.: The expected exclusion limits, in the HH channel, calculated including systematic uncertainties. The dotted red line shows the RS graviton prediction before the factor 0.25 correction, for comparison with previous searches based on this model which suffered from this bug e.g. [81].

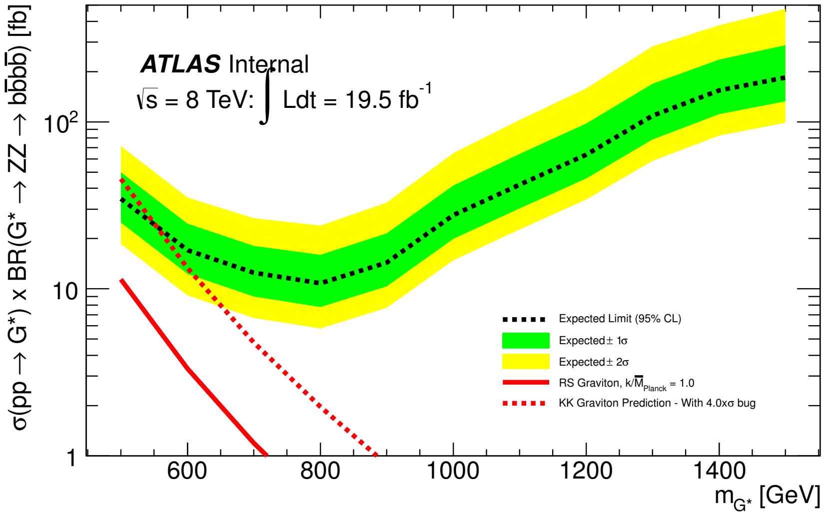

Figure 4.28.: The expected exclusion limits, in the ZZ channel, calculated including systematic uncertainties. The dotted red line shows the RS graviton prediction before the factor 0.25 correction, for comparison with previous searches (e.g. [81]) based on this model which suffered from this bug.

and ZZ channels leads to a gain in sensitivity of up to only 7%, for this graviton model, compared with using the HH channel alone.

4.9. Results

4.9.1. Unblinded Data and Search Results

Table 4.8 compares the predicted background with the total number of events in the HH and ZZ signal regions. The data in the HH region is consistent with the background prediction within 1σ and in the ZZ region, the data and background prediction are consistent within 1.3σ.

Figures 4.29 and 4.30 compare the $\mathrm{m_{4j}}$ distributions in the data to the background prediction in the HH and ZZ signal regions. The systematic uncertainties on the background shapes and normalisations are not shown. The agreement with the background-only model, even without taking into account the systematic uncertainties, is fairly good. There are no visible excesses above the background model.

The results of a more sensitive analysis in the ZZ region [81], which uses the $ZZ \rightarrow llqq$ channel, excludes a signal in that region. Hence, the consistency of the background model with the observed data in the ZZ region, is a validation of the background modeling procedure, since it is not expected to see a signal there.

The background-only hypothesis is tested against the observed data following the procedure outlined in Section 4.7. Figure 4.31 shows the local p_0 values across the

Sample	HH Region	ZZ Region
QCD	108.7 ± 5.4	139.8 ± 7.0
$t\bar{t}$	10.5 ± 5.0	1.7 ± 2.4
Z+jets	0.7 ± 0.2	6.1 ± 0.7
Total Bkgd	119.9 ± 7.4	147.6 ± 7.4
Data	114 (± 10.7)	130 (± 11.4)

Table 4.8.: The number of predicted background events in each of the HH and ZZ signal regions and the number of events in the 2012 data. The uncertainty on the Z+jets background is statistical only. The uncertainties on the $t\bar{t}$ and QCD backgrounds are the full uncertainties on the background modelling methods, explained in Section 4.4.3 for the $t\bar{t}$ and Section 4.5.2 for the QCD. The statistical uncertainties on the number of events in the data are also shown.

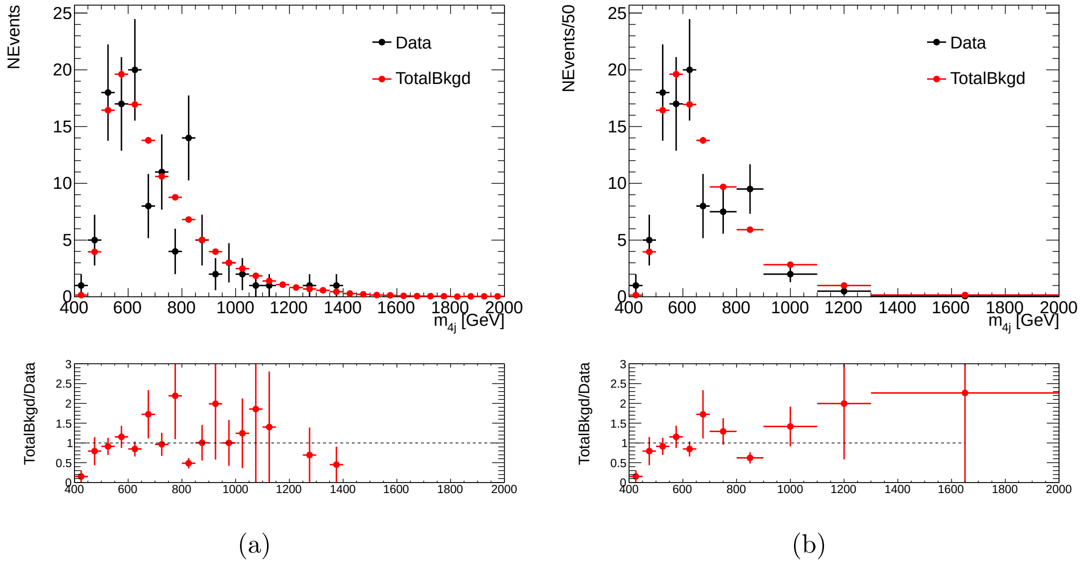

(a) (b)

Figure 4.29.: Comparison of the predicted background and data in the m_{4j} distribution of the HH signal region. Shown with (a) bin widths of 50 GeV and (b) variable bin widths.

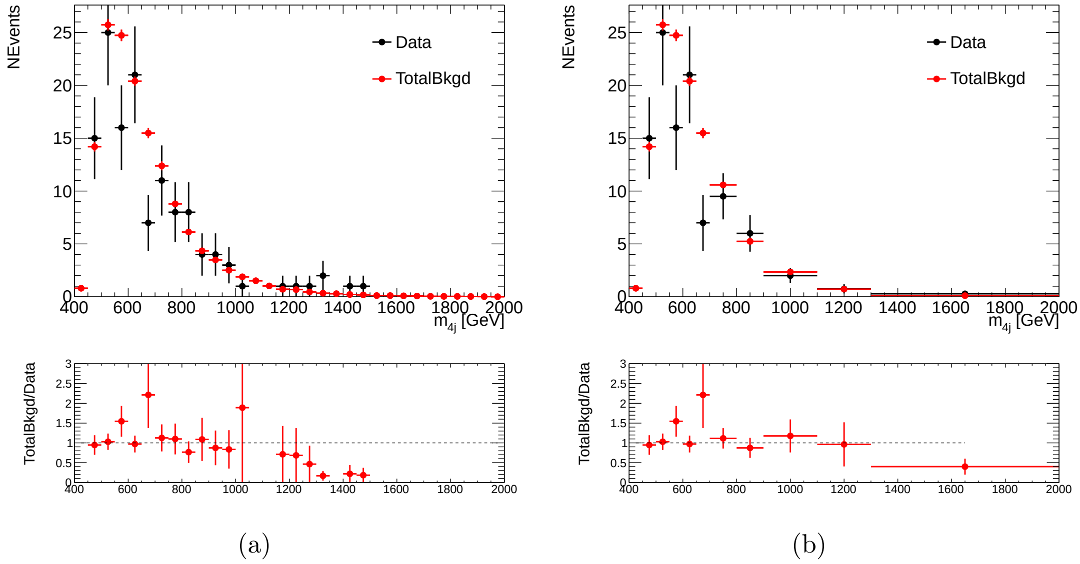

(a) (b)

Figure 4.30.: Comparison of the predicted background and data in the m_{4j} distribution of the ZZ signal region. Shown with (a) bin widths of 50 GeV and (b) variable bin widths.

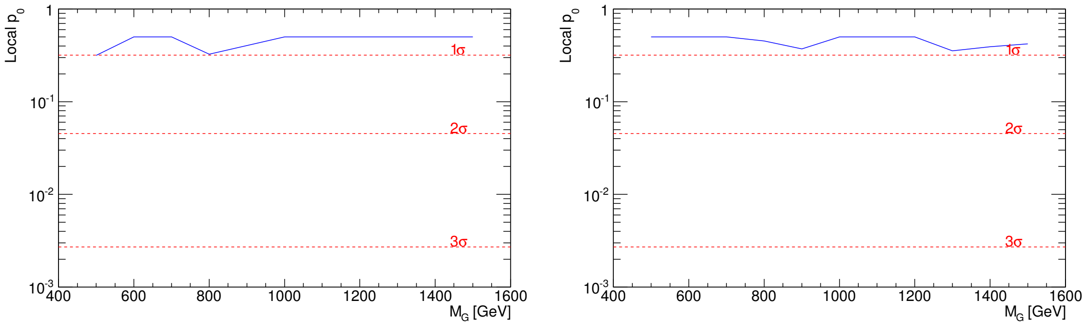

(a) HH Channel (b) ZZ Channel

Figure 4.31.: The local p_0 value (see Section 4.7) as a function of the graviton signal mass in the HH and ZZ channels.

signal mass range, in the HH and ZZ channels. There is no statistically significant excess observed. Table 4.9 shows the best fit values of the signal normalisation for each signal mass point. They are all consistent with 0.

Table 4.10 lists the pulls of the background nuisance parameters, in the maximum likelihood where μ is set to 0. It is seen that the ML values are not pulled very far from their mean values and the limited statistics of the data means that the improvement in the constraints on them is very small (i.e. the error on the pulls are close to 1σ, the original uncertainty on the parameter). Table A.3, shows the pulls of the systematics in the case where the maximum likelihood has been obtained, fixing μ to be the value at the observed upper limit, in the HH channel. It is seen that there are no large pulls of any of these parameters and that there is no significant change in the constraints on them.

4.9.2. Observed Limits and Exclusion

The observed data is used to set limits on the graviton signal model following the procedure described in Section 4.8. Figure 4.32 shows the expected and observed upper limits on σ x BR($G^* \to$HH$\to b\bar{b}b\bar{b}$) in the HH channel. The observed limit is consistent within uncertainties with the expected limit. The RS graviton is excluded at 95% confidence level in the mass range 590 - 710 GeV.

$\mathrm{m_{G^*}}$ [GeV]	$\hat{\mu}$
500	0.25 ± 0.53
600	0.00 ± 1.31
700	0.00 ± 0.29
800	0.45 ± 0.97
900	0.40 ± 1.48
1000	0.00 ± 1.96
1100	0.00 ± 1.76
1200	0.00 ± 2.50
1300	0.00 ± 10.04
1400	0.04 ± 63.32
1500	0.00 ± 68.42

Table 4.9.: The maximum likelihood values of the signal normalisation, $\hat{\mu}$.

Nuisance Parameter	Pull Value (HH Region)	Pull Value (ZZ Region)
QCD Normalisation	-0.22 ± 0.91 σ	-0.6 ± 0.86 σ
QCD Shape	-0.52 ± 0.92 σ	0.35 ± 0.88 σ
$t\bar{t}$ Normalisation	-0.01 ± 0.86 σ	-0.22 ± 0.96 σ
$t\bar{t}$ Shape	0.17 ± 0.98 σ	0.00 ± 0.99 σ

Table 4.10.: The pulls of the background nuisance parameters in the conditional maximum likelihood where μ is set to 0; $L(0, \hat{\hat{\boldsymbol{\theta}}})$.

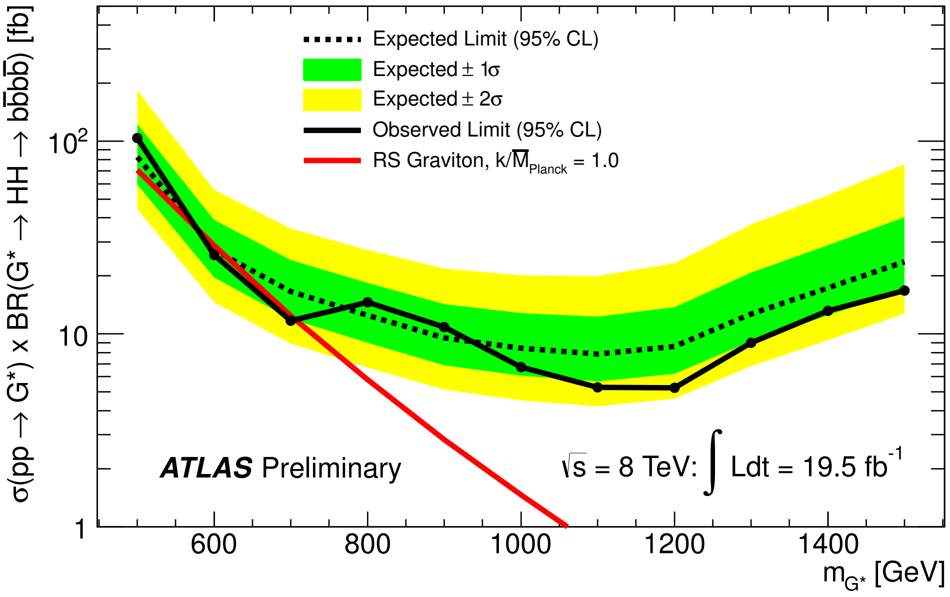

Figure 4.32.: The expected and observed upper limits on the RS graviton cross section × branching ratio in the HH channel.

Figure 4.33 shows the expected and observed upper limits on σ x BR$(G^* \to ZZ)$ in the $ZZ \to b\bar{b}b\bar{b}$ channel. The observed limit is consistent with the expected limit. Here, the branching ratio of $Z \to b\bar{b}$ has been unfolded using the PDG value of 15.1% [87]. The uncertainty on this branching ratio is $<$ 1% and so is ignored.

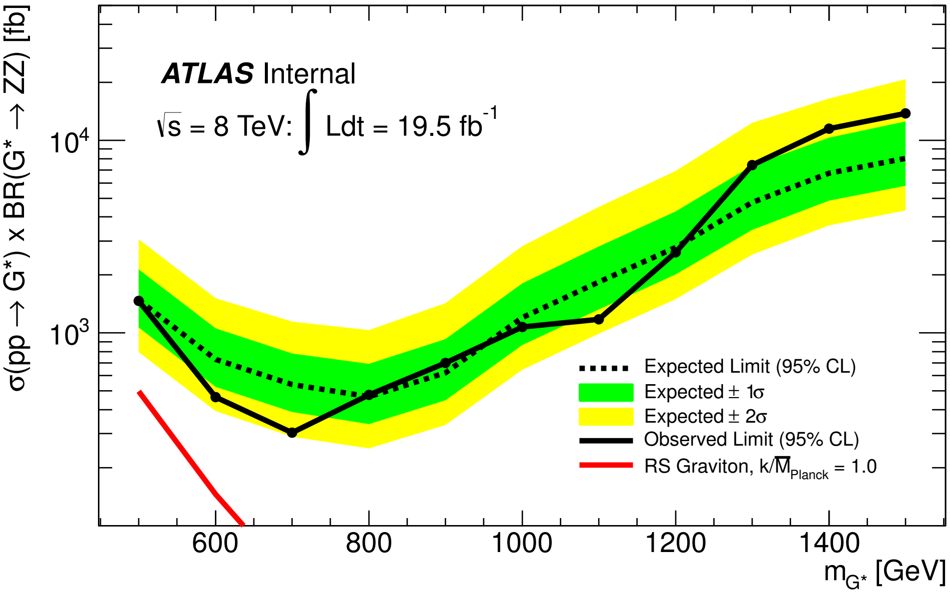

Figure 4.33.: The expected and observed upper limits on the RS graviton cross section × branching ratio in the ZZ channel.

Chapter 5.

Conclusions

The search for high transverse momentum objects decaying to b-quarks will be a key part of the physics program of the LHC in run-2. In particular these searches in all-hadronic final states are amongst the most challenging discovery channels at the LHC. The key difficulties come from the large QCD background. Firstly this makes efficient triggering very difficult due to the high rate of QCD events. Secondly, these channels tend to have a low signal-to-background ratio due to the relative strength of the strong force. Lastly these backgrounds can be difficult to model using MC, with often significant disagreement between the predictions of individual generators.

The measurement of boosted $Z \to b\bar{b}$ is an important validation of these searches in challenging all-hadronic final states. The search relies on b-jet triggers, which use b-tagging algorithms to preferentially select jets containing B-hadrons, in order to achieve high signal efficiency in the presence of the enormous rate of high p_{T} jet events that occur at the LHC. A data-driven approach is used to model the QCD background, since LO MC is found to be inadequate in its modelling of the kinematics of this background. Variables that make use of the differences between the electroweak produced signal and the QCD produced background are found and used to improve the low signal-to-background ratio and obtain a signal depleted region of data for use as the background model. The measured cross section is found to be in good agreement with the Standard Model prediction obtained using next-to-leading-order plus parton-shower MC generators. This observation opens the door for the $Z \to b\bar{b}$ peak to be used as a standard candle in run-2 of the LHC, where the increase in integrated luminosity should open up new possibilities for its use. One possibility is that the $Z \to b\bar{b}$ peak could be used as a testbed of techniques to improve the $b\bar{b}$ mass resolution and potentially to assess systematic uncertainties associated with b-jets. This has the potential to be extremely beneficial to the relevant searches, in particular the $H \to b\bar{b}$ search.

A search is performed for a di-Higgs resonance in the 500-1500 GeV mass range, in the $b\bar{b}b\bar{b}$ final state. This is a new search channel, which uses the known mass of the recently discovered Higgs boson to make a very general search for new physics. Similarly to the $Z \to b\bar{b}$ measurement, this search is reliant on b-jet triggers and uses a data-driven model for the QCD background. It is the first search for di-Higgs resonances performed in this signal mass range and is sensitive to cross section × branching ratios down to a few fb. No significant deviation from the background prediction is observed. Upper limits are set on the first massive graviton excitation in the Randal-Sundrum model, which exclude the prediction of the model, at 95% confidence level over the signal mass range 590 - 710 GeV for the parameter choice of $k/\bar{M}_{\mathrm{Pl}} = 1$. In the future, the search could be extended to higher signal masses with the use of jet substructure techniques and will obtain significantly improved sensitivity with the increase in collision energy and integrated luminosity expected for run-2. There is also significant potential for improvements in sensitivity at the lower range of signal masses. It is also possible to expand the search to non-resonant di-Higgs production, which will be of particular interest in both run-2 and the upgraded high-luminosity-LHC.

Appendix A.

Tables

Variation	RS Graviton, m_{G^*} [GeV]										
	500	600	700	800	900	1000	1100	1200	1300	1400	1500
bTagSF0 Up	-0.11	-0.08	-0.06	-0.07	-0.05	-0.04	-0.02	-0.05	-0.05	-0.06	-0.04
bTagSF0 Down	0.11	0.08	0.06	0.07	0.05	0.04	0.02	0.05	0.05	0.06	0.04
bTagSF1 Up	0.20	0.21	0.16	0.14	0.11	0.08	0.06	0.06	0.06	0.06	0.03
bTagSF1 Down	-0.20	-0.21	-0.16	-0.14	-0.11	-0.08	-0.06	-0.06	-0.06	-0.06	-0.03
bTagSF2 Up	0.01	0.05	0.05	0.02	0.01	-0.02	-0.04	-0.06	-0.09	-0.11	-0.11
bTagSF2 Down	-0.01	-0.05	-0.05	-0.02	-0.01	0.02	0.04	0.06	0.09	0.11	0.12
bTagSF3 Up	0.30	0.27	0.20	0.13	0.06	0.02	-0.03	-0.03	-0.05	-0.04	-0.13
bTagSF3 Down	-0.30	-0.26	-0.20	-0.13	-0.06	-0.02	0.03	0.03	0.05	0.04	0.13
bTagSF4 Up	0.24	0.21	0.15	0.16	0.18	0.19	0.19	0.19	0.21	0.19	0.20
bTagSF4 Down	-0.24	-0.21	-0.15	-0.16	-0.18	-0.18	-0.19	-0.19	-0.21	-0.19	-0.20
bTagSF5 Up	-0.38	-0.36	-0.32	-0.33	-0.34	-0.35	-0.36	-0.37	-0.40	-0.39	-0.38
bTagSF5 Down	0.38	0.36	0.32	0.33	0.34	0.35	0.36	0.37	0.40	0.39	0.38
bTagSF6 Up	1.84	1.75	1.38	0.938	0.638	0.391	0.189	0.0151	-0.107	-0.122	-0.209
bTagSF6 Down	-1.83	-1.73	-1.35	-0.93	-0.63	-0.39	-0.19	-0.02	0.11	0.12	0.21
bTagSF7 Up	-2.53	-1.59	-0.118	1.04	1.91	2.5	2.9	3.04	2.91	2.69	2.72
bTagSF7 Down	2.58	1.6	0.09	-1.08	-1.93	-2.51	-2.88	-3.02	-2.9	-2.69	-2.72
bTagSF8 Up	2.73	3.7	5.23	6.42	7.28	7.88	8.29	8.42	8.26	8.04	7.98
bTagSF8 Down	-2.68	-3.61	-5.06	-6.17	-6.95	-7.49	-7.84	-7.96	-7.83	-7.63	-7.58
bTagSF9 Up	-9.56	-10.5	-12	-13	-13.8	-14.3	-14.7	-14.8	-14.6	-14.4	-14.4
bTagSF9 Down	10.3	11.4	13.1	14.4	15.4	16	16.4	16.5	16.3	16.1	16.1
bTagSFHighPt Up	0.19	0.502	1.98	5.39	9.95	14.7	19.6	24.9	31.8	34.7	37.5
bTagSFHighPt Down	-0.19	-0.488	-1.95	-5.23	-9.47	-13.6	-17.8	-22	-26.9	-28.6	-30.4

Table A.1.: A table showing the percentage change in the predicted number of events passing the full hh cuts when applying the individual b-tag scale factor uncertainty eigenvector components for each of the signal MC masses.

	RS Graviton, m_{G^*} [GeV]										
Variation	500	600	700	800	900	1000	1100	1200	1300	1400	1500
JESNP1Up	3.04	1.02	0.24	-0.10	-0.56	-0.09	-0.36	-0.67	-1.35	-1.08	-1.19
JESNP1Down	-4.9	-0.93	-0.72	-0.46	-0.21	-0.13	0.36	0.15	0.41	0.40	-0.03
JESNP2Up	-7.46	-1.87	-1.52	-0.94	-0.48	-0.52	0.19	-0.04	-0.01	-0.72	-1.08
JESNP2Down	5	1.76	0.61	-0.12	-0.26	0.19	0.06	-0.39	-1.24	-0.53	-0.72
JESNP3Up	1.67	0.88	0.45	0.65	0.51	0.55	0.46	0.22	0.33	0.49	0.77
JESNP3Down	-2.65	-1.13	-0.96	-0.53	-0.56	-0.47	-0.20	-0.71	-0.75	-0.63	-1.15
JESNP4Up	0.01	0.04	-0.35	-0.09	-0.38	-0.02	-0.09	-0.32	-0.51	-0.22	-0.96
JESNP4Down	-1.28	0.02	0.15	0.09	0.18	0.35	-0.05	0.05	0.46	0.21	0.39
JESNP5Up	-0.89	-0.15	-0.021	0.06	-0.00	0.04	-0.00	-0.083	0.05	-0.13	0.19
JESNP5Down	0.00	0.07	-0.14	-0.00	-0.01	-0.04	0.13	-0.05	-0.28	-0.21	-0.19
JESNP6Up	0.98	0.29	0.11	0.14	0.08	0.06	0.04	-0.35	-0.14	-0.21	-0.17
JESNP6Down	-1.18	-0.26	-0.22	-0.00	-0.05	-0.06	0.06	-0.03	0.05	-0.07	-0.19
JESBJetUp	8.06	1.95	0.77	0.33	-0.31	0.23	-0.32	-1.00	-1.41	-1.21	-0.81
JESBJetDown	-9.22	-2.31	-2.01	-1.15	-0.96	-0.60	-0.05	-0.21	0.03	0.17	-1.39
JESForwardModelUp	5.15	1.50	0.36	0.45	-0.13	-0.45	-0.27	-0.63	-0.67	-1.28	-0.32
JESForwardModelDown	-5.6	-2.27	-1.33	-0.88	-0.77	-0.49	0.01	0.29	-0.62	-0.38	-0.53
JESForwardStatUp	1.09	0.51	0.28	0.26	0.10	0.24	-0.07	-0.29	-0.14	-0.00	-0.28
JESForwardStatDown	-1.76	-0.40	-0.36	-0.09	-0.20	-0.13	0.01	0.05	-0.01	-0.01	-0.39
JESMuUp	0.19	0.18	-0.02	0.02	0.06	0.10	0.09	0.06	-0.14	-0.21	-0.09
JESMuDown	-0.39	-0.32	-0.03	-0.04	0.00	-0.12	0.04	-0.11	-0.10	0.00	-0.39
JESNPVUp	1.15	0.28	0.01	0.08	-0.01	0.37	0.21	-0.05	-0.14	-0.76	-0.09
JESNPVDown	-0.78	-0.39	-0.40	-0.27	-0.29	0.14	-0.03	-0.17	-0.24	0.69	-0.39
JESRhoUp	1.78	0.74	0.31	0.40	0.20	0.33	0.18	-0.12	-0.32	0.08	-0.19
JESRhoDown	-2.47	-0.83	-0.77	-0.40	-0.35	-0.09	0.01	-0.20	-0.29	-0.14	-0.68
JESPileUpPtUp	-0.33	-0.20	-0.05	0.05	-0.27	0.12	-0.16	-0.27	-0.34	-0.91	-0.60
JESPileUpPtDown	0.20	0.49	-0.22	-0.14	-0.22	0.15	-0.00	-0.10	-0.22	0.50	-0.47
JESFlavCompUp	-0.59	-0.46	-0.45	-0.60	-0.43	-0.61	-0.33	-0.20	-0.69	-0.15	-0.09
JESFlavCompDown	0.40	0.39	0.36	0.47	0.48	0.55	0.67	0.40	0.10	0.49	0.48
JESFlavRespUp	-0.29	-0.28	-0.40	-0.32	-0.25	-0.38	-0.12	-0.14	-0.60	-0.01	-0.08
JESFlavRespDown	0.10	0.28	0.10	0.28	0.32	0.26	0.42	0.19	0.05	0.15	0.29

Table A.2.: A table showing the percentage change in the predicted number of events passing the full analysis selection, in the hh signal region, when applying the individual jet energy scale uncertainty eigenvector components for each of the signal masses and fully hadronic $t\bar{t}$ samples.

Systematic	500	600	700	800	900	1000	1100	1200	1300	1400	1500
BTagSF6	-0.07 ± 0.99	-0.06 ± 0.99	-0.04 ± 0.99	-0.04 ± 0.99	-0.02 ± 0.99	-0.01 ± 0.99	-0.00 ± 0.99	0.00 ± 0.99	0.01 ± 0.99	0.01 ± 0.99	0.00 ± 0.99
BTagSF7	0.11 ± 0.99	0.06 ± 0.99	0.01 ± 0.99	-0.03 ± 0.99	-0.09 ± 0.99	-0.09 ± 0.99	-0.10 ± 0.99	-0.10 ± 0.99	-0.10 ± 0.99	-0.09 ± 0.99	-0.04 ± 0.99
BTagSF8	-0.10 ± 0.99	-0.13 ± 0.99	-0.16 ± 0.99	-0.24 ± 0.98	-0.28 ± 0.98	-0.25 ± 0.98	-0.25 ± 0.98	-0.24 ± 0.98	-0.26 ± 0.98	-0.26 ± 0.98	-0.11 ± 0.99
BTagSF9	0.35 ± 0.96	0.37 ± 0.97	0.37 ± 0.97	0.51 ± 0.96	0.51 ± 0.96	0.46 ± 0.96	0.45 ± 0.97	0.44 ± 0.97	0.47 ± 0.97	0.48 ± 0.97	0.21 ± 0.97
BTagSFHighPt	-0.00 ± 0.99	-0.00 ± 0.99	-0.04 ± 0.99	-0.16 ± 0.99	-0.42 ± 0.97	-0.48 ± 0.97	-0.59 ± 0.98	-0.67 ± 1.00	-0.87 ± 0.99	-1.00 ± 0.93	-0.47 ± 0.96
JER	0.03 ± 1.04	0.10 ± 1.15	0.15 ± 1.18	0.03 ± 1.05	0.13 ± 1.18	0.04 ± 1.06	0.03 ± 1.04	0.04 ± 1.07	0.08 ± 1.12	0.09 ± 1.15	0.04 ± 1.06
JESBJet	-0.64 ± 0.91	-0.03 ± 0.96	-0.09 ± 1.17	0.30 ± 1.00	-0.28 ± 1.11	-0.07 ± 1.07	-0.08 ± 1.01	0.01 ± 1.02	0.07 ± 1.05	-0.05 ± 1.07	-0.06 ± 1.08
JESFlavComp	0.02 ± 0.99	0.01 ± 0.99	0.01 ± 1.00	0.00 ± 0.98	0.03 ± 1.01	0.02 ± 0.99	0.01 ± 0.98	0.01 ± 0.99	0.01 ± 1.00	0.00 ± 0.99	0.01 ± 0.98
JESFlavResp	0.01 ± 0.99	0.01 ± 0.99	0.01 ± 1.01	0.00 ± 0.99	0.01 ± 1.01	0.01 ± 0.99	0.00 ± 0.98	0.00 ± 0.99	0.01 ± 1.00	0.00 ± 0.99	0.00 ± 0.98
JESForwardModel	-0.38 ± 1.03	-0.02 ± 0.98	-0.07 ± 1.11	0.14 ± 1.03	-0.20 ± 1.07	-0.05 ± 1.07	-0.05 ± 1.02	0.03 ± 0.98	0.02 ± 1.00	-0.08 ± 1.15	-0.04 ± 1.02
JESForwardStat	-0.01 ± 0.96	-0.01 ± 0.97	-0.00 ± 1.01	0.05 ± 0.99	-0.05 ± 1.03	-0.01 ± 1.01	-0.01 ± 0.99	0.01 ± 1.01	0.00 ± 1.00	-0.03 ± 1.00	-0.01 ± 0.99
JESMu	0.03 ± 0.96	-0.01 ± 0.99	-0.00 ± 1.01	0.02 ± 0.98	-0.00 ± 0.99	-0.01 ± 1.00	-0.00 ± 0.94	-0.00 ± 1.01	0.01 ± 1.01	0.01 ± 1.00	-0.00 ± 0.95
JESNP1	-0.19 ± 1.08	0.02 ± 0.94	0.00 ± 1.08	0.20 ± 1.00	-0.10 ± 1.03	-0.05 ± 1.05	-0.06 ± 0.99	0.01 ± 0.96	0.06 ± 1.04	-0.03 ± 1.06	-0.04 ± 1.09
JESNP2	0.54 ± 0.98	0.02 ± 0.94	0.05 ± 1.13	-0.23 ± 1.03	0.15 ± 1.04	0.06 ± 1.04	0.06 ± 1.00	-0.00 ± 0.93	-0.00 ± 1.07	0.06 ± 1.04	0.05 ± 1.03
JESNP3	-0.02 ± 1.01	-0.03 ± 0.96	-0.01 ± 1.00	-0.03 ± 0.98	-0.00 ± 0.95	-0.01 ± 1.00	-0.00 ± 0.95	-0.02 ± 1.01	-0.03 ± 1.02	-0.01 ± 0.99	-0.02 ± 1.00
JESNP4	-0.08 ± 1.00	0.00 ± 0.99	0.00 ± 1.01	0.06 ± 0.99	-0.02 ± 1.03	-0.01 ± 1.00	-0.01 ± 1.00	0.00 ± 1.01	0.02 ± 1.00	-0.01 ± 0.96	0.00 ± 0.95
JESNP5	0.00 ± 1.05	0.00 ± 0.98	-0.01 ± 1.00	-0.03 ± 0.98	-0.01 ± 0.99	0.00 ± 1.00	-0.00 ± 0.96	0.00 ± 1.00	0.00 ± 1.01	-0.00 ± 0.94	-0.01 ± 0.99
JESNP6	-0.02 ± 1.03	-0.01 ± 0.98	-0.00 ± 1.00	0.05 ± 1.00	-0.02 ± 1.00	-0.01 ± 1.00	-0.00 ± 0.95	0.01 ± 1.02	-0.00 ± 1.01	-0.03 ± 0.99	-0.01 ± 0.97
JESNPV	-0.07 ± 1.06	0.00 ± 0.98	0.01 ± 1.01	0.02 ± 0.99	-0.04 ± 1.03	-0.00 ± 1.00	-0.01 ± 0.98	-0.01 ± 1.00	0.01 ± 1.00	0.05 ± 0.97	-0.00 ± 0.96
JESPileUpPt	0.05 ± 0.98	0.02 ± 0.93	0.00 ± 1.06	-0.03 ± 1.07	-0.03 ± 1.05	0.01 ± 1.01	-0.00 ± 0.95	-0.00 ± 0.98	0.01 ± 1.07	0.07 ± 1.00	-0.00 ± 0.95
JESRho	-0.05 ± 1.01	-0.01 ± 0.96	0.00 ± 1.02	0.04 ± 1.00	-0.06 ± 1.05	-0.01 ± 1.01	-0.01 ± 0.99	0.01 ± 1.01	0.00 ± 1.01	-0.03 ± 0.98	-0.01 ± 1.01
qcdNormSyst	-0.57 ± 0.90	-0.65 ± 0.90	-0.50 ± 0.91	-0.63 ± 0.91	-0.53 ± 0.91	-0.38 ± 0.91	-0.31 ± 0.91	-0.28 ± 0.91	-0.29 ± 0.91	-0.29 ± 0.91	-0.26 ± 0.91
qcdShapeSyst	-0.16 ± 0.95	-0.26 ± 0.94	-0.53 ± 0.93	-0.72 ± 0.92	-0.77 ± 0.92	-0.72 ± 0.92	-0.67 ± 0.92	-0.63 ± 0.93	-0.67 ± 0.93	-0.66 ± 0.93	-0.60 ± 0.93
ttbarNormSyst	-0.52 ± 0.84	-0.46 ± 0.85	-0.23 ± 0.89	-0.25 ± 0.89	-0.17 ± 0.90	-0.08 ± 0.90	-0.03 ± 0.90	-0.01 ± 0.90	-0.02 ± 0.90	-0.02 ± 0.90	-0.00 ± 0.90
ttbarShapeSyst	-0.00 ± 0.99	0.08 ± 1.01	0.18 ± 1.03	0.25 ± 1.05	0.26 ± 1.05	0.24 ± 1.04	0.21 ± 1.04	0.20 ± 1.03	0.21 ± 1.04	0.21 ± 1.04	0.19 ± 1.03

Table A.3.: The pull values of each of the systematics, for each of the signal mass points, in the conditional maximum likelihood, where the signal normalisation is fixed to its value at the observed upper limit.

Bibliography

[1] ATLAS Collaboration, G. Aad et al., *Measurement of the cross section of high transverse momentum* $Z \to b\bar{b}$ *production in proton–proton collisions at* $\sqrt{s} = 8$ *TeV with the ATLAS Detector*, `arXiv:1404.7042 [hep-ex]`.

[2] B. Cooper, N. Konstantinidis, L. Lambourne, and D. Wardrope, *Boosted* $hh \to b\bar{b}b\bar{b}$*: A new topology in searches for TeV-scale resonances at the LHC*, Phys.Rev. **D88** 114005.

[3] ATLAS Collaboration, G. Aad et al., *A search for resonant Higgs-pair production in the* $b\bar{b}b\bar{b}$ *final state in pp collisions at* $\sqrt{s} = 8$ *TeV*, Tech. Rep. ATLAS-CONF-2014-005, CERN, Geneva, Mar, 2014.

[4] M. Gaillard, P. Grannis, and F. Sciulli, *The Standard Model of Particle Physics*, in *More Things in Heaven and Earth*, B. Bederson, ed., pp. 161–187. Springer New York, 1999.

[5] F. Englert and R. Brout, *Broken Symmetry and the Mass of Gauge Vector Mesons*, Phys. Rev. Lett. **13** (Aug, 1964) 321–323.

[6] P. W. Higgs, *Broken Symmetries and the Masses of Gauge Bosons*, Phys. Rev. Lett. **13** (Oct, 1964) 508–509.

[7] E. Noether, *Invariant variation problems*, Transport Theory and Statistical Physics **1** (1971) no. 3, 186–207.

[8] CDF Collaboration, F. Abe et al., *Observation of Top Quark Production in* $p\bar{p}$ *Collisions with the Collider Detector at Fermilab*, Phys. Rev. Lett. **74** (Apr, 1995) 2626–2631.

[9] DØ Collaboration, S. Abachi et al., *Observation of the Top Quark*, Phys. Rev. Lett. **74** (Apr, 1995) 2632–2637.

[10] ATLAS Collaboration, G. Aad et al., *Observation of a new particle in the search for the Standard Model Higgs boson with the ATLAS detector at the LHC*, Physics Letters B **716** (2012) no. 1, 1 – 29.

[11] CMS Collaboration, S. Chatrchyan et al., *Observation of a new boson at a mass of 125 GeV with the CMS experiment at the LHC*, Physics Letters B **716** (2012) no. 1, 30 – 61.

[12] Planck Collaboration, P. Ade et al., *Planck 2013 results. I. Overview of products and scientific results*, `arXiv:1303.5062 [astro-ph.CO]`.

[13] S. P. Martin, *A Supersymmetry primer*, `arXiv:hep-ph/9709356 [hep-ph]`.

[14] L. Randall and R. Sundrum, *A Large mass hierarchy from a small extra dimension*, Phys.Rev.Lett. **83** (1999) 3370–3373.

[15] L. Fitzpatrick, J. Kaplan, L. Randall, and L.-T. Wang, *Searching for the Kaluza-Klein graviton in bulk RS models*, JHEP **2007** (2007) no. 09, 013.

[16] H1 and ZEUS Collaboration, F. Aaron et al., *Combined measurement and QCD analysis of the inclusive* $e^{\pm}p$ *scattering cross sections at HERA*, Journal of High Energy Physics **2010** (2010) no. 1, 1–63.

[17] CDF Collaboration, T. Affolder et al., *Measurement of the inclusive jet cross section in* $p\bar{p}$ *collisions at* $\sqrt{s} = 1.8$ *TeV*, Phys. Rev. D **64** (Jun, 2001) 032001.

[18] D0 Collaboration, B. Abbott et al., *Inclusive Jet Cross Section in* $p\bar{p}$ *Collisions at* $\sqrt{s} = 1.8$ *TeV*, Phys. Rev. Lett. **82** (Mar, 1999) 2451–2456.

[19] X. Artru and G. Mennessier, *String model and multiproduction*, Nuclear Physics B **70** (1974) no. 1, 93 – 115.

[20] R. D. Field and S. Wolfram, *A QCD model for* e^+e^- *annihilation*, Nuclear Physics B **213** (1983) no. 1, 65 – 84.

[21] A. Buckley, J. Butterworth, S. Gieseke, D. Grellscheid, S. Höche, H. Hoeth, F. Krauss, L. Lönnblad, E. Nurse, P. Richardson, S. Schumann, M. H. Seymour, T. Sjöstrand, P. Skands, and B. Webber, *General-purpose event generators for LHC physics*, Physics Reports **504** (2011) no. 5, 145 – 233.

[22] M. Bahr, S. Gieseke, M. Gigg, D. Grellscheid, K. Hamilton, et al., *Herwig++*

Physics and Manual, Eur. Phys. J. **C58** (2008) 639–707.

[23] T. Sjostrand, S. Mrenna, and P. Z. Skands, *A Brief Introduction to PYTHIA 8.1*, Comput. Phys. Commun. **178** (2008) 852–867.

[24] T. Gleisberg, S. Hoeche, F. Krauss, M. Schonherr, S. Schumann, et al., *Event generation with SHERPA 1.1*, JHEP **0902** (2009) 007.

[25] S. Alioli, P. Nason, C. Oleari, and E. Re, *A general framework for implementing NLO calculations in shower Monte Carlo programs: the POWHEG BOX*, JHEP **1006** (2010) 043, `arXiv:1002.2581 [hep-ph]`.

[26] S. Frixione and B. R. Webber, *Matching NLO QCD computations and parton shower simulations*, Journal of High Energy Physics **2002** (2002) no. 06, 029.

[27] O. S. Bruning, P. Collier, P. Lebrun, S. Myers, R. Ostojic, J. Poole, and P. Proudlock, *LHC Design Report.* CERN, Geneva, 2004.

[28] J. Pequenao, *Computer generated image of the whole ATLAS detector*, March, 2008.

[29] ATLAS Collaboration, G. Aad et al., *The ATLAS Experiment at the CERN Large Hadron Collider*, J. Instrum. **3** (2008) S08003.

[30] ATLAS Collaboration, G. Aad et al., *The ATLAS Simulation Infrastructure*, Eur. Phys. J. **C70** (2010) 823–874, `arXiv:1005.4568 [physics.ins-det]`.

[31] GEANT4 Collaboration, S. Agostinelli et al., *GEANT4: A simulation toolkit*, Nucl. Instrum. Meth. **A506** (2003) 250–303.

[32] ATLAS Collaboration, G. Aad et al., *Fast Simulation for ATLAS: Atlfast-II and ISF*, J.Phys.Conf.Ser. **396** (2012) 022031.

[33] ATLAS Collaboration, G. Aad et al., *The simulation principle and performance of the ATLAS fast calorimeter simulation FastCaloSim*, ATL-PHYS-PUB-2010-013 .

[34] W. Lampl, S. Laplace, D. Lelas, P. Loch, H. Ma, S. Menke, S. Rajagopalan, D. Rousseau, S. Snyder, and G. Unal, *Calorimeter Clustering Algorithms: Description and Performance*, Tech. Rep. ATL-LARG-PUB-2008-002. ATL-COM-LARG-2008-003, CERN, Geneva, Apr, 2008.

[35] M. Cacciari, G. Salam, and G. Soyez, *The anti-k_t jet clustering algorithm*, JHEP **0804** (2008) 063, `arXiv:0802.1189 [hep-ph]`.

[36] ATLAS Collaboration, G. Aad et al., *Pile-up subtraction and suppression for jets in ATLAS*, Tech. Rep. ATLAS-CONF-2013-083, CERN, Geneva, Aug, 2013.

[37] ATLAS Collaboration, G. Aad et al., *Tagging and suppression of pileup jets*, Tech. Rep. ATL-PHYS-PUB-2014-001, CERN, Geneva, Jan, 2014.

[38] ATLAS Collaboration, G. Aad et al., *Jet energy scale and its systematic uncertainty for jets produced in proton-proton collisions at $\sqrt{s} = 7$ TeV and measured with the ATLAS detector*, Tech. Rep. ATLAS-CONF-2010-056, CERN, Geneva, 2010.

[39] ATLAS Collaboration, G. Aad et al., *Probing the measurement of jet energies with the ATLAS detector using Z+jet events from proton-proton collisions at $\sqrt{s} = 7$ TeV*, Tech. Rep. ATLAS-CONF-2012-053, CERN, Geneva, May, 2012.

[40] ATLAS Collaboration, G. Aad et al., *Probing the measurement of jet energies with the ATLAS detector using photon+jet events in proton-proton collisions at $\sqrt{s} = 7$ TeV*, Tech. Rep. ATLAS-CONF-2012-063, CERN, Geneva, Jul, 2012.

[41] ATLAS Collaboration, G. Aad et al., *Jet energy resolution and selection efficiency relative to track jets from in-situ techniques with the ATLAS Detector Using Proton-Proton Collisions at a Center of Mass Energy $\sqrt{s} = 7$ TeV*, Tech. Rep. ATLAS-CONF-2010-054, CERN, Geneva, 2010.

[42] W. Waltenberger, R. Frühwirth, and P. Vanlaer, *Adaptive vertex fitting*, Journal of Physics G: Nuclear and Particle Physics **34** (2007) no. 12, N343.

[43] ATLAS Collaboration, *Performance of primary vertex reconstruction in proton-proton collisions at $\sqrt{s}$ =7 TeV in the ATLAS experiment*, Tech. Rep. ATLAS-CONF-2010-069, CERN, Geneva, Jul, 2010.

[44] ATLAS Collaboration, G. Aad et al., *Commissioning of the ATLAS high-performance b-tagging algorithms in the 7 TeV collision data*, Tech. Rep. ATLAS-CONF-2011-102, CERN, Geneva, Jul, 2011.

[45] G. Piacquadio and C. Weiser, *A new inclusive secondary vertex algorithm for*

b-jet tagging in ATLAS, Journal of Physics: Conference Series **119** (2008) no. 3, 032032.

[46] ATLAS Collaboration, G. Aad et al., *Calibration of b-tagging using dileptonic top pair events in a combinatorial likelihood approach with the ATLAS experiment*, Tech. Rep. ATLAS-CONF-2014-004, CERN, Geneva, Feb, 2014.

[47] ATLAS Collaboration, G. Aad et al., *Updated Luminosity Determination in pp Collisions at $\sqrt{s} = 7$ TeV using the ATLAS Detector*, Tech. Rep. ATLAS-CONF-2011-011, CERN, Geneva, 2011.

[48] S. van der Meer, *Calibration of the effective beam height in the ISR*, Tech. Rep. CERN-ISR-PO-68-31. ISR-PO-68-31, CERN, Geneva, 1968.

[49] J. M. Campbell and R. Ellis, *MCFM for the Tevatron and the LHC*, Nuclear Physics B - Proceedings Supplements **205-206** (2010) no. 0, 10 – 15.

[50] G. Corcella et al., *HERWIG 6.5: an event generator for Hadron Emission Reactions With Interfering Gluons (including supersymmetric processes)*, JHEP **01** (2001) 010, `arXiv:0011363 [hep-ph]`.

[51] J. Butterworth, J. R. Forshaw, and M. Seymour, *Multiparton interactions in photoproduction at HERA*, Z. Phys. **C72** (1996) 637–646.

[52] M. Cacciari et al., *Top-pair production at hadron colliders with next-to-next-to-leading logarithmic soft-gluon resummation*, Phys. Lett. **B710** (2012) 612–622.

[53] P. Bärnreuther, M. Czakon, and A. Mitov, *Percent Level Precision Physics at the Tevatron: First Genuine NNLO QCD Corrections to $q\bar{q} \to t\bar{t} + X$*, Phys. Rev. Lett. **109** (2012) 132001.

[54] M. Czakon and A. Mitov, *NNLO corrections to top-pair production at hadron colliders: the all-fermionic scattering channels*, JHEP **1212** (2012) 054.

[55] M. Czakon and A. Mitov, *NNLO corrections to top pair production at hadron colliders: the quark-gluon reaction*, JHEP **1301** (2013) 080.

[56] M. Czakon, P. Fiedler, and A. Mitov, *The total top quark pair production cross-section at hadron colliders through $O(\alpha_S^4)$*, Phys. Rev. Lett. **110** (2013) 252004.

[57] M. Czakon and A. Mitov, *Top++: A Program for the Calculation of the Top-Pair Cross-Section at Hadron Colliders*, `arXiv:1112.5675 [hep-ph]`.

[58] ATLAS Collaboration, G. Aad et al., *Selection of jets produced in proton-proton collisions with the ATLAS detector using 2011 data*, Tech. Rep. ATLAS-CONF-2012-020, CERN, Geneva, March, 2012.

[59] S. Bernstein, *Démonstration du théoreme de Weierstrass fondée sur le calcul des probabilités*, Comm. Soc. Math. Kharkov **13** (1912) .

[60] R. Barlow, *Extended maximum likelihood*, Nuclear Instruments and Methods in Physics Research Section A: Accelerators, Spectrometers, Detectors and Associated Equipment **297** (1990) no. 3, 496 – 506.

[61] ATLAS Collaboration, G. Aad et al., *b-jet tagging calibration on c-jets containing D^{*+} mesons*, Tech. Rep. ATLAS-CONF-2012-039, CERN, Geneva, Mar, 2012.

[62] S. Alioli et al., *Jet pair production in POWHEG*, JHEP **1104** (2011) 081.

[63] R. Frederix et al., *Scalar and pseudoscalar Higgs production in association with a top-antitop pair*, Phys. Lett. **B701** (2011) 427–433.

[64] J. Alwall, M. Herquet, F. Maltoni, O. Mattelaer, and T. Stelzer, *MadGraph 5 : Going Beyond*, JHEP **1106** (2011) 128.

[65] H.-L. Lai, M. Guzzi, J. Huston, Z. Li, P. M. Nadolsky, et al., *New parton distributions for collider physics*, Phys.Rev. **D82** (2010) 074024.

[66] A. D. Martin, W. J. Stirling, R. S. Thorne, and G. Watt, *Parton distributions for the LHC*, Eur. Phys. J. **C63** (2009) 189–285, `arXiv:0901.0002 [hep-ph]`.

[67] S. Forte, L. Garrido, J. I. Latorre, and A. Piccione, *Neural network parametrization of deep-inelastic structure functions*, Journal of High Energy Physics **2002** (2002) no. 05, 062.

[68] LHC Higgs Cross Section Working Group, S. Heinemeyer, C. Mariotti, G. Passarino, and R. Tanaka (Eds.), *Handbook of LHC Higgs Cross Sections: 3. Higgs Properties*, CERN-2013-004 (CERN, Geneva, 2013) , `arXiv:1307.1347 [hep-ph]`.

[69] ATLAS Collaboration, G. Aad et al., *Measurements of Higgs boson production and couplings in diboson final states with the ATLAS detector at the LHC*, Physics Letters B **726** (2013) no. 1-3, 88 – 119.

[70] ATLAS Collaboration, G. Aad et al., *Evidence for the spin-0 nature of the Higgs boson using ATLAS data*, Physics Letters B **726** (2013) no. 1-3, 120 – 144.

[71] CMS Collaboration, S. Chatrchyan et al., *Evidence for the direct decay of the 125 GeV Higgs boson to fermions*, `arXiv:1401.6527 [hep-ex]`.

[72] ATLAS Collaboration, G. Aad et al., *Evidence for Higgs Boson Decays to the* $\tau^+\tau^-$ *Final State with the ATLAS Detector*, Tech. Rep. ATLAS-CONF-2013-108, CERN, Geneva, Nov, 2013.

[73] B. Coleppa, F. Kling, and S. Su, *Constraining Type II 2HDM in Light of LHC Higgs Searches*, `arXiv:1305.0002 [hep-ph]`.

[74] K. Agashe, H. Davoudiasl, G. Perez, and A. Soni, *Warped gravitons at the CERN LHC and beyond*, Phys. Rev. D **76** (Aug, 2007) 036006.

[75] D. Stump, J. Huston, J. Pumplin, W.-K. Tung, H. Lai, et al., *Inclusive jet production, parton distributions, and the search for new physics*, JHEP **0310** (2003) 046.

[76] N. Greiner, A. Guffanti, T. Reiter, and J. Reuter, *Next-to-Leading Order QCD Corrections to the Production of Two Bottom-Antibottom Pairs at the LHC*, Phys. Rev. Lett. **107** (2011) 102002.

[77] ATLAS Collaboration, G. Aad et al., *Measurement of the top quark pair production cross section in the single-lepton channel with ATLAS in proton-proton collisions at 8 TeV using kinematic fits with b-tagging*, Tech. Rep. ATLAS-CONF-2012-149, CERN, Geneva, Nov, 2012.

[78] CMS Collaboration, S. Chatrchyan et al., *Measurement of differential top-quark pair production cross sections in the lepton+jets channel in pp collisions at 8 TeV*, Tech. Rep. CMS-PAS-TOP-12-027, CERN, Geneva, 2013.

[79] CMS Collaboration, S. Chatrchyan et al., *Identification of b-quark jets with the CMS experiment*, JINST **8** (2013) P04013.

[80] ATLAS Collaboration, G. Aad et al., *Measuring the b-tag efficiency in a top-pair sample with* $4.7fb^{-1}$ *of data from the ATLAS detector*, Tech. Rep. ATLAS-CONF-2012-097, CERN, Geneva, Jul, 2012.

[81] ATLAS Collaboration, G. Aad et al., *Search for resonant ZZ production in the* $ZZ \to llqq$ *channel with the ATLAS detector using 7.2 fb-1 of* $\sqrt{s} = 8$ *TeV pp collision data*, Tech. Rep. ATLAS-CONF-2012-150, CERN, Geneva, Nov, 2012.

[82] ATLAS Collaboration, G. Aad et al., *Measurement of the top quark pair differential cross-sections in the l+jets channel in pp collisions at* $\sqrt{s} = 7\,TeV$ *using the ATLAS detector*, Tech. Rep. ATLAS-CONF-2013-099, CERN, Geneva, Sep, 2013.

[83] J. Neyman and E. S. Pearson, *On the Problem of the Most Efficient Tests of Statistical Hypotheses*, Philosophical Transactions of the Royal Society of London. Series A, Containing Papers of a Mathematical or Physical Character **231** (1933) no. 694-706, 289–337.

[84] A. L. Read, *Presentation of search results: The CL(s) technique*, J.Phys. **G28** (2002) 2693–2704.

[85] E. Gross and O. Vitells, *Trial factors for the look elsewhere effect in high energy physics*, The European Physical Journal C **70** (2010) no. 1-2, 525–530.

[86] G. Cowan, K. Cranmer, E. Gross, and O. Vitells, *Asymptotic formulae for likelihood-based tests of new physics*, Eur.Phys.J. **C71** (2011) 1554, `arXiv:1007.1727 [physics.data-an]`.

[87] K. N. et al. (Particle Data Group), *The Review of Particle Physics*, J.Phys. G **37** ((2010) and 2011 partial update for the 2012 edition) 075021.